

# The astronomical consequences of primordial black holes

*Loke Lönnblad Ohlin*

---

Lund Observatory  
Lund University



2019-EXA150

Degree project of 60 higher education credits (for a degree of Master)  
May 2019

Supervisor: Melvyn B. Davies

Lund Observatory  
Box 43  
SE-221 00 Lund  
Sweden

## Abstract

In the radiation or early matter dominated eras of the Universe, there is a theoretical possibility for the formation of black holes (BHs). These primordial black holes (PBHs) have been thought of as a possible candidate for dark matter (DM), and an attractive one at that as it would explain DM using only baryonic physics. Constraints from theory and observations such as microlensing has nearly excluded the existence of large amounts of PBHs in most ranges of BH masses. However, there are still three mass ranges that remain relatively unconstrained and could therefore make up a large fraction of DM. These include asteroid mass ( $\sim 10^{13} - 10^{14}$  kg), sub-lunar ( $\sim 10^{17} - 10^{19}$  kg) and stellar mass ( $10^{31} - 10^{32}$  kg) PBHs. This project focuses on what impact a large population of PBHs in the lower mass ranges would have on stellar populations, and if any further constraints on PBH masses can be inferred from this.

Focusing on three environments; the galactic centre, solar neighbourhood and dwarf galaxies, we consider the collision, capture and settling of small PBHs inside of stars such as main sequence star, White Dwarfs (WDs) and Neutron Stars (NSs). As the PBHs that we consider are so low mass, if they make up a significant fraction of the DM their number density would be high, and therefore collisions between them and stars would be frequent. The PBHs are small, so during the collision the PBHs simply fly through the star. However due to energy dissipation into the medium of the stars, the PBH can become bound, and over multiple subsequent orbits lose more energy until they have become completely trapped inside of the star. Once this happens, the star is consumed by the PBH. This process of disrupting stars cannot be too efficient (as otherwise stars could not exist), which previous research has used to put constraints on the abundance of low mass PBHs based on the survival of star.

We model this energy dissipation, integrating the trajectories of the PBHs through a target star. We find that the energy dissipation is small, and therefore PBHs end up on too wide orbits. Due to the wide orbits, and long orbital periods, the PBHs are therefore susceptible to being scattered by intruding stars. As the energy dissipation is weaker for lower mass PBHs, and therefore their subsequent orbits become larger, this puts a lower limit on the mass range for PBHs where they can settle inside of stars with this process. This is important, as in the denser environments, where collisions and capture is the most frequent, the probability for an intruding star to eject the PBH is higher. As such, the mass range PBHs can have in order to settle is often already constrained by microlensing constraints. Previous research on the capture of PBHs in stars have not taken this into account, and therefore their results may be significantly changed.

In addition to attempting to capture onto single targets, we also consider capturing in binary stars and planetary systems. As the orbits of the target bodies have comparable velocities as that expected of the incoming PBHs, the three body interaction can exchange energy and angular momentum between the PBH and the binary. Performing n-body simulations, treating the PBHs as test particles, we find that this exchange more often than not lead to the PBHs gaining energy, and are subsequently ejected from the binary. Furthermore as the energy change due to the three body interaction is higher than

that of the energy dissipation into the medium of the star, this is the dominant process. Therefore we suggests that the settling of PBHs into stars in binary systems is improbable, invalidating previous research which has determined merger rates of systems containing a star consumed by a PBH, without considering the three body interaction.

Finally we estimate the rate at which the consumption of a white dwarf or neutron star would be observed. Using a model for a milky way equivalent galaxy and a NS population synthesis for the galactic distribution of NSs, we determine the cosmological consumption rates of WDs and NSs. Assuming that the consumption of a NS or WD is either similar to Type 1a supernovae or gamma ray bursts, we determine the observable rate of such an event. We find that, due to the aforementioned scattering by intruding stars during the settling of a PBH inside of the target, the observational rate is only significant for mass ranges already constrained by microlensing, and we are unable to derive further constraints on the abundance of PBHs.

### Acknowledgements

*I would like to thank my supervisor Melvyn B. Davies for the guidance and support throughout this work. I would also like to thank David Hobbs and Abbas Askar for the feedback on this thesis, and Rebecca Forsberg for correcting the Swedish popular science abstract. Finally I would like to thank Ross Church for fruitful discussion surrounding the topic of this thesis.*



## Populärvetenskaplig beskrivning

Inom modern astronomi är mörk materia en av dem viktigaste byggstenarna i universum. Även om vi inte kan se mörk materia, tror vi att uppemot 85 % av all materia består av det. Faktum är att vi behöver denna mängd för att förstå hur stjärnor rör sig runt Galaxen, och hur galaxer formas. Trots dess betydelse för vår nuvarande förståelse inom astronomi har vi inte kunnat identifiera vad mörk materia skulle kunna bestå av. De mest populära teorierna tror att det skulle kunna vara små partiklar, men dessa har ännu inte hittats, ens i våra mest avancerade detektorer.

En annan teori för vad mörk materia skulle kunna vara är vad som kallas uråldriga svarta hål (primordial black holes på engelska). På tidigt sjuttiotal kom Steven Hawking på att i dem första sekunderna av universum skulle svarta hål kunna bildas. Vi vet inte om detta faktiskt har skett, men om vi skulle kunna hitta ett sådant svart hål skulle det ge oss insikt i det tidiga universum. Dessutom, om tillräckligt många av dessa svarta hål bildades skulle de förklara all mörk materia i universum.

Dessa uråldriga svarta hål skulle vara unika från de vi redan vet existerar, eftersom de nästan skulle kunna ha vilken massa som helst, från några hundratusendelar gram, till miljoner gånger solens massa. Detta skiljer uråldriga svarta hål från de svarta hålen vi vet existerar, och därmed skulle vi kunna urskilja dem i observationer. Även om vi inte kan utesluta dem helt, med noggranna observationer och undersökningar har vi kunnat säga att svarta hål med specifika massor inte finns i tillräckligt stora mängder för att förklara mörk materia. Men, det är fortfarande så att all mörk materia skulle kunna bestå av små svarta hål, där våra observationer inte kan se dem. Dessa svarta hål skulle antingen kunna ha massor liknande asteroider, eller c.a. tusen till hundra tusen gånger mindre än månen. Eftersom svarta hål är kompakta skulle de minsta av dessa inte vara mycket större än en atom, medan de största skulle vara lika stora som våglängden för synligt ljus.

I detta projektet har jag undersökt vad som skulle ske ifall all mörk materia bestod av dessa små uråldriga svarta hål. Specifikt har jag teoretiskt försökt se vad som händer om de skulle kollidera med stjärnor. Eftersom det skulle finnas extremt många av dessa svarta hål, så hade dessa kollisioner vara vanliga. På grund av att svarta hålen är väldigt små, åker de för det mesta bara igenom stjärnan, men genom diverse fysikaliska processer skulle svarta hålen saktats ner av stjärnans täta innehål. Om svarta hålen saktas ner tillräckligt kan de bli gravitationellt bundna till stjärnan, och om de åker igenom stjärnan flertalet gånger fastna inuti stjärnan. Om detta sker skulle stjärnan tillslut sväljas upp av svarta hålet.

Jag har använt mig av tidigare studier och förbättrat deras teoretiska modeller, samt skapat datorsimuleringar för att se hur ofta ett uråldrigt svart hål fastnar inuti stjärnor och liknande objekt, så som vita dvärgar och neutronstjärnor. Jag har visat att denna processen är mycket mindre effektiv än tidigare trott, bland annat genom att ta hänsyn till att ett svart hål som blir bunden till en stjärna först hamnar långt bort från stjärnan innan de åker igenom igen. Därmed finns det en stor sannolikhet att en annan stjärna kommer tillräckligt nära för att via gravitationell kraft dra bort svarta hålet. Jag har även visat att det är näst intill omöjligt att svarta hålen fastnar i en stjärna som är en medlem i

ett binärt stjärnsystem, eftersom gravitationskraften från de två stjärnorna är för våldsam, och det lilla svarta hålet kastas ut.

Jag har använt mig av mina resultat för beräkna hur ofta vi skulle kunna se stjärnor bli uppätna av uråldriga svart hål. Fastän detta sällan sker, händer det tillräckligt ofta för neutronstjärnor och vita dvärgar för att vi skulle kunna se det om vi observerar flertalet galaxer. Dock gäller detta endast för svarta hål med massor som vi redan kan utesluta genom tidigare observationer.



# Contents

<b>1</b>	<b>Introduction</b>	<b>6</b>
<b>2</b>	<b>Primordial black holes constraints</b>	<b>9</b>
2.1	PBH mass function . . . . .	9
2.2	Current constraints on PBH masses . . . . .	10
2.2.1	Hawking Radiation . . . . .	11
2.2.2	Gravitational lensing . . . . .	11
2.2.3	Constraints from accretion . . . . .	13
2.2.4	Large scale structure constraints . . . . .	13
2.2.5	Dynamical constraints . . . . .	13
2.2.6	Disruption of Stellar Remnants . . . . .	14
2.3	Remaining mass windows . . . . .	15
<b>3</b>	<b>Collisions with PBHs</b>	<b>16</b>
3.1	The collision rate . . . . .	16
3.2	Environments . . . . .	18
3.2.1	Solar Neighbourhood . . . . .	19
3.2.2	Galactic centre . . . . .	20
3.2.3	Dwarf galaxies . . . . .	22
3.3	Targets of PBH . . . . .	25
3.3.1	Stars and stellar remnants . . . . .	26
3.3.2	Planetary Systems . . . . .	28
3.4	Collision rates . . . . .	28
<b>4</b>	<b>Capturing processes</b>	<b>31</b>
4.1	Energy dissipation . . . . .	31
4.1.1	Dynamical friction . . . . .	32
4.2	Numerical simulations: Single targets . . . . .	38
4.3	Capture rate . . . . .	42
4.4	Settling phase . . . . .	42
4.5	Capturing in binaries . . . . .	46
4.6	Neutron star binaries . . . . .	46
4.6.1	Co-planar trajectories . . . . .	48

*CONTENTS*

---

4.6.2	Random trajectories . . . . .	51
4.7	Capture in planetary systems . . . . .	54
<b>5</b>	<b>The growth of PBH inside of stars &amp; transient rates</b>	<b>56</b>
5.1	Growth of a settled black hole . . . . .	56
5.1.1	Angular momentum . . . . .	57
5.1.2	Radiation pressure . . . . .	59
5.1.3	Possibility of collapse . . . . .	62
5.1.4	Consumption time and possible transients . . . . .	63
5.1.5	White dwarfs and Main sequence stars . . . . .	65
5.2	Consumption probability . . . . .	67
5.2.1	Neutron star survival in the Galactic centre . . . . .	68
5.3	Transient rates . . . . .	70
5.3.1	Milky way equivalent galaxy . . . . .	70
5.3.2	Dwarf galaxies . . . . .	74
5.3.3	Cosmological transit rate . . . . .	76
<b>6</b>	<b>Discussion</b>	<b>79</b>
6.1	Comparison to previous work . . . . .	80
6.1.1	Capture rates . . . . .	80
6.1.2	Disruption during settling & binaries . . . . .	81
6.2	Energy dissipation and capture processes . . . . .	81
6.2.1	Energy dissipation models . . . . .	82
6.2.2	Properties of the target . . . . .	83
6.2.3	A third capture channel: PBH binaries . . . . .	84
6.3	Viability of the observational transient rates . . . . .	85
6.3.1	Transients of PBH consumption events . . . . .	85
6.3.2	Lookback time . . . . .	87
6.3.3	Viable mass range of PBH . . . . .	87
<b>7</b>	<b>Summary &amp; conclusions</b>	<b>89</b>
7.1	Summary . . . . .	89
7.2	Conclusions . . . . .	91
<b>A</b>	<b>General relativistic calculations</b>	<b>93</b>
A.1	Schwarzchild metric . . . . .	93
A.1.1	Cross section . . . . .	94
A.1.2	Trajectories . . . . .	95
A.2	General static, spherically symmetric metric . . . . .	98
<b>B</b>	<b>Galactic neutron star distribution</b>	<b>100</b>
B.1	Population synthesis . . . . .	100
B.1.1	Galactic distribution . . . . .	100

---

B.1.2 Kick velocity and NS age . . . . .	101
B.1.3 Numerical integration . . . . .	102
B.2 Resulting distribution . . . . .	103

# List of Figures

2.1	Current constraints on the primordial black hole dark matter fraction . . . . .	10
3.1	Orbital velocity, velocity dispersion and density profiles in the galactic centre	23
3.2	The collision rate profile in the galactic centre . . . . .	23
3.3	The velocity dispersion and dark matter density for dwarf galaxies . . . . .	26
3.4	Velocity distribution of collisions . . . . .	30
4.1	Sketch of the scattering of a particle by a primordial black hole . . . . .	36
4.2	Velocity dependence of the dynamical friction model . . . . .	37
4.3	Energy loss from energy dissipation . . . . .	41
4.4	Settling time and maximum radius during the settling phase . . . . .	44
4.5	A sketch of an the encounter with a binary . . . . .	47
4.6	A sketch of the energy loss during the encounter . . . . .	47
4.7	Snapshots of a NS-NS binary scattering PBHs . . . . .	50
4.8	The distribution of $\Delta E$ per minimum passage . . . . .	51
4.9	Number of PBHs still bound after a given time in a binary . . . . .	52
4.10	Final energy and radial distribution of surviving PBHs in binary capture. .	53
5.1	Size of the accretion disc around a PBH growing inside a NS . . . . .	58
5.2	Limits from the survival of NS in the galactic centre . . . . .	69
5.3	Settling rate in a MWEG for NSs and WDs . . . . .	73
5.4	Fraction of DM required in order to see one PBH consumption event . .	78
7.1	Schematic on how many PBHs collide, captures and settles inside of a target	91
B.1	Initial positions of the NS population . . . . .	103
B.2	Circular velocity, initial distribution of NS and final distribution of NS . .	104

# List of Tables

3.1	Parameters for the density profile given by Fritz et al. (2016) . . . . .	21
3.2	Parameters and fiducial values for dwarf galaxies . . . . .	25
3.3	The masses and radii for the targets . . . . .	26
3.4	Collision rates . . . . .	29
4.1	Capture rates . . . . .	43
B.1	Parameters for the spiral arms form Wainscoat et al. (1992) . . . . .	101

# Chapter 1

## Introduction

Dark matter (DM) is vital for our current understanding of the universe. Assuming that, outside of relativistic effects, Newtonian gravity is valid on all scales DM explains the flattened rotation curves of spiral galaxies, high velocity dispersion in galaxy clusters (eg. [Zwicky 1933](#)), along with being necessary for the formation of galaxies. These observations and current cosmological models put the DM fraction of the total energy budget of the universe as  $\sim 25\%$  ([Planck Collaboration et al. 2016](#)), making up the vast majority of matter. For DM to explain these phenomena, it needs to satisfy at least two conditions: it has to be non-interacting with light, and be collisionless. With these conditions, one can imagine multiple DM candidates, with the current favourites being either particles as DM, such as sterile neutrinos or Weakly Interacting Massive Particles (WIMPS)(for review, see [Bertone et al. 2005](#)), or more massive objects, eg. MAssive Compact Halo Objects (MACHOs). However, none of these have yet to be observed, and currently we do not know what DM consists of.

One of the more interesting candidates for DM is that of Primordial Black Holes (PBHs). Quantum fluctuations in the early universe grows during inflation, and, if they are compact enough, can collapse into Black Holes (BHs) ([Hawking 1971](#)). Due to them being collisionless and (largely) non-interacting with light, if enough of these PBHs form, they would act as DM, without the need of a new, non-baryonic particle as with WIMPS (for recent review on PBHs as DM candidates, see [Carr et al. 2016](#)). A key point with PBHs, is that the time during inflation at which they form depend on the inflation model/formation mechanism (see examples [Polnarev & Khlopov 1982](#); [Leach et al. 2000](#); [Ballesteros & Taoso 2018](#), see also review [Khlopov 2010](#)). Due to the exponential growth the perturbations, the mass of PBHs depend on their formation time ([Carr & Hawking 1974](#); [Carr et al. 2010](#)). The large range in possible formation epochs therefore imply that PBHs have little in theoretical limits to their mass, which can range from  $10^{-5}$  g to possibly more than  $10^5$   $M_\odot$ .

As the mass of PBHs is dependent on the formation model, the discovery or exclusion of a PBH of a given mass would have implications on the physics in the early universe. Furthermore, the existence of PBHs would have several other implications on the universe as we observe it today (discussed more in detail in chapter [2](#)). However, little evidence for PBH has been found, and current observations restrict the population of PBHs. As we will

go into detail in the next chapter, there are currently only three mass ranges where PBHs could make up a significant amount of the DM content. These being PBHs with masses of  $10^{16}$  g –  $10^{17}$  g, called asteroid mass black holes,  $10^{20}$  g –  $10^{22}$  g sub-lunar mass black holes, and stellar mass black holes in the range  $10 - 100 M_{\odot}$ . In order to constrain these mass ranges further, and possibly exclude the existence of PBHs, one needs to consider the astronomical consequences that would come from a large population of BHs in these mass ranges.

If all of the DM was made up of PBHs, then one can consider the collision between them and the stellar population. As we will show, for the asteroid mass and sub-lunar mass PBHs, due to their low mass and corresponding high number density, these collisions would be frequent. For these low mass PBHs, a collision does not necessarily lead to an interesting effect (but see, [Graham et al. 2015](#); [Abramowicz et al. 2018](#)), however, there is still a possibility that the PBHs can be captured and become gravitationally bound to the star. In that case, the decay of subsequent orbits can lead to the PBH settling inside of the star, at which point the PBH starts to grow via mass accretion, ultimately consuming the star. The key phases of this process would then be the collision, capture and settling of the PBH.

The rate at which PBHs captures inside of Neutron Stars (NSs) has been considered in [Capela et al. \(2013\)](#). By calculating the energy dissipation PBHs experience as they travel through NSs, it was estimated that the capture rate of PBHs inside of NSs could be high inside of globular clusters. Based on the survival of NSs inside of globular clusters, [Capela et al. \(2013\)](#) estimated constraints on the total DM fraction that can consist of sub-lunar mass PBHs. This process of capturing PBHs inside of NS, has also been used to estimate the abundance of r-process elements formed in the consumption of NSs ([Fuller et al. 2017](#)), giving values similar to what is observed, even if only a small amount of the DM consisted of PBHs. Similarly, the possible merger rate between stellar remnants and the  $\sim M_{\odot}$  BH formed in the consumption of NSs and White Dwarfs (WDs) has been estimated ([Bramante et al. 2018](#); [Fuller et al. 2017](#)).

However, the constraint from the survival of neutron stars derived by [Capela et al. \(2013\)](#) relies on high DM densities in globular clusters. As the DM density in globular clusters is uncertain, these constraints can be significantly alleviated. The lack of this constraint leaves the sub-lunar mass window unconstrained, and can therefore supply all of the DM. Furthermore, several of these aforementioned works concerns the capture of PBHs inside of binary NSs ([Bramante et al. 2018](#); [Takhistov 2018](#)), but none of them considers the three body interaction between the PBHs and the binary, instead treating the binary as a single target with twice the potential of a NS ([Takhistov 2018](#)). As the orbital velocity of NS binaries can be similar to that of the incoming PBHs, the gravitational interaction between the binary and the PBHs might be significant. Finally, most of these studies take a simple approach to the settling phase, and are only concerned with the timescale of the PBH to settle once it has been captured ([Capela et al. 2013](#); [Fuller et al. 2017](#); [Takhistov 2018](#)).

In order to attempt to derive new constraints for the sub-lunar mass region, in this thesis, we consider the same idea of capturing inside of neutron stars as ([Capela et al.](#)

2013), not only exploring multiple environments where this could be a likely occurrence, but also other targets such as white dwarfs and main sequence stars. We also adopt a more realistic treatment of both the settling phase of the PBHs and the capture in binaries. As the consumption of stars/stellar remnants of a PBH could be luminous events, we also estimate the rate at which these transient events would be observed, which as far as we know, has yet to be considered.

### Structure of thesis

- In chapter 2, we summarise all the current constraints on the total DM mass fraction of PBHs.
- In chapter 3, we discuss the collisions between PBHs and a given target. In section 3.1 we derive the collision rate between a target and PBHs, motivated by which, we choose and model the environments and targets in consideration in sections 3.2 and 3.3. In 3.4 we show that the collision rates indeed are high between low mass PBHs and most targets.
- In chapter 4, we consider different channels by which a PBH can be captured and settle inside of a given target. First, in section 4.1 we consider the capture of PBHs in single targets based on the energy dissipation model of Capela et al. (2013), integrating it over the trajectory through the star. In section 4.4 we consider the settling phase of PBHs, using simple analytical arguments to estimate the time it takes for a PBH to settle inside of a star, and how long the orbits are during the settling. We find that there is a non-negligible probability that a captured PBH is scattered away by intruding stars during settling. We then turn towards capturing in binary systems in sections 4.5 and 4.6, where we use an N-body code to integrate trajectories through the binary. We determine that the capture of PBHs in binaries is either too rare for our simulations to detect, or impossible.
- In chapter 5, we start by discussing how a PBH grows inside of a star in section 5.1. We then derive settling rates inside of a Milky way-like galaxy and dwarf galaxies in section 5.3, estimating the rate at which transient events from the consumption of stars can be observed.
- In chapter 6, we discuss how our results differ from previous research, pointing out how these results weakens, or even invalidates much of these works. We then move on to discuss possible flaws in or models for the capture of PBHs, and the validity of the derived observational rates.
- In chapter 7, we briefly summarise the entire thesis, and list the main results.

# Chapter 2

## Primordial black holes constraints

In this chapter we show and explain the current constraints on the DM fraction that can be occupied by PBHs. We start by discussing the mass functions of the PBHs, and why this is assumed to be a delta function when deriving constraints. Then we discuss the different constraints that can be derived on PBHs, based both on observations such as microlensing, but also theoretical ones, such as those based on Hawking radiation, the ones based on the interaction between PBHs and baryonic matter. The strongest of these constraints are shown in fig. 2.1. At the end of this chapter, we summarise the three mass windows that are currently lacking strong constraints.

### 2.1 PBH mass function

Before we start describing the current constraints on the fraction of DM that can currently be occupied by PBHs, we make a quick note on the assumed mass function of the PBHs. As mentioned before, due to the dependence on the formation mechanism of PBHs, the mass of PBHs can be within a large range of theoretically allowed masses. The astrophysical impact of a large population of low mass BHs can be very different from that of massive BHs (think  $10^{15}$  g BHs compared to  $10^5 M_\odot$  BHs). Astrophysical constraints therefore tend to limit the abundance of PBHs of a specific mass range. The distribution of PBH masses is then important when considering constraints (for instance, see Carr et al. 2016; García-Bellido et al. 2018).

Typically, astrophysical constraints are derived assuming that all PBHs are of the same/similar mass (usually referred to as a monochromatic mass distribution). Due to the mass dependence of the constraints, and the dependence on the mass distribution on the formation mechanism, it is simpler to consider constraints on a monochromatic mass function. Most formation models suggest extended mass distributions, and the shape of these functions can significantly change the effectiveness/strength of the constraints (see discussion in Carr et al. 2016). However, for simplicity, and coherence with previous work, we shall also consider a monochromatic mass function.

## 2.2 Current constraints on PBH masses

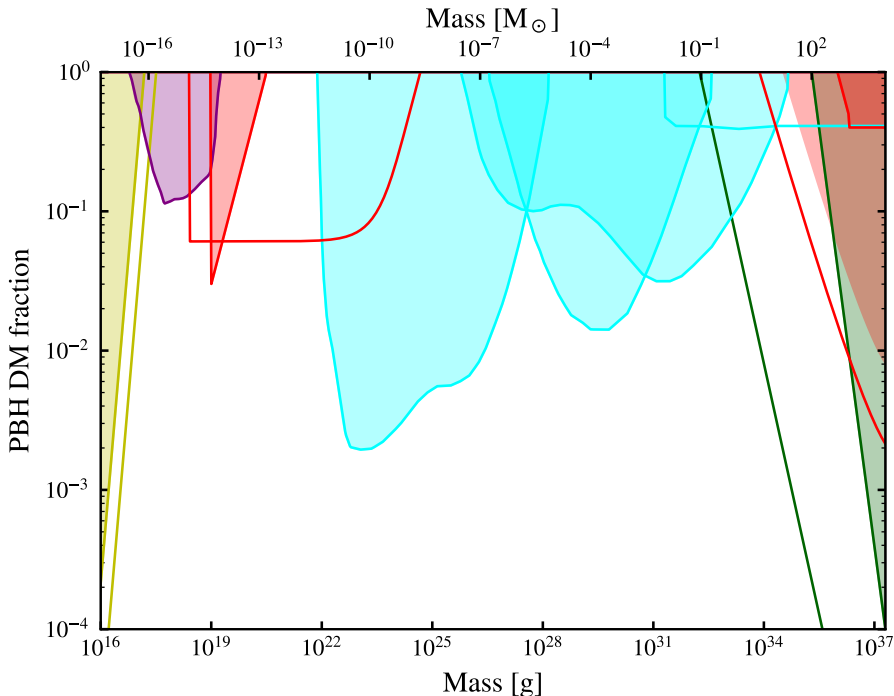


Figure 2.1: A representation of the current constraints on PBH masses. Constraints are separated into categories by colour. **Yellow**) Hawking radiation ([Carr et al. 2010; Clark et al. 2018](#)) between  $10^{16} - 10^{17}$  g; **Purple**) femtolensing ([Barnacka et al. 2012](#)) between  $10^{16} - 10^{19}$  g; **Cyan**) microlensing ([Tisserand, P. et al. 2007; Niikura et al. 2019b,a](#)) from  $10^{22}$  g; **Green**) accretion [Ali-Haïmoud & Kamionkowski \(2017\); Hektor et al. \(2018\)](#) from  $0.1 M_{\odot}$ ; **Red**) dynamical constraints [Quinn et al. \(2009\); Capela et al. \(2013\); Graham et al. \(2015\); Brandt \(2016\)](#) between  $10^{19}$  g –  $10^{25}$  g and above  $1 M_{\odot}$ . For details see text. Constraints that are not filled have been challenged. Masses below or above the range shown are have either already evaporated, or are subject to dynamical constraints ([Carr & Sakellariadou 1999](#)).

One can derive constraints on the total DM mass fraction of primordial black holes based on the fact that such an abundance of primordial black holes have several consequences on their surrounding. The non-observations of such consequences then imposes constraints on the mass fraction of the total DM  $f_{\text{DM}} = \rho_{\text{PBH}}/\rho_{\text{DM}}$ . The currently strongest constraints are summarised in fig. 2.1 and explained in the rest of this section.

### 2.2.1 Hawking Radiation

It has been theorised that due to quantum mechanical effects near the event horizon, black holes radiate energy in what is called Hawking radiation ([Hawking 1975](#)). Due to this radiation black holes loses mass, and evaporate. This process applies for PBHs as well (in fact it was first considered for them), and as the lifetime of a PBH due to this radiation goes as  $m_{\text{PBH}}^3$ , low mass black holes evaporate faster. This sets a fixed limit on the number of low mass PBHs that can still be around at the current age of the universe, as all PBHs with masses less than  $m_{\text{PBH}} \leq 10^{15}$  g would already have evaporated.

Furthermore, the evaporation PBHs in would cause excess radiation which imposes constraints on these lower masses existing, or having existed in the past. The radiation caused by masses beyond  $m_{\text{PBH}} = 10^{15}$  g would imply an excess intensity in extragalactic background radiation, which can be constrained from observations. This then implies that the mass fraction of PBHs is limited to ([Carr et al. 2010](#))

$$f(m_{\text{PBH}}) \leq 2 \times 10^{-8} \left( \frac{m_{\text{PBH}}}{m_{\text{eva}}} \right)^{3+\epsilon}, \quad (2.1)$$

where  $m_{\text{eva}} = 5 \times 10^{14}$  g and  $\epsilon$  is power associated with the observed extra-galactic x-ray and  $\gamma$ -ray spectra, and is likely within the range of 0.1 – 0.4 ([Sreekumar et al. 1998](#); [Strong et al. 2004](#)). This constraint is shown in yellow on the low mass end of fig. 2.1 for  $\epsilon = 0.2$ , and can be seen to constrain PBH masses up to  $10^{17}$  g.

Recently, the observation of a stronger than expected 21 cm absorption line by the EDGES collaboration ([Bowman et al. 2018](#)) suggested lower temperatures in the early universe. If confirmed, the cooler temperatures would imply stronger constraints based on Hawking radiation, as the radiation would result in extra heating ([Clark et al. 2018](#)). The improvement of the constraints can roughly be approximated with the maximum  $f_{\text{DM}}$  being 10-100 times lower than that of [Carr et al. \(2010\)](#), which would increase the mass range constrained.

### 2.2.2 Gravitational lensing

As gravity bends light, massive or compact objects can act as lenses. Therefore, if a massive object comes in between the line of sight of an observer and a background luminous object, the light is can be bent, producing two lensed images of the background object. This effect is called gravitational lensing, and is frequently exploited in observational astrophysics (for review, see [Bartelmann 2010](#)). In the context of constraining PBHs, constraints on PBH masses of  $10^{22}$  g –  $100 M_{\odot}$  and  $10^{16}$  –  $10^{19}$  g can be derived based on two types of lensing observations, microlensing and femtolensing respectively. Next we discuss these two lensing techniques, along with lensing of type 1a supernovae.

#### Microlensing

Small, compact dark objects, which can be approximated as point masses, do give rise to lensing events. While they are too small in order for the lensed images to be resolved, the

super-position of the two images causes an small increase in luminosity for the period of time that they lie between the observer and the background object. This effect is what is usually called microlensing (for review, see [Roulet & Mollerach 1997](#)). If PBHs made up a significant fraction of the DM of the Galactic halo, one would expect to observe microlensing events from PBHs, or Massive Compact Halo Objects (MACHOs) in general ([Paczynski 1986](#)).

Multiple studies have attempted to observe microlensing events from MACHOs, and with only a few possible detected events, have managed to significantly constrain a large range of PBH masses. Combining the results from the MACHO ([Alcock et al. 1998](#)) and the EROS surveys ([Tisserand, P. et al. 2007](#)), one can effectively constrain PBH masses between  $10^{-9} - 10^2 \text{ M}_\odot$ . Furthermore, the OGLE study put strong constraints on the  $10^{-6} - 1 \text{ M}_\odot$  mass range ([Wyrzykowski et al. 2009, 2010, 2011a,b; Niikura et al. 2019b](#)). For lower black hole masses, the Kepler mission managed to constrain PBH masses between  $10^{-9} - 10^{-7} \text{ M}_\odot$  ([Griest et al. 2013, 2014](#)), but this has been surpassed by the much stronger constraints by the HSC-Subaru survey ([Niikura et al. 2017, 2019a](#)) which effectively constrain the mass range  $10^{22} \text{ g} \leq m_{\text{PBH}} \leq 10^{29} \text{ g}$ . The total mass range constrained by these surveys is

$$10^{22} \text{ g} \leq m_{\text{PBH}} \leq 30 \text{ M}_\odot, \quad (2.2)$$

and the currently strongest of these constraints are displayed in fig. [2.1](#).

### Femtolensing

The constraints from the HSC described in the previous section should be able to constrain PBH masses lower than  $10^{22} \text{ g}$ . However due their low masses, the Schwarzschild radii of these PBHs becomes smaller than the wavelength used for in the observation. This causes the light to be diffracted, and the amplitude of the luminosity spike to decrease, reducing the effectiveness of the microlensing constraint ([Inomata et al. 2018; Naderi et al. 2018; Niikura et al. 2019a](#)).

This effect can however be used to derive other constraints on the PBH mass fraction. [Gould \(1992\)](#) suggested that small  $10^{17} - 10^{20} \text{ g}$  PBHs would induce a sinusoidal pattern on the light spectrum of Gamma-Ray Bursts (GRBs). This is denoted as Femtolensing, and has been tested on GRBs, but yet to be observed, constraining PBHs in the mass range ([Barnacka et al. 2012](#))

$$10^{16} \text{ g} \leq m_{\text{PBH}} \leq 10^{19} \text{ g}. \quad (2.3)$$

### Supernovae lensing

Recently, it has been suggested that the lack of lensing events in cosmological type 1a supernovae provides constraints on PBH masses larger than  $0.01 \text{ M}_\odot$  ([Zumalacárregui & Seljak 2018](#)). However, it has been argued that the aforementioned study adopted too strong priors on their cosmological model ([García-Bellido et al. 2018](#)). This along with

more realistic sizes of type 1a supernovae (and consideration of a non-monochromatic PBH mass function) reduces the effectiveness of the constraint. As such, we display the constraint in fig. 2.1, but keep in mind that the effectiveness is disputed.

### 2.2.3 Constraints from accretion

The accretion of gas onto massive PBH after recombination would radiate high energy photons. The radiation would then heat up the universe and leave an imprint on the power spectrum and anisotropies of the cosmic microwave background. Using WMAP and FIRAS, [Ricotti et al. \(2008\)](#) investigated the existence of these imprints, and was able to put significant constraints on the abundance of PBHs in the mass range

$$1 \text{ M}_\odot \leq m_{\text{PBH}} \leq 10^6 \text{ M}_\odot. \quad (2.4)$$

These constraints may be significantly weaker though, as there are uncertainties in how efficiently the BH radiates in the early universe. Using a more detailed model for the radiative efficiency of the PBHs, [Ali-Haïmoud & Kamionkowski \(2017\)](#) found that these constraints can only efficiently constraint masses between

$$100 \text{ M}_\odot \leq m_{\text{PBH}} \leq 10^6 \text{ M}_\odot, \quad (2.5)$$

depending on whether the emitted radiation ionised the surrounding gas or not.

Using the aforementioned 21 cm observation, [Hektor et al. \(2018\)](#) derived constraints based on the heating from accretion onto massive PBHs. Their constraints are similar to that of [Ricotti et al. \(2008\)](#) and covers the mass range  $\geq 1 \text{ M}_\odot$  depending on model. We show the constraints of [Ali-Haïmoud et al. \(2017\)](#) and [Hektor et al. \(2018\)](#) in fig. 2.1, keeping in mind that they can vary greatly depending on the model used for the accretion efficiency.

### 2.2.4 Large scale structure constraints

If massive PBHs made up a large amount of the DM in the universe, due to their massive size, their number density would be subject to Poisson fluctuations. These fluctuations would impact the formation of the large scale structures, as pointed out by [Meszaros \(1975\)](#). Using observations of the Lyman- $\alpha$  forest, and correlating it to the DM power spectrum, [Afshordi et al. \(2003\)](#) managed to derive an upper limit on PBHs supplying all DM of  $\sim 10^4 \text{ M}_\odot$ . Using analytical arguments, [Carr et al. \(2010\)](#) obtained a similar result, providing constraints on PBH masses greater than

$$m_{\text{PBH}} \geq 10^4 \text{ M}_\odot. \quad (2.6)$$

### 2.2.5 Dynamical constraints

As PBHs interact gravitationally or dynamically with astrophysical objects, one is able to derive constraints based on the results of these interactions. As the strength of the

gravitational interaction scales with the mass of the PBHs, these constraints typically cover large PBH masses. We briefly summarise these below.

- **Dynamical friction on PBHs:** Massive PBHs would experience a drag force from the interaction with nearby stars. As such they loose angular momentum and migrate towards the centre of galaxies. Based on the mass of the Galactic centre of the Milky Way, [Carr & Sakellariadou \(1999\)](#) derived a constraint on massive ( $> 10^4 M_\odot$ ) PBHs. There are some uncertainties for the larger PBHs ( $> 10^6 M_\odot$ ), as the three-body interaction between three of these would effectively eject one of the PBHs via the slingshot mechanism.
- **Heating of galactic discs:** In the interactions between massive PBHs and stars, the stars would gain orbital energy. The resulting heating of galactic discs was studied in [Carr & Sakellariadou \(1999\)](#), where constraints on PBH masses larger than  $10^6 M_\odot$  was found.
- **Disruption of wide binaries and clusters:** If a massive PBH encounters a wide stellar binary, there is a probability that the binary is disrupted. The current constraints based on this method is based on the observed number of wide halo binaries, which gives constraints of  $f_{DM} < 0.3$  for masses larger than  $5 \times 10^2 M_\odot$  ([Quinn et al. 2009](#)). Similarly, one can derive constraints based on the survival of stellar clusters, which would be prone to breakup if most of the DM consisted of massive PBHs. Considering open clusters, [Carr & Sakellariadou \(1999\)](#) derived constraints for PBH masses between  $10^3 M_\odot - 10^7 M_\odot$ .
- **Heating in dwarf galaxies:** Based on the heating and disruption of dwarf galaxies and the survival of clusters in dwarf galaxies, [Brandt \(2016\)](#) derived constraints on the fraction of PBHs. The strongest of these came from the survival of a stellar cluster in the dwarf galaxy Eridanus II. This constraint covers masses larger  $5 M_\odot$ , however it is also heavily dependent on the DM density and velocity dispersion in the centre of Eridanus II.

### 2.2.6 Disruption of Stellar Remnants

The final set of constraints that we list here, are those based on the collisions/capture of small black holes in stellar remnants. This is the type of constraint that we attempt to derive, and discuss in detail in the remainder of the thesis. However, we list the more important constraint which has been derived in the literature. The first of these constraints is the aforementioned capture of PBHs inside of neutron stars in globular clusters, derived in [Capela et al. \(2013\)](#). They found the probability of neutron stars being disrupted to be significant. The survival of neutron stars in globular clusters would then imply a low number density of PBHs, which [Capela et al. \(2013\)](#) used to derive constraints in the mass range of  $10^{20} - 10^{23}$  g. However, as mentioned before, this constraint is based on there being a significant DM density in the cores of globular clusters, which is uncertain.

It has been pointed out in [Graham et al. \(2015\)](#), that the energy dissipation into the medium of white dwarfs would heat up the medium. If the increased heat is enough to cause a runaway fusion event, the white dwarf would disrupt in a type Ia SNe. Based on the survival of massive white dwarfs, [Graham et al. \(2015\)](#) derived constraints covering the mass range

$$10^{19} \text{ g} \leq m_{\text{PBH}} \leq 10^{20} \text{ g}. \quad (2.7)$$

## 2.3 Remaining mass windows

On examination of fig. 2.1, one can see that there is at least one mass range that is currently not well constrained. If one considers the uncertainties in some of the constraints, three mass windows remain where PBHs can constitute a significant ( $> 10\%$ ) fraction of the total DM content of the universe. These three windows are listed below.

- **Stellar mass:** By considering the lowest possible constraints from accretion ([Ali-Haïmoud & Kamionkowski 2017](#)), and relaxing the constraints from the heating of dwarf galaxies ([Brandt 2016](#)), a mass window between  $\sim 10 M_\odot$  and  $\sim 100 M_\odot$  appears where more than 10% of the DM can be made up by PBHs. This window can however be severely reduced when including the 21-cm accretion constraint of ([Hektor et al. 2018](#)).
- **Sub-lunar mass:** The constraint from capturing PBHs in NS in globular clusters depends on a high DM density in GC, which as mentioned is uncertain. Relaxing this constraint, one can find a regime between the constraint based on the disruption of white dwarfs ([Graham et al. 2015](#)) and microlensing constraints ([Niikura et al. 2019a](#)). This available mass window ( $10^{20} - 10^{22}$  g) is the currently most unconstrained.
- **Asteroid mass:** PBHs of masses  $10^{16} - 10^{17}$  g can not make up all DM, as long as the femtolensing constraint ([Barnacka et al. 2012](#)) is valid. However this constraint still allows for a substantial amount of DM (40 %) to consist of PBHs in this mass range. Furthermore, one can reduce the constraints from Hawking radiation by changing  $\epsilon$  the exponent of eq. (2.1). However, if one includes the 21-cm constraints of [Clark et al. \(2018\)](#), this mass range is only viable for  $m_{\text{PBH}} \sim 10^{17}$  g.

In this thesis, we concern ourselves with attempting to derive new constraints, mainly in the sub-lunar mass region, but also considering the asteroid mass black holes.

# Chapter 3

## Collisions with PBHs

In order to investigate the capture of PBHs in targets such as stars, stellar remnants and systems, we first need to determine how often PBHs collide, or interacts with these targets. In this chapter we derive the collision rate between PBHs and given targets. Then, based on the dependence this collision rate has on the velocity dispersion and density of DM, we chose environments, with models based on observations, in which we consider these collisions. Next we describe the choice and models for the various targets. Finally we calculate the collision rates between PBHs and all targets, within all environments for a given mass of the PBHs. We find that due to the low mass of the PBHs in consideration, the collision rates can be significantly high, especially for DM rich environments such as the galactic centre.

### 3.1 The collision rate

If we focus on one target and consider its rest frame, one can describe the collision rate  $\Gamma$  via

$$\Gamma = n\sigma v_{\text{rel}}, \quad (3.1)$$

where  $n$  is the number density of impactors (PBHs),  $v_{\text{rel}}$  the relative velocity between the target and the impactors, and  $\sigma$  the cross section of the collision. This equation holds given that all impactors have the same velocity, which is generally not the case. In the remainder of this section, we describe the distribution of relative velocities, and the cross section, in order to construct a general collision rate.

#### Relative velocity distribution

As the main question of this thesis is on the viability of PBHs as dark matter, our assumption is that the PBHs make up the DM halos around galaxies. Therefore PBH have the properties that we can infer on dark matter halos today. The halo is a relaxed, self gravitating system, and is therefore virialised. Furthermore, we know that in galaxies, the orbital

velocity  $v_{\text{orb}}$ , and by extension the velocity dispersion  $\sigma_v$ , is roughly constant with distance from the centre. If one assumes a spherical, isothermal (same velocity) distribution, one retrieves a Maxwellian distribution in velocities (Binney & Tremaine 2008)

$$f(v)dv_xdv_ydv_z = \left(\frac{3}{2\pi\sigma_v^2}\right)^{3/2} \exp\left(-\frac{3v^2}{2\sigma_v^2}\right) dv_xdv_ydv_z \quad (3.2)$$

where  $v^2 = v_x^2 + v_y^2 + v_z^2$ . As we describe in the next section on the environments that we consider, the assumption that the velocity profile is constant is not always accurate. As such the PBHs do not necessarily follow a Maxwellian velocity distribution. However, as an approximation we assume this distribution.

We also need to consider that the target is going to have some velocity. Generalising, we say that the target (stellar) population is described by a distribution about some mean velocity  $\langle v_{\text{tar}} \rangle$ . If we assume that the distribution is spherical, then it is also described by a Maxwellian

$$f(v)du_xdu_ydu_z = \left(\frac{3}{2\pi\sigma_u^2}\right)^{3/2} \exp\left(-\frac{3u^2}{2\sigma_u^2}\right) du_xdu_ydu_z, \quad (3.3)$$

where  $u$  is the velocity about  $\langle v_{\text{tar}} \rangle$ , with dispersion  $\sigma_u$ . It can be shown that the difference between two velocities given by separate Maxwellians with dispersions  $\sigma_v$  and  $\sigma_u$ , is also given by a Maxwellian with dispersion  $\sigma_{\text{rel}}^2 = \sigma_v^2 + \sigma_u^2$  (Binney & Tremaine 2008). Therefore the distribution of the relative velocities between a target and the PBHs can be written as

$$f(v_{\text{rel}})d^3u_{\text{rel}} = \left(\frac{3}{2\pi\sigma_{\text{rel}}^2}\right)^{3/2} \exp\left(-\frac{3u_{\text{rel}}^2}{2\sigma_{\text{rel}}^2}\right) d^3u_{\text{rel}}, \quad (3.4)$$

where  $\mathbf{v}_{\text{rel}} = \langle \mathbf{v}_{\text{tar}} \rangle + \mathbf{u}_{\text{rel}}$ , and  $u_{\text{rel}}$  is the difference of the PBH velocity and the target velocity about  $\langle v_{\text{tar}} \rangle$ .

As we have assumed spherical symmetry, we can decompose  $d^3u_{\text{rel}}$  into the components orthogonal and parallel to  $\langle \mathbf{v}_{\text{tar}} \rangle$ ,  $u_{\perp}$  and  $u_{\parallel}$ , along with some angle. Then the distribution of the relative velocities become

$$f(v_{\text{rel}})du_{\parallel}du_{\perp} = \left(\frac{3}{2\pi\sigma_{\text{rel}}^2}\right)^{3/2} 2\pi \exp\left(-\frac{3u_{\text{rel}}^2}{2\sigma_{\text{rel}}^2}\right) u_{\perp} du_{\parallel} du_{\perp}, \quad (3.5)$$

where  $v_{\text{rel}}^2 = (\langle v_{\text{tar}} \rangle + u_{\parallel})^2 + u_{\perp}^2$ , and  $u_{\text{rel}} = u_{\parallel}^2 + u_{\perp}^2$ . In the case of the target population having no mean velocity, this can be reduced further to

$$f(v_{\text{rel}})dv_{\text{rel}} = \left(\frac{3}{2\pi\sigma_{\text{rel}}^2}\right)^{3/2} 4\pi \exp\left(-\frac{3v_{\text{rel}}^2}{2\sigma_{\text{rel}}^2}\right) v_{\text{rel}}^2 dv_{\text{rel}}, \quad (3.6)$$

as  $v_{\text{rel}} = u_{\text{rel}}$ .

### Cross section

Next we describe the cross section  $\sigma$  in eq. (3.1). Naively this would be the cross section of the target,  $\pi R_{\text{tar}}$ , where  $R_{\text{tar}}$  is the radius of the target. However, as both the target and PBHs gravitates towards each other, this cross section is increased. If one considers the maximum impact parameter  $b$  that would lead to collision, one gets from conservation of energy and angular momentum that

$$b = R_{\text{tar}} \left( 1 + \frac{2G(M + m_{\text{PBH}})}{R_{\text{tar}} v^2} \right)^{1/2}, \quad (3.7)$$

where its been assumed that  $r_{\text{PBH}} \ll R_{\text{tar}}$ . The cross section is given as

$$\sigma = \pi b^2 \quad (3.8)$$

$$= \pi R_{\text{tar}}^2 \left( 1 + \frac{2G(M + m_{\text{PBH}})}{R_{\text{tar}} v^2} \right). \quad (3.9)$$

However, for denser targets (such as neutron stars), general relativistic effects modifies the cross section. For a non-rotating, spherically symmetric target it can be shown that the cross section is (see appendix A.1.1)

$$\sigma = \pi R_{\text{tar}}^2 \left( 1 - \frac{2GM_{\text{tar}}}{R_{\text{tar}} v^2 \gamma^2} \right) / \left( 1 - \frac{2GM_{\text{tar}}}{R_{\text{tar}} c^2} \right), \quad (3.10)$$

where  $c$  is the speed of light in vacuum and  $\gamma$  the Lorentz factor.

### Collision rate

The differential expression for  $\Gamma$  then becomes

$$d\Gamma(v) = f_{\text{DM}} \frac{\rho_{\text{DM}}}{m_{\text{PBH}}} \left( \frac{3}{2\pi\sigma_{\text{rel}}} \right)^{3/2} 2\pi\sigma(v_{\text{rel}})v_{\text{rel}} \exp\left(-\frac{3u_{\text{rel}}^2}{2\sigma_{\text{rel}}^2}\right) u_{\perp} du_{\parallel} du_{\perp}, \quad (3.11)$$

where  $f_{\text{DM}}$  is the fraction of dark matter comprised of PBHs. We take  $f_{\text{DM}} = 1$  for most of this thesis, e.g. assuming all dark matter consist of PBHs, and only consider smaller values when we derive constraints on PBH masses. The full collision rate is then given as

$$\Gamma = \frac{\rho_{\text{DM}}}{m_{\text{PBH}}} \left( \frac{3}{2\pi\sigma_{\text{rel}}^2} \right)^{3/2} 2\pi \int \int \sigma(v_{\text{rel}})v_{\text{rel}} \exp\left(-\frac{3u_{\text{rel}}^2}{2\sigma_{\text{rel}}^2}\right) u_{\perp} du_{\parallel} du_{\perp} \quad (3.12)$$

## 3.2 Environments

There are three quantities in eq. (3.12) that depend on the environment the target is located in;  $\sigma_{\text{rel}}$ ,  $\rho_{\text{DM}}$  and  $\langle v_{\text{tar}} \rangle$ . For simplicity we start by limiting ourselves to three regions in consideration; the solar neighbourhood, the galactic centre and dwarf galaxies.

We use estimates of  $\rho_{\text{DM}}$  and the circular orbital velocity  $v_c$  from observations. From these two, the  $\sigma_v$  can be determined as follows. First, we again assume that the potential  $\Phi$  and density in all regions is spherically symmetric (only a function of  $r$ ). This then gives  $v_c$  as

$$v_c(r)^2 = r \frac{d\Phi}{dr} \quad (3.13)$$

$$= \frac{GM(< r)}{r}, \quad (3.14)$$

where  $M(< r)$  is the total mass enclosed in  $r$ . The second assumption we make is that the DM has reached dynamical (hydrostatic) equilibrium, i.e.

$$\frac{dP}{dr} = -\rho \frac{d\Phi}{dr} \quad (3.15)$$

$$= -\rho \frac{v_c^2}{r}. \quad (3.16)$$

Finally we assume the pressure  $P$  can be taken as the one of an ideal gas, which by equipartition of energy gives

$$P = \rho k_b T \quad (3.17)$$

$$= \rho \sigma_v^2. \quad (3.18)$$

Our expression for the velocity dispersion is then

$$\frac{d\rho\sigma_v^2}{dr} = -\rho \frac{v_c^2}{r}, \quad (3.19)$$

which, to reiterate, is valid for spherically symmetric potential and a DM halo that behaves as an ideal gas.

The validity of the assumption of spherical symmetry is up for debate in the galactic centre and some of the dwarf galaxies, where both the DM and component are close, but slightly deviating from spherical. The same cannot be said to be valid for the local solar neighbourhood, where the presence of the Galactic disc causes anisotropy. We emphasise that our assumption of a Maxwellian velocity distribution hinges even more strongly on spherical symmetry and an isothermal halo. Later in this chapter, we discuss the impact on our results that would arise from different velocity distributions.

### 3.2.1 Solar Neighbourhood

Any constraints on PBH masses must sooner or later rely on observations in order to be confirmed. As such, the Solar Neighbourhood (SN) is an attractive region for constraining PBHs, and DM in general. Here one can not only connect to the solar system itself, but one also have low uncertainties and completeness in stellar populations. However, the SN is not an ideal region for collisions between PBHs and stars, due to a high velocity dispersion and low DM density.

Estimating the velocity dispersion of dark matter can easily be done from the orbital velocity. The circular velocity  $v_c$  (and by extension  $\sigma_v$ ) is famously approximately constant in the SN. If  $v_c$  is constant in  $r$ , then by eq. (3.14), the total enclosed mass must be linear, and therefore the density  $\rho$  must go as  $r^{-2}$ . Taking a constant  $v_c$  and  $\sigma_v$  along with  $\rho \propto r^{-2}$  into eq. (3.19),  $v_c$  and  $\sigma_v$  are simply related as

$$\sigma_v = \frac{v_c}{\sqrt{2}}. \quad (3.20)$$

Taking the circular velocity in the SN as  $v_c = 220 \text{ km s}^{-1}$ , the velocity dispersion is the given as

$$\sigma_v = 156 \text{ km s}^{-1}. \quad (3.21)$$

For the velocities of the stars we assume that they are on circular orbits ( $\langle v_{\text{tar}} \rangle = v_c = 220 \text{ km s}^{-1}$ ), with a velocity dispersion around the mean of  $\sigma_u = 30 \text{ km s}^{-1}$ . This gives the relative velocity dispersion is

$$\sigma_{\text{rel}} = 158 \text{ km s}^{-1} \quad (3.22)$$

Unlike in the non-local environments that we discuss below, the local dark matter density is typically estimated using stellar kinematics rather than rotation curves (for review, see Read 2014, and references within). There are studies that do derive an estimate of the local DM density from rotation curve, but these rely on strong assumptions on the shape of the DM halo. Estimates from vertical kinematics of stars (eg. Garbari et al. 2012; Zhang et al. 2013; Sivertsson et al. 2018), while giving higher uncertainties, do not require such strong assumptions. These estimates rely on tracer stars to determine the vertical gravitational potential and by extension the total surface density and density. From here, estimates/assumptions on the (dominant) baryonic component is subtracted to give  $\rho_{\text{DM}}$ . Estimates of  $\rho_{\text{DM}}$  using this method range from  $0.005 - 0.015 \text{ M}_{\odot} \text{pc}^{-3}$  (again, for review: Read 2014), with the most modern estimate using SDSS-SGUE G-dwarf stars giving  $\rho_{\text{DM}} = 0.012 \text{ M}_{\odot} \text{pc}^{-3}$ . For our model, we take the local dark matter density as

$$\rho_{\text{DM}} = 0.01 \text{ M}_{\odot} \text{pc}^{-3}. \quad (3.23)$$

It has been suggested that the DM halo is slightly non-spherical (prolate/oblate) which would affect the velocity dispersion and distribution. In the case of baryons having formed discs at high redshift, some of the DM could be co-rotating with the stars in a *dark disc* (Lake 1989). These scenarios can be distinguished by comparing the  $\rho_{\text{DM}}$  estimated from vertical stellar tracers to that expected from the rotation curve, and modern estimate appears to indicate a spherically symmetric halo.

### 3.2.2 Galactic centre

The Galactic Centre (from here on GC) is most likely the region of the Milky Way that would have the highest collision rate between PBHs and the different targets. As  $\rho_{\text{DM}}$

Table 3.1: The parameters for the density profile in the GC from [Fritz et al. \(2016\)](#). The core scale  $a$  is given in arc-seconds, and converted to pc with the assumed distance from the centre to the sun  $r_\odot = 8.2$  kpc.

	Inner	Outer
$L$ [stars]	$6.73 \times 10^4$	$7.05 \times 10^6$
$a$ ["]	194	3396
$\gamma$	0.81	0

is, on average, decreasing outwards, the centre has the highest density. While the DM component is not well known, the total density can be estimated from stellar tracers.

We use the work of [Fritz et al. \(2016\)](#). Here, the stellar density profile is estimated from both the observed stellar density and the flux density. The stellar density profile is assumed to be spherically symmetric and of the form

$$L(r) = \frac{3 - \gamma}{4\pi} \frac{L}{r^\gamma} \frac{a}{(r + a)^{4-\gamma}}, \quad (3.24)$$

where  $L$  is the total star count flux, and  $a$  the scale of the core and  $\gamma$  the inner slope. [Fritz et al. \(2016\)](#) takes the profile as the sum of two profiles, one inner component and one outer, with the outer having a fixed  $\gamma = 0$ . For the fits, we choose the values based of the stellar tracer density, with the values shown in tab. 3.1. Due to the uncertainty of the distance between the sun and the galactic centre  $r_\odot$ ,  $a$  is given in arc-seconds. We convert this to pc using the distance used in [Fritz et al. \(2016\)](#),  $r_\odot = 8.2$  kpc. The above density is not the total density, but has to be scaled to match the enclosed mass  $M(< r)$ . [Fritz et al. \(2016\)](#) uses a mass to light ratio for this normalisation, scaling at  $r = 100''$  where the total mass is most known from their data. We ignore the mass to light ratio and simply normalise at  $r = 100'' \sim 4$  pc. The enclosed mass needed for the normalisation of  $\rho$ , consists of two components. One is the stellar/DM/gas component, and the second the central super massive black hole (SMBH). Using kinematic data, [Fritz et al. \(2016\)](#) related the observed velocity distribution  $\sigma_{v,o}$  to the total enclosed mass. The total enclosed mass is then given as

$$M_{\text{tot}}(r) = M_{\text{SMBH}} + M(r), \quad (3.25)$$

with the SMBH was estimated to have a mass of  $M_{\text{SMBH}} = 4.37 \times 10^6 M_\odot$ , and the mass of the stellar component is given at  $r = 100''$  as  $M_{100''} = 5.17 \times 10^6 M_\odot$ .

The circular velocity  $v_c$  and velocity distribution  $\sigma_v$ , calculated from eqs. (3.14) and (3.19) are shown on the right plot of fig. 3.1. We see that closer than 1 pc the SMBH is the dominant mass component, with the circular velocity behaving as Keplerian. At about 1 pc the stellar/DM/gas component starts to dominate the enclosed mass, and the  $v_c$  and  $\sigma_v$  is close to constant. The density profile is shown in the left hand side of fig. 3.1. We note that this is not the dark matter density  $\rho_{\text{DM}}$ , but the total mass density. As a comparison

we also show an Navarro-Frenk-White (NFW) profile (Navarro et al. 1995)

$$\rho_{\text{NFW}} = \frac{\rho_H}{\left(\frac{r}{r_H}\right)\left(1 + \frac{r}{r_H}\right)}, \quad (3.26)$$

where  $r_H$  and  $\rho_H$  are some scale radius and density taken from Nesti & Salucci (2013). The total density is on the order  $10^2$  higher than that of an NFW. Moreover, as there is a possibility of the milky way DM halo to be cored (Nesti & Salucci 2013), the DM density could be even lower. However for our purposes, we initially take the DM density to be some fraction  $\alpha$  of the total density,  $\rho_{\text{DM}} = \alpha\rho$ , with a fiducial value of  $\alpha = 0.5$ .

We assume that the velocity distribution of the stars is spherically symmetric,  $\langle v_{\text{tar}} \rangle = 0$ , with the same velocity dispersion as the DM. The resulting relative velocity dispersion is then

$$\sigma_{\text{rel}} = \sqrt{2}\sigma_v \quad (3.27)$$

For simplicity we only discuss a given region in the GC. We choose this by considering where the collision rate with low velocity PBHs are higher. In figure 3.2, the total collision rate with PBHs of velocity  $< v$  is shown for different  $v$ s, i.e eq. (3.12) integrated such that the maximum  $v_{\text{rel}} = v$ . As can be seen, the rate is the highest for low velocities at  $r \sim 1$  pc. As we ultimately want to capture the PBHs, this then gives the best case scenario, due to the highest number of low-energy PBHs. The reason for the maxima at 1 pc is a combination of that the slope of the density profile becomes steeper and velocity dispersion becomes shallower about this point. As high density and low dispersion grants more low velocity collisions the maximum is located here. Our fiducial  $\rho_{\text{DM}}$  and  $\sigma_v$  for the galactic centre are then taken as

$$\rho_{\text{DM}} = 8.17 \times 10^4 \text{ M}_\odot \text{pc}^{-3} \quad (3.28)$$

$$\sigma_{\text{rel}} = 146 \text{ km s}^{-1} \quad (3.29)$$

### 3.2.3 Dwarf galaxies

Similarly to the GC, centres of dwarf galaxies can have high DM densities, as well as even lower velocity dispersion due to the lower enclosed mass. However, there is still some ambiguity regarding the shape of dwarf galaxy DM profiles, specifically to which degree their DM profile is cored in their inner regions. The original cusp-core problem, where DM-only numerical simulations had cusps whereas observations suggested cores (Moore 1994; Flores & Primack 1994), has been mostly solved. It has now been shown that repeated bursts of stellar feedback causes a cusp to core conversion (Read & Gilmore 2005; Read et al. 2016). So, while the cusp-core problem is mostly resolved, and dwarfs should have a cored profile, the actual inner slope is time dependent (Read et al. 2016), and differs between dwarfs (Adams et al. 2014; Read et al. 2018).

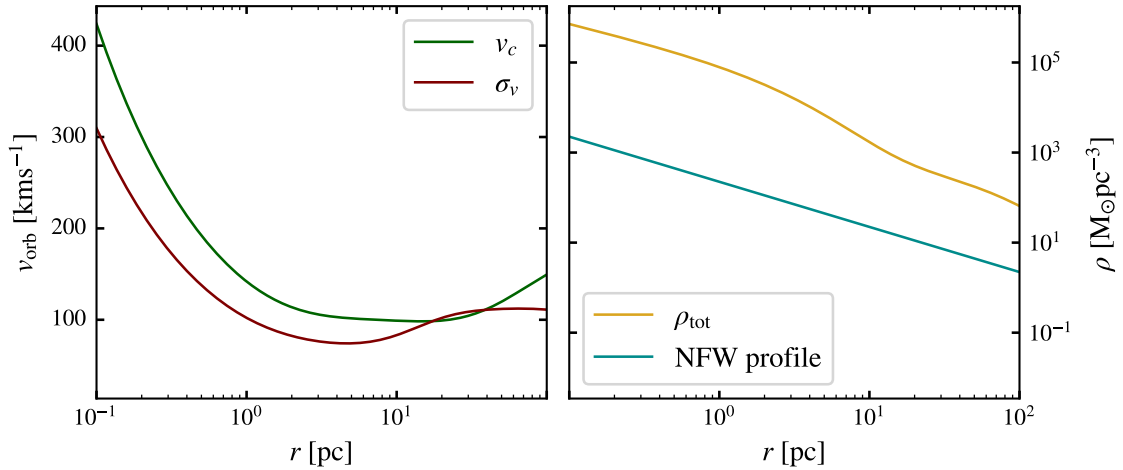


Figure 3.1: Left) The orbital velocity with respect to radius from the galactic centre, based of observational data from Fritz et al. (2016). Right) The total (gold) and a NFW DM (cyan) density profile, with the NFW profile taken from Nesti & Salucci (2013).

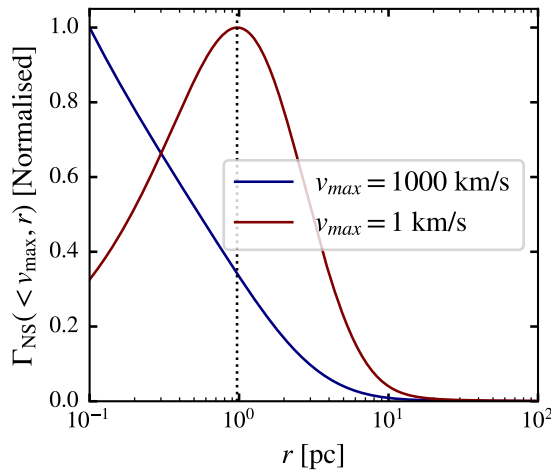


Figure 3.2: The collision rate with PBHs of velocities  $v < v_{\max}$  ( $v_{\max} = 1, 10^3 \text{ km s}^{-1}$  in red, blue respectively) in the GC as a function of radius, normalised by the maximum value.

As the centre of a dwarf galaxy is the region where the collision rate is high (due to higher  $\rho_{\text{DM}}$  and lower  $\sigma_v$ ) differences in the inner slope and concentration of DM could affect our results. Therefore, we consider three types of dwarf galaxies, dwarf Spheroidals (dSph) and Irregulars (dIrr) based of data from [Read et al. \(2018\)](#), as well as dwarf Spirals (dSpi) from [Adams et al. \(2014\)](#). Following from [Adams et al. \(2014\)](#), we model these using a generalised NFW (g-NFW) profile,

$$\rho_{\text{DM}}(r) = \frac{\delta_c \rho_c}{(r/r_H)^\gamma (1+r/r_H)^{3-\gamma}}, \quad (3.30)$$

where  $r_H$  is the scale radius,  $\gamma$  the inner slope,  $\delta_c$  the overdensity factor and  $\rho_c$  the critical density of the universe, defined as

$$\rho_c = \frac{3H^2(z)}{8\pi G}. \quad (3.31)$$

$r_H$  is given by the virial radius  $r_{\text{vir}}$

$$r_H = \frac{r_{\text{vir}}}{c}, \quad (3.32)$$

where  $c$  is the concentration parameter.  $r_{\text{vir}}$  is defined as the radius within which the average density of the halo is 200 times larger than  $\rho_c$ , which then from the virial mass  $M_{200}$  gives

$$r_{\text{vir}} = \left( \frac{3M_{200}}{4\pi \times 200\rho_c} \right)^{1/3}. \quad (3.33)$$

$\delta_c$ , the overdensity factor, is given by ([Barnabè et al. 2012](#))

$$\delta_c = \frac{200}{3} \frac{c^3}{\xi(c, \gamma, 1)} \quad (3.34)$$

$$\xi(c, \gamma, 1) = \int_0^c t^{2-\gamma} (1+t)^{\gamma-3} dt, \quad (3.35)$$

where, again  $c$  is the concentration parameter, which has an empirical form ([Dutton & Macciò 2014](#))

$$c = 0.905 - 0.101 \log \left( \frac{M_{200} h}{10^{12} \text{ M}_\odot} \right). \quad (3.36)$$

We do not consider different redshifts, and therefore take  $H(z) = H_0$ , and assume  $h = 0.7$ .

For the dSph and dIrr, we assume that the stars have a spherical velocity distribution, with the same velocity dispersion as the DM. For the dSpi, we make the approximation that all stars are on circular orbits ( $\langle v_{\text{tar}} \rangle = v_c$ ), with no velocity distribution.

The data sample from both [Adams et al. \(2014\)](#) and [Read et al. \(2018\)](#) uses HI gas and stars as tracers for the potential. [Adams et al. \(2014\)](#) fits a gNFW profile of eq. (3.30)

Table 3.2:  $M_{200}$ ,  $\gamma$ , and the dark matter density  $\rho_{100}$ , velocity dispersion  $\sigma_{100}$  of DM and circular velocity  $v_{c,100}$  at 100 pc for the dSph, dIrr (Based on [Read et al. 2018](#)) and dSpi ([Adams et al. 2014](#)).

Type	$M_{200}$ [M <sub>⊙</sub> ]	$\gamma$	$\rho_{100}$ [ M <sub>⊙</sub> pc <sup>-3</sup> ]	$\sigma_{100}$ [ km s <sup>-1</sup> ]	$v_{c,100}$ [ km s <sup>-1</sup> ]
dSph	$1.3 \times 10^9$	0.87	0.194	9.53	0
dIrr	$7.9 \times 10^9$	0.18	0.028	13.48	0
dSpi	$3.2 \times 10^{11}$	0.63	0.143	24.89	5.34

directly, giving  $M_{200}$ ,  $c$  and  $\gamma$ . [Read et al. \(2018\)](#) does not fit a gNFW profile, and does not fit  $\gamma$ , giving only an  $M_{200}$ , with  $c$  given from eq. (3.36) and a  $\gamma$  taken as the slope at 150 pc. As 150 pc is in the central region, we take this as the  $\gamma$  in eq. (3.30). Although [Adams et al. \(2014\)](#) does give a  $c$  for the dSpi, for consistency we choose to use eq. (3.36) for its determination in all galaxies.

For our models of the dwarf galaxies, we take the average of the values given in [Adams et al. \(2014\)](#); [Read et al. \(2018\)](#) for each type, found in table 3.2. As can be seen, the dSpi is more massive than the other two dwarfs, but from eq. (3.36) this does not necessarily imply higher densities. The dIrr has a shallower inner slope (and has therefore more of a core), whereas the dSpi and dSph have comparable  $\gamma$ . The velocity dispersion and density profile of the DM in dSph, dIrr and dSpi are shown in fig. 3.3. It is clear that the dSph, with its high  $\gamma$  and larger  $c$  is generally the densest of the three due to it being more cuspy. Along with this, the dSph also has the lowest velocity dispersion. The dSpi is somewhere between the dSph and dIrr in density, but at larger radii it starts to dominate, with an added increase in velocity dispersion.

Again, for simplicity, we choose a single radii for our analysis of the capture rate. As these dwarfs are not dense enough in stars (and therfore targets for PBH collisions), it makes little sense in looking at small radii. However, as the DM density is the highest, and velocity dispersion the lowest at the centre of the dwarfs, we still look in the central region (where the DM profile follows has the slope of  $\gamma$ ). At a distance  $r = 100$  pc, we can see in fig. 3.3 that all three of the dwarfs has reached their central region, so we (arbitrarily) choose this as our reference. This radius is not neccesarily the region for which the collision rate is at its maximum (in fact its not), but due the arguments above, gives us a better representation of the collision rate. With that in mind, the DM density and velocity dispersion at  $r = 100$  pc,  $\rho_{100}$  and  $\sigma_{100}$  are shown alongside the parameters in tab. 3.2.

### 3.3 Targets of PBH

We have mentioned that we want to investigate the collision between PBHs and stars, stellar remnants and planetary systems. All of these targets have different sizes  $R_{\text{tar}}$  and masses  $M_{\text{tar}}$ , which does not go linearly into eq. (3.12) due to the gravitational focusing factor. The denser an object is, the larger effect its gravitational focusing has, so the

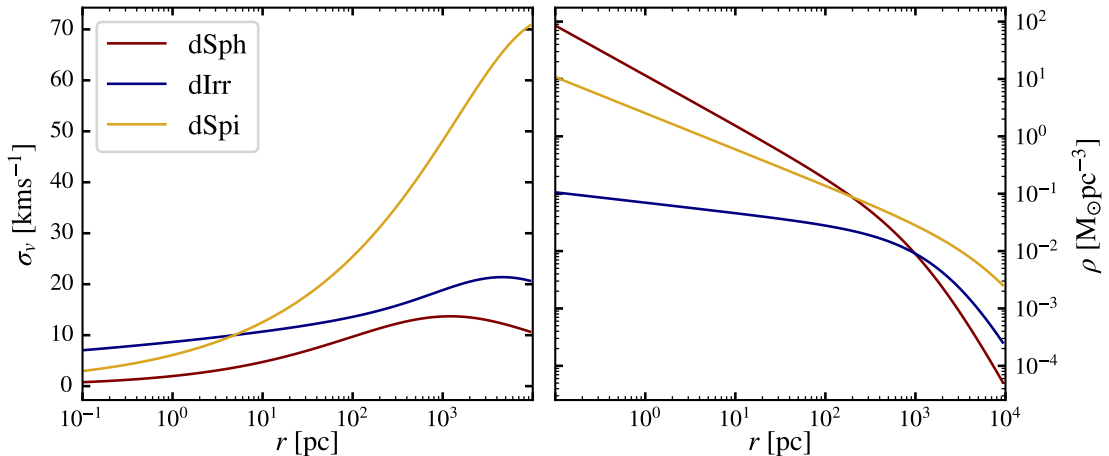


Figure 3.3: The velocity dispersion (left) and DM density (right) for the dSph (red), dIrr (blue) and dSpi (gold) dwarf galaxies. The dSph and dIrr are based of data from [Read et al. \(2018\)](#) and the dSpi from [Adams et al. \(2014\)](#).

choice of target both affects the overall collision rate with PBHs, but also at which velocity these PBHs encounter the target. The density of a given target is also important later when we consider the capture of PBHs via energy dissipation. However, unlike in other works ([Capela et al. 2013; Luo et al. 2012](#)), for simplicity we only consider uniform density profiles, and do not assume some profile based on equations of state.

The mass and radius of all targets in consideration are shown in tab. 3.3. In the rest of this section, we discuss the motivation for studying these specific targets, and the choice of their parameters.

Table 3.3: The masses  $M_{\text{tar}}$  and radii  $R_{\text{tar}}$  chosen for the different targets, eg. Main Sequence stars (MS), White Dwarfs (WD), Neutron Stars (NS), Binaries (Bi), Planets (Pl) and Planetary Systems (PS)

	MS	WD	NS	Bi	Pl	PS
$M_{\text{tar}}$	$M_\odot$	$0.5 M_\odot$	$1.4 M_\odot$	$2.8 M_\odot$	$M_\oplus$	$M_\odot$
$R_{\text{tar}}$	$R_\odot$	7000 km	12 km	$10 R_\odot$	$R_\oplus$	50 au

### 3.3.1 Stars and stellar remnants

Starting with stars and stellar remnants, we consider three types: Main Sequence stars (MSs), White Dwarfs (WDs) and Neutron Stars (NSs). MSs are natural targets for constraining DM. Not only would effects found for the MSs be observable in the Sun, allowing

for easier observations, but they are plentifully in most DM rich environments. For the MSs we take the solar values,  $R_{\text{tar}} = R_{\odot}$ ,  $M_{\text{tar}} = M_{\odot}$ . Most initial mass functions for stars gives the average MSs as lower mass (and by extension radii) than the sun, but for simplicity, and further relevance to our sun we have chosen these values.

As we describe later in this thesis, processes for capturing PBHs benefits from high densities. Both WDs and NSs are at such high densities that they need to be supported by degeneracy pressure in order to prevent gravitational collapse. As these high densities allow for higher capture rates, WDs and especially the denser NSs have been used in multiple studies attempting to constrain PBHs and other types of DM. The masses and radii for the NSs and WDs are chosen from common sense values. There is a peak in WDs mass at around  $M \sim 0.6 M_{\odot}$  ([Liebert et al. 2005](#)), and WDs radii extends up to a few hundredths of solar radii. We choose the mass and radius of WDs as

$$M_{\text{WD}} = 0.5 M_{\odot} \quad (3.37)$$

$$R_{\text{WD}} = 7 \times 10^3 \text{ km}, \quad (3.38)$$

where the mass is slightly below average, and the radius is taken as roughly  $10^{-2} R_{\odot}$ . The mass, radius and their interdependence for NSs is highly dependent on the equation of state for the NSs (for review, see [Özel & Freire 2016](#)). We chose a values for the mass and radius that roughly agree with the observations and theoretical estimates summarised in [Özel & Freire \(2016\)](#)

$$M_{\text{WD}} = 1.4 M_{\odot} \quad (3.39)$$

$$R_{\text{WD}} = 12 \text{ km}. \quad (3.40)$$

There are also reasons for investigating the *collision* (interaction) between a PBH and a binary system consisting of any combination of MS, WD and NS. This has been done in [Takhistov \(2018\)](#), where the possible transmutation of a binary companion (lets say in a NS-NS binary) would lead to a binary with a NS and a neutron star mass black hole (NSMBH), where the BH would have a mass slightly lower than a NS. The transmutation of a binary companion into a NSMBH could give a distinctive signal in LIGO/VIRGO if the binary later merged. The gravitational wavefront highly depend on the mass and radii of the target, so a NS-NSMBH could be distinguished from not only a NS-NS binary due to the smaller radii of the NSMBH, but also NS-BH binary where the BH comes from stellar evolution (eg.  $\geq 5 M_{\odot}$ ) due to the different masses.

[Takhistov \(2018\)](#) estimated that the merger rate of NS-NSMBH and other transmuted binaries would be fairly high, and should be detectable by LIGO/VIRGO. However, in their calculations, they ignored that the binary companions are orbiting each other, and only took into account the increased target mass (eg. two NS masses), doubling the collision rate. However the binaries that merge within a hubble time, must, by the Peters equations ([Peters 1964](#)) have fairly small separations ( $\sim 5 R_{\odot}$ ). As such their orbital velocities must be larger than  $250 \text{ km s}^{-1}$ . Now comparing this velocity to that in the GC or local solar neighbourhood, we see that the binary orbital velocity is similar to the galactic orbital

velocity and velocity dispersion. We investigate if the comparable binary orbital velocity increases or reduce the capture rate of PBHs. For our fiducial values, we take a NS-NS binary with a separation of

$$a = 10 \text{ R}_\odot. \quad (3.41)$$

and a mass of  $2.8 \text{ M}_\odot$ . While this binary does not merge within a hubble time, its orbital velocity is the same as the orbital velocity at the local solar neighbourhood, eg.  $230 \text{ km s}^{-1}$ .

### 3.3.2 Planetary Systems

Planets, due to their lower densities, do not have much stopping power when colliding with PBHs. Nevertheless, there has been studies on the collision between planets (namely the Earth) and PBHs. For example, [Luo et al. \(2012\)](#) did not focus on actually capturing PBHs, as this would be next to impossible, but rather calculated the gravitational energy dissipation into the Earth, and suggested that this would cause earthquakes with distinctive modes. We do not consider this aspect, but rather investigate if, similar to the binary systems, the orbits of the planets make it possible to capture PBHs. Just as an example, the orbital velocity of the Earth around the Sun is roughly  $30 \text{ km s}^{-1}$ , which while not comparable to the galactic orbital velocity, is still similar to many of the incoming PBH velocities, which could lead easier capture.

Keeping the specifics of the planetary system open for now, we consider the total mass of the system to be the mass as the central star, which is taken a MS. For the radius of the system, we do not assume a given semi-major axis of the outermost planet. Instead we simply take a radius of 50 au, similar to the Kuiper belt in our solar system. This should then cover most planetary orbits that we consider. When we later specify a system in consideration, the cross section have been adjusted to the semi-major axis of the outermost planet. For completeness we also consider a planet, specifically Earth, as a single target. While again, the Earth probably is not effective at capture PBHs, it is a useful comparison when discussing the collision rates.

## 3.4 Collision rates

The collision rate in eq. (3.12) has been calculated for all combinations of targets and environments, and the resulting values are shown in tab. 3.4 for a PBH mass of  $m_{\text{PBH}} = 10^{22} \text{ g}$ . We note that in the limit of these small PBH masses, eq. (3.12) scales inversely to  $m_{\text{PBH}}$ . In tab. 3.4, we see that in the SN, only main sequence stars and planetary systems/binaries collides with lunar mass PBHs at a rate higher than  $\Gamma \geq 0.1 \text{ Gyr}^{-1}$ . For lower PBH masses, all targets in the SN collide with PBHs at rates higher than one per age of the universe, with the Earth being hit once every 100 million years for an  $10^{16} \text{ g}$  PBH. In the galactic centre, due to the much higher dark matter density, the collision rates are high for all targets, and may therefore be relevant. All three of the dwarf galaxies have similar rates at 100 pc, varying by a order of magnitude. As the dSph has the highest  $\rho_{DM}$  and lowest

Table 3.4:  $\log \Gamma$  in inverse years for all environments and targets. The PBH mass is taken as  $m_{\text{PBH}} = 10^{22}$  g. The targets are abbreviated as Main Sequence stars (MS), White Dwarfs (WD), Neutron Stars (NS), Binaries (Bi), Planets (Pl) and Planetary Systems (PS)

Region	MS	WD	NS	Bi	Pl	PS
SN	-8.34	-10.75	-13.07	-5.45	-13.05	-0.93
GC	-1.00	-3.32	-5.64	1.39	-6.52	5.62
dSph	-5.61	-7.91	-10.23	-3.43	-12.87	-0.93
dIrr	-6.59	-8.89	-11.21	-4.41	-13.69	-1.67
dSpi	-6.27	-8.57	-10.89	-4.01	-12.80	-0.68

$\sigma_v$  at this radius, it is unsurprising that it has the highest rates. On the other hand, even though the dSpi has an order of magnitude higher  $\rho_{DM}$  than the dIrr, its higher  $\sigma_v$  gives a more comparable collision rate for targets with  $v_{esc} \gg \sigma_v$ , i.e when gravitational focusing is strong.

On the point of gravitational focusing, it has an important effect on the distribution in velocities of the PBHs that are colliding with a given target. This distribution is given by the integrand of equation 3.12 which we denote as  $\Gamma(v)$ . For a spherical distribution of stellar velocities, this is given as

$$\Gamma(v) = \frac{\rho_{DM}}{m_{\text{PBH}}} \left( \frac{3}{2\pi\sigma_{rel}^2} \right)^{3/2} 4\pi\sigma(v_{rel})v_{rel}^3 \exp\left(-\frac{3v_{rel}^2}{2\sigma_{rel}^2}\right). \quad (3.42)$$

It's important to note that  $\Gamma(v)$  is not a rate (and in fact has the unit of inverse length), but the shape of it represents the distribution in velocities. If one takes the limit of the escape velocity of the target being low (lower than  $v$ ), then  $\sigma \sim \pi R_{tar}^2$  in eq. (3.42), and in the low velocity limit,  $\Gamma(v)$  scales as  $v^3$ . In the other case, where  $v_{esc} \gg v$  then  $\sigma \propto v^{-2}$ , and  $\Gamma(v) \propto v$ . This is seen in fig. 3.4, where  $\Gamma(v)$  is plotted for a NS and a planet in the solar neighbourhood (for no circular velocity, as a demonstration). As seen the distribution for the planet peaks at  $v = \sigma_v$ , while for the NS the peak is at lower velocities. A larger fraction of PBHs that collides with a NS at low velocities than for the planet. This is important, as we wish to capture the PBHs, which is easier for small velocities due to the lower initial energy.

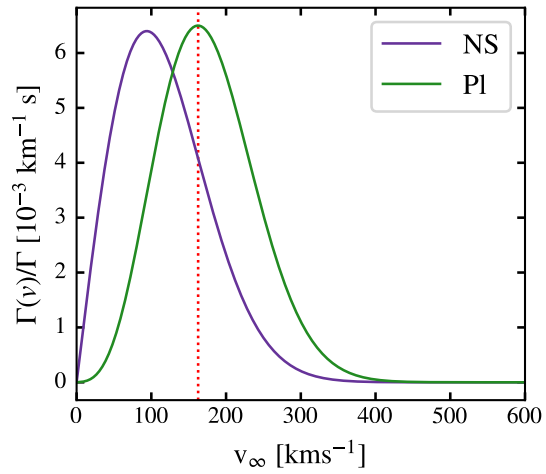


Figure 3.4: The normalised collision rate integrand for a NS (purple) and an Pl(Green) in the solar neighbourhood. The velocity dispersion is indicated with a dotted red line.

# Chapter 4

## Capturing processes

The collision rates derived in chapter 3, while high, do not necessarily have any significant consequence, as due to the small Schwarzschild radius of the low mass PBHs in consideration, the PBHs can simply fly through the target. In this chapter, we start by considering the collision of PBHs with a single target. Re-deriving and refining the model from [Capela et al. \(2013\)](#), we determine the energy loss the PBH experience due to dissipation into the medium of the target. Using this energy loss we calculate the rate at which PBHs become gravitationally bound to a target; the capture rate. A PBH that becomes bound then ends up on long elliptical orbits, going through the target, loosing further energy, and settling inside of the target. We show, using simple arguments that during the settling, due to the long orbits, there can be a significant probability that an intruding star ejects the PBH. This idea has not been considered in previous, similar studies (eg. [Capela et al. 2013](#); [Fuller et al. 2017](#); [Bramante et al. 2018](#); [Takhistov 2018](#)), and may affect their conclusions.

After this, we consider how a PBH can be captured due to the three body interaction with a stellar binary. Using numerical integration we show that the energy exchange can be significantly higher than that in single target, but can both give and take energy from the PBH. We find that the probability of a PBH gaining enough energy to be ejected is significant, and argue that therefore capturing in binaries is difficult.

### 4.1 Energy dissipation

As stated previously, the process for a singular target to capture a PBH is via the deceleration the PBH experiences as it travels through the medium of the target. The energy loss can be decomposed into two components; the accretion onto the black hole and the gravitational energy dissipation into the medium. The first of these is the most straight forward, as required by conservation of momentum, the slight increase in mass due to accretion must result in a proportional decrease in velocity. On the other hand, to model the energy dissipation requires us to model the gravitational effects the passing PBH have on the surrounding medium.

### 4.1.1 Dynamical friction

The most widely used model for the energy dissipation into the medium, developed by [Capela et al. \(2013\)](#), treats the medium of the target as individual particles. The energy dissipation thereby is modelled as dynamical friction, where the average energy/momentum exchange in scattering events leads to massive bodies slowing down as they travel through a medium of less massive bodies. This usually seen in a galactic context (see [Binney & Tremaine 2008](#)), where massive black holes or stellar clusters loses energy via the scattering of field stars. Here, however, we are considering the interaction between the PBH ( $m_{\text{PBH}} \geq 10^{16}$  g) and the particles of the target (eg. neutrons and protons inside a NS), with the deceleration coming from both the scattering and accretion of the particles.

One question that arises in regards to the validity of this model is whether the medium, of lets say a NS can be described as a collection of free particles. The particles inside of a NS is in a degenerate state of matter, making the treatment as free particles unrealistic. However, as argued in [Capela et al. \(2013\)](#), the typical velocity of a PBH as it travels through the NS is similar to the escape velocity  $v_{\text{esc}} = \sqrt{2GM_{\text{NS}}/R_{\text{NS}}} \sim 0.6 c$ , which is similar if not greater than the speed of sound in a NS ( $\lesssim c$ ). Therefore, the PBH is travelling with supersonic velocities, and one can assume that the medium does not have time to react to the interaction, allowing for the treatment of the medium as free particle. Furthermore, a limit on the scattering is imposed such that the exchange in momentum must exceed the fermi momentum  $k_f$ , defined as

$$k_f = \left( 2\pi^2 \frac{\rho}{m_n} \right)^{2/3} \hbar^2, \quad (4.1)$$

where  $\rho$  is the density of the medium and  $m_n$  the mass of a neutron. This momentum corresponds to the energy difference between the highest and lowest quantum states. So by setting  $k_f$  as the minimum allowed momentum in a scattering event, only interactions which may overcome the degeneracy of the neutrons are considered.

In the appendix of [Capela et al. \(2013\)](#), a derivation of the dynamical friction model is presented. However, the details of the derivation is not clearly explained, and in certain regions even missing. Furthermore, one of the main equations in ([Capela et al. 2013](#)) contains a mathematical singularity, specifically in their eq. (A1). This singularity does not originate from those of the PBH (which are natrual), but rather comes from the derivation itself. In order to fill in the details of the derivation, and to work around the singularity, I have re-derived the equations for the dynamical friction, which is the focus of this section.

Lets start by considering a scattering event between a PBH and an single nucleon, in a general relativistic (GR) framework. For the remainder of this section we adopt geometric units, where  $G = c = 1$ , unless explicitly stated. The largest PBHs that we consider has a Schwarzschild radius of  $\sim 10^{-6}$  m. Therefore we can consider the interaction to happen over small length scales, taking the geometry of the target to be locally flat. Assuming that the rest frame of the PBH is a free falling frame (eg. we can ignore the gravitational influence of the target body), the metric is given by the Schwarzschild metric from the PBH

(Schwarzschild 1916),

$$ds^2 = - \left(1 - \frac{R_s}{r}\right) dt^2 + \left(1 - \frac{R_s}{r}\right)^{-1} dr^2 + r^2 d\Omega^2 \quad (4.2)$$

$$d\Omega = d\theta^2 + \sin^2(\theta) d\phi^2, \quad (4.3)$$

where  $r$  is the distance to the PBH with a Schwarzschild radius  $R_s = 2m_{\text{PBH}}$ ,  $t$  is the time and  $\phi, \theta$  are spacial angles. The details of this metric can be found in any GR textbook (such as Chandrasekhar 1983; Schutz 2009), but we show summaries and derivations of the relevant equations in appendix A.1. The main equations relevant for the motion of a particle around a BH are:

$$\left(\frac{dr}{d\tau}\right)^2 = \tilde{E}^2 - 1 + \frac{R_s}{r} - \frac{\tilde{L}^2}{r^2} + \frac{R_s \tilde{L}^2}{r^3}, \quad (4.4)$$

$$\frac{d\phi}{d\tau} = \frac{\tilde{L}}{r^2} \quad (4.5)$$

where  $\tau$  is the proper time, and  $\tilde{E}$  and  $\tilde{L}$  are the specific energy and momentum of the particle, both of which are conserved.

Dividing eq. (4.4) by eq. (4.5), and changing variable to  $u = 1/r$ , one finds

$$\left(\frac{du}{d\phi}\right)^2 = R_s u^3 - u^2 + \frac{R_s}{\tilde{L}^2} u - \frac{1 - \tilde{E}^2}{\tilde{L}^2}. \quad (4.6)$$

We can describe  $\tilde{E}$  and  $\tilde{L}$  as their values at infinity, eg. in Minkowski space,

$$\tilde{E} = \gamma \quad (4.7)$$

$$\tilde{L} = v\gamma b, \quad (4.8)$$

where  $b$  is the impact parameter and  $v$  the velocity at infinity (eg. the velocity of the PBH) and  $\gamma$  its corresponding Lorentz factor. This then gives

$$\left(\frac{du}{d\phi}\right)^2 = R_s u^3 - u^2 + \frac{R_s}{b^2 v^2 \gamma^2} u + \frac{1}{b^2}. \quad (4.9)$$

$$= \left[ \gamma^2 - (1 + 2R_s \tilde{b}^2 u^2)(1 - R_s u) \right] / (R_s \tilde{b})^2, \quad (4.10)$$

where  $\tilde{b} = bv\gamma/R_s$ . Normalising  $u$  by taking  $x = R_s/r$ , one arrives at

$$\left(\frac{dx}{d\phi}\right)^2 = \left[ \gamma^2 - (1 + \tilde{b}^2 x^2)(1 - x) \right] / \tilde{b}^2. \quad (4.11)$$

As we are interested in the change in momentum of the incoming particle (which by conservation is equivalent to the change in momentum for the PBH), we need to understand

its trajectory. The maxima/minima of  $x$  (minima/maxima of  $r$ ) occurs at the zeros of eq. (4.11). As eq. (4.11) is third degree polynomial, there exists three possible zeros,  $x_1$ ,  $x_2$  and  $x_3$ , one of which is real, with the other two being either real or complex conjugate pairs. For unbound orbits, one of the roots has to be real and negative, and one can distinguish three distinct cases (Chandrasekhar 1983), which for our purposes can be described as

- Case 1) All real,  $x_1 < 0$ ,  $0 < x_2 < x_3$ : The particle comes in from infinity ( $x = 0$ ) and reaches its minimum at  $x = x_2$ .
- Case 2) All real,  $x_1 < 0$ ,  $x_2 = x_3$ : The particle comes in from infinity and asymptotically spirals inwards towards  $x = x_2$ .
- Case 3) One real,  $x_1 < 0$ , and two complex conjugate roots  $x_2, x_3$ : Starting at the infinity, the particle spirals inwards towards the singularity.

Two of these (Case 2 and 3) *unbound* trajectories end up trapped next to or inside the PBH (they are, however, still considered unbound), and therefore correspond to trajectories of particles that are accreted onto the PBH. If we fix  $v$ , the impact parameter  $b$  alone determines which case the trajectory belongs to. Importantly if  $b$  is smaller than some critical value  $b_{\text{crit}}$ , the trajectory corresponds to either case 2 ( $b = b_c$ ), or case 3 ( $b < b_c$ ).

The value of  $b_c$  for a given  $v$  is then given by equation eq. (4.11) having all real roots, with two being equal and positive. While this can then be solved using the discriminant of eq. (4.11), it should be noted that this corresponds to the extrema being a saddle point, e.g. the union of

$$\frac{dr}{d\tau} = 0 \quad (4.12)$$

$$\frac{d^2r}{d\tau^2} = 0 \quad (4.13)$$

which, by eq. (4.11) is equivalent of saying

$$U(x) = \gamma^2 \quad (4.14)$$

$$\frac{\partial U(x)}{\partial x} = 0 \quad (4.15)$$

where  $U(x) = (1 + \tilde{b}^2 x^2)(1 - x)$ . We find the value of  $b_{\text{crit}}$  that satisfies eqs. (4.14) and (4.15) as

$$\frac{b_{\text{crit}}}{R_s} = \frac{1}{v^2} \left( v^4 + \frac{5}{2}v^2 - \frac{1}{8} + \sqrt{8v^6 + 3v^4 + \frac{3}{8}v^2 + \frac{1}{64}} \right)^{1/2}, \quad (4.16)$$

where in the derivation only positive roots have been chosen, as the largest value of  $b_{\text{crit}}$  determines if an orbit is trapped. So for  $b < b_c$  the PBH accretes the incoming particles, reducing its momentum by  $\gamma v m_p$ , e.g. the momentum of the particle.

For  $b > b_{\text{crit}}$ , the particle is not accreted, but due to it being scattered, the momentum of neutron (and by conservation of momentum, the PBH) changes. The change momentum depends on the scattering angle of the interaction  $\Theta$  (see fig. 4.1). In Capela et al. (2013),  $\Theta$  is determined by inverting eq. (4.11) and integrating up to the maxima of  $x$ , eg  $x_2$ . This then gives  $\Theta$  as

$$\Theta = -\pi + 2\tilde{b} \int_0^{x_2} \frac{dx}{\sqrt{\gamma^2 - (1 + \tilde{b}^2 x^2)(1 - x)}}, \quad (4.17)$$

where the factor of 2 comes from integrating the trajectory going in and away from the PBH. However, as  $x_2$  by definition is the root of the denominator in eq. (4.17), the integral diverges. This is where the derivation of Capela et al. (2013) encounters a singularity, which originates from attempting to invert eq. (4.11), while still considering its roots.

To avoid the singularity in eq. (4.17), we follow the description found in Chandrasekhar (1983) and make some change in variables, described in appendix A.1.2. This then allows us to calculate the scattering angle as

$$\Theta = \frac{4}{\Delta} [K(k) - F(\arccos(e^{-1})/2, k)] - \pi. \quad (4.18)$$

where  $\Delta$ ,  $k$  and  $e$  are described in appendix A.1.2.  $K$  and  $F$  are the complete, and incomplete elliptic integrals which can be calculated numerically. As the difference between eqs. (4.17) and (4.18) is down to a few variable changes, we assume that Capela et al. (2013) implicitly made equivalent manipulations to avoid the singularity (as otherwise their calculations would not work), and therefore any differences between our results does not arise from differences in calculating  $\Theta$ .

The change in momentum of the particles in the rest frame of the NS can now be described in Cartesian coordinates as

$$\Delta\mathbf{p} = \gamma m_p v ((\cos \Theta - 1)\gamma, \sin \Theta, 0), \quad (4.19)$$

where  $m_p$  is the mass of the particle, and we have assumed that the PBH is travelling in the  $x$  direction. The total change in momentum over time is the sum over all interactions with the particles in the medium, i.e.

$$\frac{dp}{dt} = 2\pi \int db n b v \Delta p(b), \quad (4.20)$$

where  $n$  is the number density the particles Over multiple interactions the vertical ( $y-$ ) component of eq. (4.19) averages out and  $\Delta p(b)$  can be written as

$$\Delta p(b) = m_p v^2 \gamma^2 \begin{cases} 1 & b < b_{\text{crit}} \\ 1 - \cos \Theta(b) & b > b_{\text{crit}} \end{cases}, \quad (4.21)$$

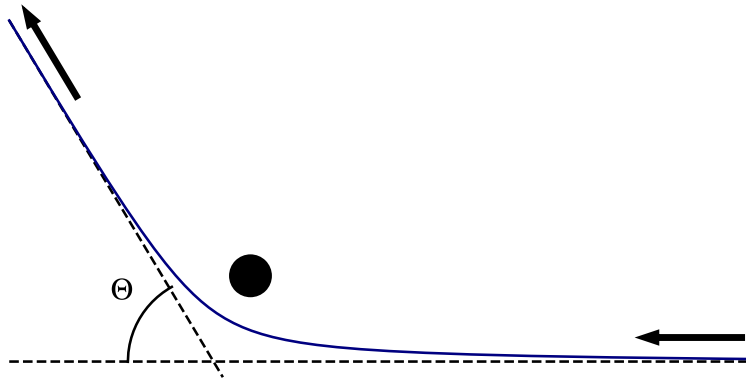


Figure 4.1: A sketch of the scattering of a particle by a PBH. The trajectory of the particle is shown in blue, with its scattering angle  $\chi$  between the asymptotic lines of the trajectory.

giving the total change in momentum, or the force acting on the PBH as

$$\begin{aligned} \frac{dE}{dl} &= 2\pi nm_p v^2 \gamma^2 \left( \frac{b_{\text{crit}}^2}{2} + \int_{b_{\text{crit}}}^{b_{\text{max}}} bdb(1 - \cos \Theta(b)) \right) \\ &= 4\pi \rho m_{\text{PBH}}^2 \frac{\ln \Lambda(v)}{v^2}, \end{aligned} \quad (4.22)$$

where we have defined an equivalence to the Coulomb logarithm  $\ln \Lambda$

$$\frac{\ln \Lambda}{v^2} = v^2 \gamma^2 \left( \frac{b_{\text{crit}}^2}{R_s^2} + \frac{2}{R_s^2} \int_{b_{\text{crit}}}^{b_{\text{max}}} bdb(1 - \cos \Theta(b)) \right), \quad (4.23)$$

and limited the allowed impact parameters to some maximum  $b_{\text{max}}$ . The value of  $b_{\text{max}}$  differs for different states of matter.

For non-degenerate matter the allowed impact parameters are simply bounded by the extent of the targets. So for a radial trajectory through a target of radius  $R_{\text{tar}}$ ,  $b_{\text{max}}$  is simply given as

$$b_{\text{max}} = \sqrt{R_{\text{tar}}^2 - r^2}, \quad (4.24)$$

where  $r$  is the current distance of the PBH to the centre. For degenerate matter, as stated before, we limit the interactions to those that exceed the fermi momentum of eq. (4.1). So combining eq. (4.1) and eq. (4.19),

$$\left( 2\pi^2 \frac{\rho}{m_n} \right)^{2/3} \hbar^2 = m_n^2 v^2 \gamma^2 \left( [1 - \cos \Theta(b_{\text{max}})]^2 \gamma^2 + \sin^2 \Theta(b_{\text{max}}) \right), \quad (4.25)$$

we get  $b_{\max}$  as

$$\cos \Theta(b_{\max}) = 1 - \frac{1}{v^2} \sqrt{1 - v^2 \left[ \frac{1 - \left(2\pi^2 \frac{\rho}{m_n^4}\right)^{2/3} \hbar^2 (1 - v^2)/v^2}{\gamma^2} + 1 \right]}, \quad (4.26)$$

where  $b_{\max}$  can be found from inverting eq. (4.18). It can happen that  $b_{\max}$  is smaller than  $b_{\text{crit}}$ . In that case we take  $b_{\text{crit}}$  as  $b_{\max}$ , and ignore the integral. We also set minimum on  $b_{\max}$  as  $R_s$ , as accretion would be unavoidable below  $b = R_s$ .

Before we move on to the full calculations, there are two important notes on eqs. (4.22) and (4.23). The first is that  $\ln \Lambda/v^2$  has been scaled, such it that can be considered independent of the mass of the black hole. This is true for degenerate matter, where  $b_{\max}$  is scaled by  $m_{\text{PBH}}$  in 4.18. In the case of non-degenerate matter  $b_{\max}$  is set by the extent of the target. However as the scattering angle scales with  $m_{\text{PBH}}$ , and is negligible at larger radii,  $\ln \Lambda/v^2$  is in practice also independent of  $m_{\text{PBH}}$  in this case. It is then always true that  $\Delta E \propto m_{\text{PBH}}^2$ .

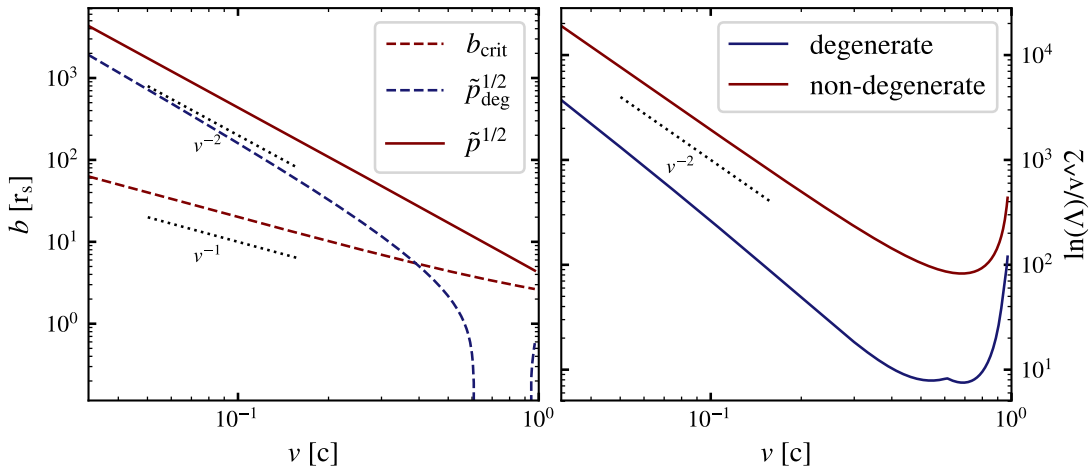


Figure 4.2: Left) the velocity dependence of the critical impact parameter  $b_{\text{crit}}$  (red dashed), the square root of the change in momentum via scattering for non-degenerate (red) and degenerate (blue dashed). Right) The coulomb logarithm with respect to velocity. Both has dashed lines indicating the dependence on velocity.

The second point is that eq. (4.22) scales as  $R_{\text{tar}}^{-2}$  for a fixed target mass and low velocities. To qualitatively see this, we make the assumption that that a PBH is on a radial trajectory through a target of mass  $M_{\odot}$ . The velocity of the PBH is of the order of the escape velocity  $v = \sqrt{2GM_{\text{tar}}/R_{\text{tar}}}$ . Now we look at eq. (4.23) for a fixed target and PBH mass, varying  $v$  (and therefore  $R_{\text{tar}}$ ). On the left plot in fig. 4.2 we show the

dependence of  $b_{\text{crit}}$  and the square root of the integral in eq. (4.23) (denoted  $\tilde{p}$ ) for both degenerate and non-degenerate matter. At high velocities, we see that for degenerate matter, the contribution from  $\tilde{p}_{\text{deg}}$  is zero, corresponding to  $b_{\text{max}} < b_{\text{crit}}$ . We note that this is only an illustration, as we scale the density of the medium with the (escape) velocity, which is not generally the case. At low velocities, both  $\tilde{p}^{1/2}$  and  $\tilde{p}_{\text{deg}}^{1/2}$  scales as  $v^{-2}$ . As can be seen in the right plot in fig. 4.2, where the full  $\ln \Lambda/v^2$  is shown, this corresponds to that both degenerate and non degenerate matter scales as  $v^{-2}$  for low velocities. Inserting this into eq. (4.22), one sees that since  $\rho \propto R_{\text{tar}}^{-3}$  and  $v^2 \propto R_{\text{tar}}^{-1}$  that

$$\frac{dE}{dl} \propto R_{\text{tar}}^{-2} \quad (4.27)$$

and since the integration path through the target is some factor times  $R_{\text{tar}}$ , qualitatively the total energy loss should be inversely proportional to  $R_{\text{tar}}$ .

## 4.2 Numerical simulations: Single targets

In Capela et al. (2013), the total loss in energy was calculated as a density weighted volume average

$$\Delta E = \frac{4\pi G^2 m_{\text{PBH}}^2}{R_{\text{tar}}^2} \int_0^{R_{\text{tar}}} dr \rho(r) r^2 \frac{\ln \Lambda(r)}{v(r)^2}. \quad (4.28)$$

Here, however, we choose to numerically integrate trajectories of PBH through a given target. By doing so we integrate eq. (4.22) for each trajectory, and therefore get the total energy loss as a function of the impact parameter of the trajectory  $b$ , and its velocity at infinity,  $v_\infty$ . As  $\Delta E$  ultimately is used in tandem with eq. (3.12), where both  $b$  and  $v_\infty$  can vary, this grants a more accurate capture rate.

### Numerical setup

We perform the integration of the trajectories of the PBHs in a general relativistic framework, looking at the energy loss from passing through a single MS, WD or NS. As the masses of PBHs that we are considering are small compared to the targets ( $\leq 10^{-10} M_\odot$  vs.  $M_\odot$ ), we can treat the PBHs as test particles. Therefore the trajectories are given by the metric  $g_{\alpha\beta}$  of the target body. Assuming that the target is spherically symmetric and non-rotating (time-independent), the metric outside of the target is simply the Schwarzschild metric, and the trajectories can be calculated as described in appendix A.1.2. Inside the target  $r < R_{\text{tar}}$ , the metric depends on the density profile, which, unlike the Schwarzschild metric, may not have a (semi-)analytic solution. As shown in appendix A.2, for a spherically symmetric, time independent metric, we can numerically solve for the trajectories by

integrating

$$\frac{dt}{d\tau} = g^{tt} \tilde{E} \quad (4.29)$$

$$\frac{d\phi}{d\tau} = \frac{1}{r^2} \tilde{L} \quad (4.30)$$

$$\frac{d^2r}{d\tau^2} = \frac{g^{rr}}{2} \left[ g_{tt}^{-2} g_{tt,r} \tilde{E}^2 + 2 \frac{\tilde{L}^2}{r^3} - g^{rr} g_{rr,r} \left( g^{tt} \tilde{E}^2 - \left[ 1 + \frac{\tilde{L}^2}{r^2} \right] \right) \right], \quad (4.31)$$

where again  $\tilde{E}$  and  $\tilde{L}$  is the specific energy and angular momentum of the test particle.

In order to integrate eqs. (4.29)-(4.31) we need the metric components for time and radius  $g_{tt}$ ,  $g_{rr}$ , and their derivatives with respect to  $r$ . As mentioned before, we take the density profile of the target to be uniform and constant,  $\rho(r) = \rho$ , and therefore the metric components inside the target is given as (Schutz 2009) (we remind the reader that we are still using geometric units,  $G = c = 1$ )

$$g_{tt} = \left[ \frac{3}{2} \left( 1 - \frac{2M_{\text{tar}}}{R_{\text{tar}}} \right)^{1/2} - \frac{1}{2} \left( 1 - \frac{2M_{\text{tar}}}{R_{\text{tar}}^3 r^2} \right)^{1/2} \right]^2 \quad (4.32)$$

$$g_{rr} = \left( 1 - \frac{8\pi\rho r^2}{3} \right)^{-1}, \quad (4.33)$$

where, again,  $R_{\text{tar}}$ ,  $M_{\text{tar}}$  is the radius and mass of the target. These components have the derivatives with respect to  $r$  as

$$g_{tt,r} = \frac{M_{\text{tar}} r}{R_{\text{tar}}^3} \left[ 1 - \frac{6}{2} \left( \frac{1 - 2M_{\text{tar}}/R_{\text{tar}}}{1 - 2M_{\text{tar}}r^2/R_{\text{tar}}^3} \right)^{1/2} \right] \quad (4.34)$$

$$g_{rr,r} = \frac{16\pi\rho}{3} \frac{r}{(1 - 8\pi\rho r^2/3)^2}, \quad (4.35)$$

giving us all the relations required in order to integrate the trajectories numerically via eqs. (4.29)-(4.31).

For the numerical integration, we initialise a given PBH at a distance  $r = 2R_{\text{tar}}$  away from the centre of the target. Here, as the geometry is given by the Schwarzschild metric, much of the derivation done in section 4.1.1 holds, but with the central object being the target (instead of a PBH). As such  $\phi$  can be calculated as described in appendix A.1.2, and we only have to separate the two cases of eq. (4.4) having all real roots, or one real and a complex conjugate pair. As in section 4.1.1, for a fixed  $\tilde{E}$ , the limit between the two cases is determined by  $b_c$  of eq. (4.16). We fix the initial velocity  $v$  (or equivalently  $\tilde{E}$ ) to a given value, and vary  $b$  in even intervals up to its maximum value, which is given by (again, see appendix A.1.1)

$$b = \left( \frac{1 - \frac{R_s}{\gamma^2 v^2 R_{\text{tar}}}}{1 - \frac{R_s}{R_{\text{tar}}}} \right)^{1/2} R_{\text{tar}}. \quad (4.36)$$

With  $v$  and  $b$  (or  $\tilde{L}$ ,  $\tilde{E}$ ) set,  $\phi$  can now be calculated, along with  $dr/d\tau$  via eq. (4.4), giving all the initial conditions.

We run multiple simulations for each target, with 500 PBHs each. For each simulation the PBHs have a fixed  $v = 1000, 10, 1, 0.1 \text{ km s}^{-1}$  and then spread the PBHs evenly in  $b$ . We integrate the eqs. (4.29)-(4.31) over  $\tau$  using the Schwarzschild metric outside of  $r = R_{\text{tar}}$  and the metric of eqs. (4.32)-(4.33) inside the target. We integrate the energy loss from dynamical friction via

$$\frac{dE}{dl} = \frac{dE}{dt} \left( \frac{dl}{dt} \right)^{-1} \quad (4.37)$$

$$= \frac{dE}{d\tau} \left( \frac{dt}{d\tau} \right)^{-1} \left( \frac{dl}{dt} \right)^{-1} \quad (4.38)$$

$$\implies \frac{dE}{d\tau} = \frac{dt}{d\tau} \frac{dt}{dl} \frac{dE}{dl}, \quad (4.39)$$

where

$$\frac{dl}{dt} = \sqrt{- \left[ 1 + g_{tt} \left( \frac{dt}{d\tau} \right)^2 \right]} \left( \frac{dt}{d\tau} \right)^{-1} \quad (4.40)$$

is the current spacial velocity. The trajectories are all integrated through the target, to when they reach  $r = 2R_{\text{tar}}$  again, with the exception of radial trajectories  $b = 0$ , where the integration diverges at  $r = 0$ . For these trajectories, we integrate down to  $10^{-14}R_{\text{tar}}$  of the centre, and stop there. The total specific energy loss is then

$$\Delta E = \int_0^{\tau_{\text{stop}}} \frac{dE}{d\tau} d\tau, \quad (4.41)$$

except for the radial trajectories, where the  $\Delta E$  is doubled, as the runs are stopped at the half way point, and the trajectories should be symmetric.

### Resulting energy loss

In fig. 4.3,  $\Delta E$  as a function of  $b$  is shown for PBHs of mass  $m_{\text{PBH}} = 10^{22} \text{ g}$  passing through a NS. There appears to be no apparent difference in  $\Delta E$  for different  $v_\infty$ , which is unsurprising due to  $v \ll v_{\text{esc}} \simeq 0.6 \text{ c}$ . One could suspect that the different trajectories should have a bigger impact, but again, this is not seen. We define the maximum and average value of  $\Delta E$  as

$$\Delta E_{\text{max}} = \Delta E(b = 0) \quad (4.42)$$

$$\langle \Delta E \rangle = \frac{1}{b_{\text{max}}^2} \int_0^{b_{\text{max}}} \Delta E(b) b db. \quad (4.43)$$

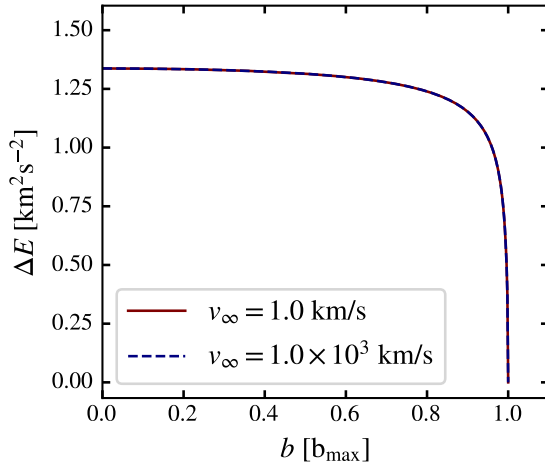


Figure 4.3: The energy loss from dissipation from one passage through a NS by a PBH of mass  $m_{\text{PBH}} = 10^{22}$  g, as function of  $b$ . The energy loss is plotted for  $v_\infty = 1 \text{ km s}^{-1}$  (red) and  $1000 \text{ km s}^{-1}$  (blue, dashed) for comparison.

We use  $\Delta E_{\max}$  as our limit when considering different initial velocities, and  $\langle \Delta E \rangle$  to discuss the general outcomes of captured PBHs. The values of  $\Delta E_{\max}$  and  $\langle \Delta E \rangle$  are found as

$$\Delta E_{\max} = \left( \frac{m_{\text{PBH}}}{10^{22} \text{g}} \right) \times \begin{cases} 1.3 \text{ km}^2 \text{s}^{-2} & \text{NS} \\ 4.2 \times 10^{-3} \text{ km}^2 \text{s}^{-2} & \text{WD} \\ 4.2 \times 10^{-5} \text{ km}^2 \text{s}^{-2} & \text{MS} \end{cases} \quad (4.44)$$

$$\langle \Delta E \rangle = \left( \frac{m_{\text{PBH}}}{10^{22} \text{g}} \right) \times \begin{cases} 0.61 \text{ km}^2 \text{s}^{-2} & \text{NS} \\ 1.8 \times 10^{-3} \text{ km}^2 \text{s}^{-2} & \text{WD} , \\ 1.8 \times 10^{-5} \text{ km}^2 \text{s}^{-2} & \text{MS} \end{cases} \quad (4.45)$$

where the scaling with  $m_{\text{PBH}}$  is implied from eq. (4.22). As suspected, the denser medium of the NS makes capturing easier by some order of magnitude. The scaling between WD and MS is also to be expected from that  $\Delta E \propto R^{-1}$ . This scaling does not hold between NS and MS/WD due to that we treat both MS/WD as non-degenerate matter. Our values of  $\langle \Delta E \rangle$  are slightly higher ( $\sim 8\%$ ) than those found in Capela et al. (2013); Takhistov (2018) ( $0.57 \text{ km}^2 \text{s}^{-2}$  for NSs), probably due to our general relativistic treatment of the trajectories through the target, and taking the target as having uniform density. However, this difference is small compared to other uncertainties in this thesis (such as the use of a Maxwellian velocity distribution for the collision rate) so we do not expect a major impact to originate from this small discrepancy.

## 4.3 Capture rate

Knowing  $\Delta E$ , we can now use equation eq. (3.12) to determine the capture rate, eg. the rate of PBHs becoming captured by the target,  $\Gamma_{\text{cap}}$ .  $\Gamma_{\text{cap}}$  is similar to eq. (3.12) but with an integration limit of  $\sqrt{2\Delta E}$ . Now as  $\Delta E$  is dependent on  $b$ , the cross section is different, with

$$\Gamma_{\text{cap}} = \frac{\rho_{\text{DM}}}{m_{\text{PBH}}} \left( \frac{3}{2\pi\sigma_{\text{rel}}^2} \right)^{3/2} 4\pi^2 \times \int_{\langle v_{\text{tar}} \rangle - \sqrt{2\Delta E_{\text{max}}}}^{\langle v_{\text{tar}} \rangle + \sqrt{2\Delta E_{\text{max}}}} \int_0^{\sqrt{2\Delta E_{\text{max}} - v_{\parallel}^2}} b_{\text{cap}}^2(v_{\text{rel}}) v_{\text{rel}} u_{\perp} \exp\left(-\frac{3u_{\text{rel}}^2}{2\sigma_{\text{rel}}^2}\right) du_{\perp} du_{\parallel}, \quad (4.46)$$

where  $v_{\parallel} = \langle v_{\text{tar}} \rangle - u_{\parallel}$ , and  $b_{\text{cap}}$  is the maximum impact parameter for capture, given by

$$\Delta E(b_{\text{cap}}) = \frac{1}{2}v_{\text{rel}}^2. \quad (4.47)$$

Now a thing to note about eq. (4.46), is that for targets with a spherical velocity distribution ( $u_{\text{rel}} = v_{\text{rel}} = v$ ), in the limit of  $v \ll \sigma_v$ , the exponential goes to 1, and  $b_{\text{cap}}^2 \rightarrow R_{\text{tar}} v_{\text{esc}}^2 / v^2$ . So for low velocities (which due to the inefficiency of the dynamical friction model, are the velocities we mostly consider),  $\Gamma_{\text{cap}}$  depends on the mass of the PBHs as

$$\Gamma_{\text{cap}} \propto m_{\text{PBH}}^{-1} \int_0^{\sqrt{2\Delta E_{\text{max}}}} v dv \quad (4.48)$$

$$\propto m_{\text{PBH}}^{-1} \Delta E_{\text{max}}, \quad (4.49)$$

and as  $\Delta E_{\text{max}}$  goes linearly with  $m_{\text{PBH}}$ , the capture rate is independent of the PBH mass. For massive PBHs, the energy loss is higher, and this approximation breaks down when  $\sigma_v^2 \sim \Delta E_{\text{max}}$ , or roughly  $m_{\text{pbh}} \sim 10^{24} \text{ g}$  for the dwarf galaxies, and  $m_{\text{pbh}} \sim 10^{25} \text{ g}$  for the milky way.

The values of  $\Gamma_{\text{cap}}$  are shown in tab. 4.1. As can be seen, the capture rates for this channel is smaller than once per 10 Gyr for all of the environments, with the possible exception of the GC if  $\rho_{\text{DM}} \gtrsim 0.1\rho_{\text{tot}}$ . For the dwarf galaxies, one can argue for that if the stellar population is of ages  $\sim 10$  Gyr years, roughly one in ten of MS, WD and NS have captured a PBH in dSph, and one in a hundred for MS and WD in dIrr and dSpi, with capturing in NS ranging down  $10^{-3}$ . In general however, this capture in single targets do not affect the stellar populations significantly, except for possibly the galactic centre. Furthermore, this is just the rate at which PBHs become gravitationally bound to the target. In order for us to convert the capture rates into settling rates, we need to understand what happens past the point of capture.

## 4.4 Settling phase

Again, following Capela et al. (2013), we now describe the trajectory of a PBH past the point of being captured by a target. As  $\Delta E$  is low compared to the energetics of the orbit,

Table 4.1: the capture rates  $\log \Gamma_{\text{cap}}$  of PBH inside of single NS, WD and MS in years for all considered environments.  $m_{\text{PBH}}$  is chosen as  $10^{22}$  g

Region	NS	WD	MS
SN	-17.37	-17.76	-17.46
GC	-9.60	-10.07	-9.78
dSph	-12.07	-12.49	-12.21
dIrr	-13.29	-13.68	-13.38
dSpi	-13.40	-13.78	-13.48

after the first passage through the target the PBH is on a highly eccentric elliptical orbit. However, as this orbit has its pericentre inside of the target, subsequent passages results in further energy loss. Taking the initial energy as  $-\Delta E$ , and approximating the orbit as radial (allowed due to the high eccentricity), the apocentre  $r_{\text{max}}$  and period  $T$  of the first orbit are given as

$$r_{\text{max}} = \frac{GM_{\text{tar}}}{2\Delta E} \quad (4.50)$$

$$T = \frac{\pi r_{\text{max}}^{3/2}}{2^{3/2} \sqrt{GM_{\text{tar}}}}. \quad (4.51)$$

As we are assuming the radial orbit, the PBH passes through the target once every half period. So the rate of energy loss can then be approximated as

$$\frac{dE}{dt} = \frac{2\Delta E}{T} \quad (4.52)$$

$$= \frac{2^{3/2} \sqrt{GM_{\text{tar}}} \Delta E}{\pi} r_{\text{max}}^{-3/2}. \quad (4.53)$$

Taking  $E = GM/r_{\text{max}}$ , one then gets

$$\frac{dr_{\text{max}}}{dt} = -\frac{2^{3/2} \Delta E}{\pi \sqrt{GM_{\text{tar}}}} r_{\text{max}}^{1/2} \quad (4.54)$$

which we write as

$$\frac{d\xi}{dt} = -\frac{1}{\tau} \sqrt{\xi} \quad (4.55)$$

$$\xi(t) = \left( \sqrt{\xi(t_0)} - \frac{t}{2\tau} \right) \quad (4.56)$$

where  $\xi = r_{\text{max}}/R$  and

$$\tau = \frac{\pi \sqrt{GM_{\text{tar}} R_{\text{tar}}}}{2^{3/2} \Delta E}. \quad (4.57)$$

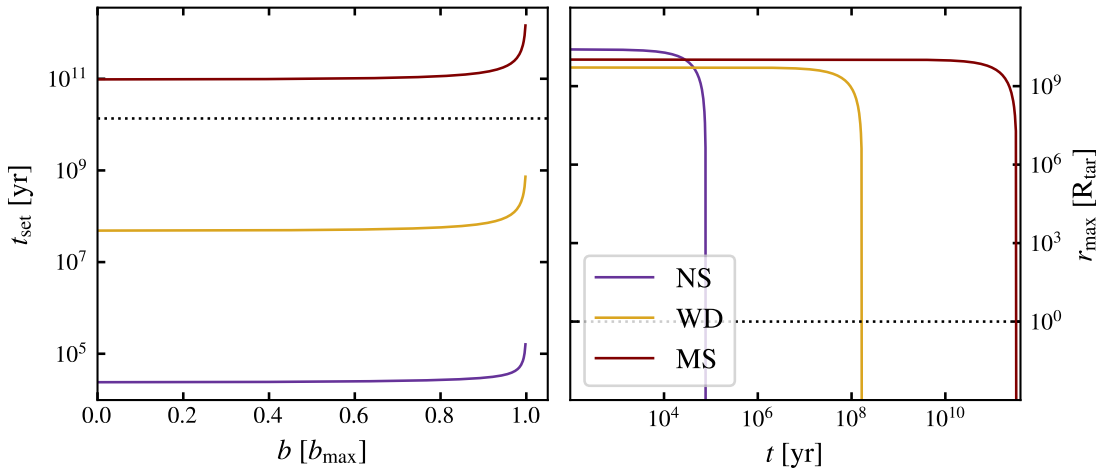


Figure 4.4: Left) The time for a PBH to be fully settle inside of the target  $t_{\text{set}}$  as a function of  $r_{\min}$  of the initial hyper/parabolic trajectory. A Hubble time is indicated with a dotted black line. Right) The maximum radius of the orbit of a PBH settling into a target as a function of time. The radius of the target is shown in a dotted black line. Both plots are shown for  $m_{\text{PBH}} = 10^{22} \text{ g}$

The time for which the orbit of the PBH is fully inside of the target, the settling time  $t_{\text{set}}$ , is then approximately given as

$$t_{\text{set}} = 2\tau\sqrt{\xi(t_0)}. \quad (4.58)$$

We note that as  $\Delta E \propto R_{\text{tar}}^{-1}$ ,  $\tau \propto R_{\text{tar}}^{3/2}$ , and therefore  $t_{\text{set}} \propto R_{\text{tar}}^{3/2}$ .

On the right plot in fig. 4.4 we show the value of  $t_{\text{set}}$  for the different impact parameters of the initial trajectory (related by  $\Delta E(b)$ ). For  $\langle E \rangle$  of 4.45 The values for  $t_{\text{set}}$  are found as

$$t_{\text{set}} = \left( \frac{m_{\text{PBH}}}{10^{22} \text{ g}} \right)^{-3/2} \begin{cases} 7.77 \times 10^4 \text{ yr} & \text{NS} \\ 1.68 \times 10^8 \text{ yr} & \text{WD} \\ 3.34 \times 10^{11} \text{ yr} & \text{MS} \end{cases} \quad (4.59)$$

We note that the average  $t_{\text{set}}$  based of  $\langle \Delta E \rangle$  matches the of values  $t_{\text{set}}(b)$ , except for the orbits with  $b \sim b_{\max}$ . For MSs, the settling time is longer than a hubble time, and therefore the PBH never settles. As  $t_{\text{set}} \propto m_{\text{PBH}}^{-3/2}$ , this is also the case for WDs and NSs for lower mass PBHs. We can define the minimum PBH mass for which the PBH can settle as

$$m_{\text{PBH}}(t_{\text{set}} = 10 \text{ Gyr}) = \begin{cases} 3.92 \times 10^{18} \text{ g} & \text{NS} \\ 6.55 \times 10^{20} \text{ g} & \text{WD} \\ 1.03 \times 10^{23} \text{ g} & \text{MS} \end{cases} \quad (4.60)$$

We see that asteroid mass PBHs can never settle, as  $t_{\text{set}}$  is too large, which also holds for the sub-lunar range settling in MSs. This has been accounted for most previous studies (eg. Capela et al. 2013).

On right plot in fig. 4.4, the evolution of  $r_{\text{max}}$  over the settling time is shown for all considered targets, with  $\Delta E = \langle \Delta E \rangle$ . The values of  $r_{\text{max}}$  for  $\Delta E = \langle \Delta E \rangle$  are found as

$$r_{\text{max},0} = \left( \frac{m_{\text{PBH}}}{10^{22} \text{ g}} \right)^{-1} \begin{cases} 9.87 \times 10^{-3} \text{ pc} & \text{NS} \\ 1.17 \text{ pc} & \text{WD} \\ 233 \text{ pc} & \text{MS} \end{cases} \quad (4.61)$$

and we see that for all targets,  $r_{\text{max}}$  is so large that we have to question whether we can treat the system as isolated. This has not been taken into consideration in the analysis of Capela et al. (2013), and we make our own analysis on this below.

If an intruding star comes close to the newly formed PBH-target binary, then there is a large probability of the PBH either getting ejected, or to be disturbed enough for its orbit not to pass through the target. In both of these cases, the settling process stops, and the PBH does not end up inside of the target. Based on fig. 4.4, the orbit of the PBH is close to  $r_{\text{max},0}$  for the vast majority of  $t_{\text{set}}$ . As the PBH spends more time further out in the orbit (lower velocities), we can estimate the average distance away from the target as the semi-major axis of the initial orbit  $a = r_{\text{max},0}/2$ , assuming an eccentricity of 1. We can then take the cross section of the PBH-target binary as  $\sigma = \pi a^2$ , and estimate the rate at which an intruding star disrupts the PBH  $\Gamma_{\text{scat}}$  as

$$\Gamma_{\text{scat}} = \pi n_* \sigma_{v,*} \frac{r_{\text{max},0}^2}{4}, \quad (4.62)$$

where  $n_*$  and  $\sigma_{v,*}$  is the number density and velocity dispersion of stars.

Based on  $\Gamma_{\text{scat}}$ , we can estimate the probability of the PBH surviving the settling phase as

$$p_{\text{set}} = \exp(-\Gamma_{\text{scat}} t_{\text{set}}) \quad (4.63)$$

$$= \exp\left(-\pi n_* \sigma_{v,*} \frac{r_{\text{max},0}^2}{4} t_{\text{set}}\right). \quad (4.64)$$

For a given environment (fixed  $n_*$  and  $\sigma_{v,*}$ ), this expression depends only on the PBH mass in consideration, with the exponent scaling as  $m_{\text{PBH}}^{7/2}$ . Due to the strong scaling with  $m_{\text{PBH}}$ ,  $p_{\text{set}}$  is either extremely close to one or zero, and there is a narrow range in  $m_{\text{PBH}}$  where it transitions between these two. We can estimate the PBH mass where the probability of being ejected becomes relevant by setting  $\ln p_{\text{set}} = 1$  and solving for  $m_{\text{PBH}}$ , giving

$$m_{\text{PBH}} (\ln p_{\text{set}} \sim 1) = \left( \frac{n_*}{\text{pc}^{-3}} \right)^{2/7} \left( \frac{\sigma_{v,*}}{\text{km s}^{-1}} \right)^{2/7} \times \begin{cases} 3.24 \times 10^{20} \text{ g} & \text{NS} \\ 4.44 \times 10^{22} \text{ g} & \text{WD} \\ 8.02 \times 10^{24} \text{ g} & \text{MS} \end{cases} \quad (4.65)$$

Below these masses, the PBHs end up on too wide orbits and are likely ejected by an intruding star.

As far as we know, no previous research mentions that the PBH are ejected during settling. We can see from eq. (4.60) and eq. (4.65) that for reasonable values of  $n_*$  and  $\sigma_{v,*}$ , this limit is much more confining than setting a maximum  $t_{\text{set}}$ . We also note that as the capture rate scales with DM density, the interesting environments are usually dense, such as the GC. However these environments can also contain a large density of stars, and therefore the limit of eq. (4.65) become relevant. For certain environments the minimum mass of PBHs that can settle can even be outside the sub-lunar mass range, and therefore deriving constraints in these regions may be impossible using the capture and settling of PBHs.

## 4.5 Capturing in binaries

In a binary system, the PBH would still experience the drag from dynamical friction. However, in the binary one can consider a different process for extracting kinetic energy from the PBH. Due to the each binary companion being in motion, the potential of the system is time dependent. This opens up the possibility that we denote as gravitational capture, where the time dependent potential can drain energy from the PBH. To see why this is the case, consider the following situation. A PBH is travelling towards a NS within a binary, such that their relative velocities are low. The two orbits (the inner between the binary companions, and the outer between the PBH and the binary) have some phase between each other  $\varphi$ . If this phase is such that just after the point of closest approach, the velocities of the PBH and the binary companion is roughly aligned, as in the sketch in fig. 4.5, then this would cause an asymmetry in the interaction.

In the specific interaction of fig. 4.5, the asymmetry is such that the PBH spends more time at closer radii from the companion when its moving away from, than when its moving towards the companion. As the acceleration goes as  $r^{-2}$ , this implies that the acceleration from the PBH coming towards the companion is lower than the deceleration moving away, meaning a loss in energy. This is sketched in fig. 4.6, where on the left side, the absolute magnitude of the acceleration ( $\nabla\Phi$ , where  $\Phi$  is the potential) is slightly asymmetric before and after closest approach, causing a net loss in velocity and thereby energy. It is important to note that the energy does not vanish, but put into the orbit of the binary. However as the PBH masses in consideration are small, this effect is negligible in the encounter.

## 4.6 Neutron star binaries

In order to test what relevance gravitational capturing has, we have developed a Fortran90 code to integrate the trajectories of PBHs through a binary. As the masses of PBHs are small compared to NSs, we can consider the PBHs as test particles, and can therefore integrate multiple at a time in order to more efficiently probe the parameters space. We

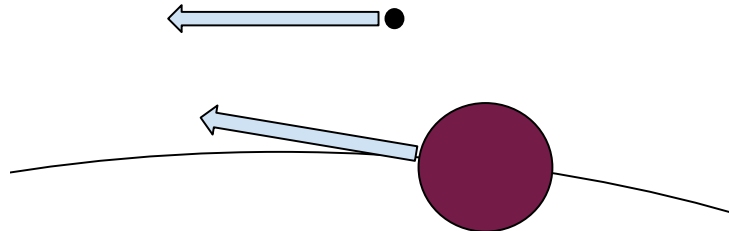


Figure 4.5: A sketch of an encounter between a PBH and a binary companion which could remove energy from the PBH.

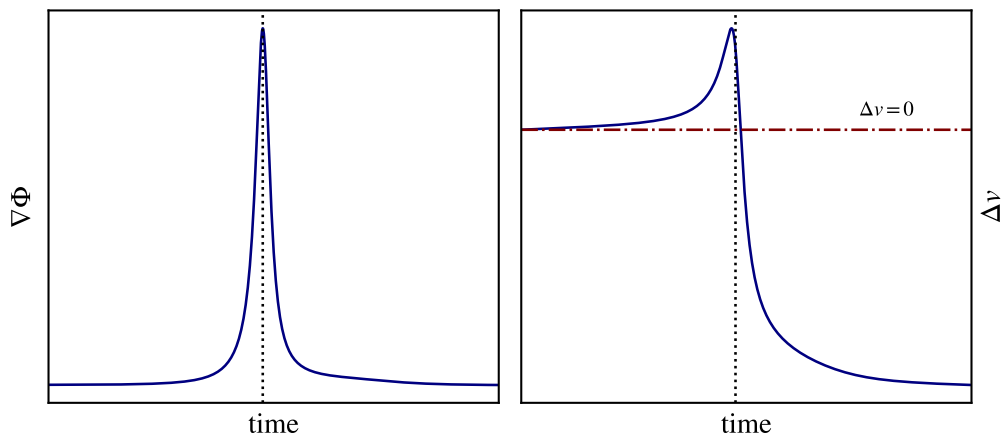


Figure 4.6: A sketch of how the asymmetry in the potential before and after closest approach might remove energy from a PBH travelling at low relative velocities to binary companion. On the left is the absolute magnitude of the acceleration  $\nabla\Phi$ , and on the right the total change in velocity  $\Delta v$ . The vertical dotted lines indicate the closest approach and the red vertical line the zero of  $\Delta v$ .

do not consider general relativistic effect, and simply integrate the positions and velocities of the PBHs in a Newtonian framework:

$$\frac{d\mathbf{x}_{\text{PBH}}}{dt} = \mathbf{v}_{\text{PBH}} \quad (4.66)$$

$$\frac{d\mathbf{v}_{\text{PBH}}}{dt} = -G \sum_{i=1}^2 \frac{M_i}{|\mathbf{x}_{\text{PBH}} - \mathbf{x}_{\text{bin},i}|^3} (\mathbf{x}_{\text{PBH}} - \mathbf{x}_{\text{bin},i}), \quad (4.67)$$

where  $\mathbf{x}_{\text{PBH}}$ ,  $\mathbf{v}_{\text{PBH}}$  is the 3D position and velocity of the PBH, and  $\mathbf{x}_{\text{bin},i}$ ,  $\mathbf{v}_{\text{bin},i}$  is the position and velocity for the binary companion  $i$ . The integration is done using a fourth order Runge-Kutta integrator with adaptive step size control ([Dormand & Prince 1980](#)).

For simplicity we do not consider elliptical binaries, nor companions of varying mass. Instead we start by looking at a circular NS-NS binary and vary the orbital velocity  $v_{\text{orb}}$ . The position  $\mathbf{x}_{\text{bin},i}$  and velocities  $\mathbf{v}_{\text{bin},i}$  of the binary companion  $i$  are then analytically computed as

$$\mathbf{x}_{\text{bin},1} = \frac{1}{2}a_{\text{bin}}[\cos(\omega t), \sin(\omega t), 0] \quad (4.68)$$

$$\mathbf{x}_{\text{bin},2} = -\mathbf{x}_{\text{bin},1} \quad (4.69)$$

$$\mathbf{v}_{\text{bin},1} = \frac{1}{2}\omega a_{\text{bin}}[-\sin(\omega t), \cos(\omega t), 0] \quad (4.70)$$

$$\mathbf{v}_{\text{bin},2} = -\mathbf{v}_{\text{bin},1}, \quad (4.71)$$

where  $a_{\text{bin}}$  and  $\omega$  is the semi major axis and orbital frequency of the binary, given by

$$a_{\text{bin}} = \frac{2GM_{\text{tar}}}{v_{\text{orb}}^2} \quad (4.72)$$

$$\omega = \frac{2v_{\text{orb}}}{a_{\text{bin}}}, \quad (4.73)$$

with  $M_{\text{tar}}$  being the mass of the individual binary companions.

### 4.6.1 Co-planar trajectories

For better understanding of when and where gravitational scattering is relevant for capturing PBHs, we do not start by considering all possible PBH trajectories. Instead we start by only considering PBH trajectories that are co-planar to the binary, eg. are on the same orbital plane. We do multiple runs with 500 PBHs each. Each run has the PBHs  $b$  and  $v_\infty$  fixed, with half of the PBHs on trajectories co/counter-rotating with the binary (eg. the angular momenta are aligned/anti-aligned with that of the binary). In each set (co/counter-rotating), we spread the PBHs in phase with the binary  $\phi$ ,  $\phi = [0, 2\pi]$ , eg. the phase of the binary at the pericentre passage of PBH. We initially set the PBHs on Keplerian parabolic/hyperbolic trajectories (considering the binary as a single point mass), with the initial separation to the binary being set as

$$\arctan\left(\frac{a_{\text{bin}}}{r}\right) = 1^\circ. \quad (4.74)$$

We choose this large initial separation simply because the binary can not be considered a point mass, only approximately so at far distances.

We vary  $b$  and  $v_\infty$  between runs.  $b$  varies such that the pericentre of the Keplerian trajectory between  $r_{\min} = 0.05 - 0.75a_{\text{bin}}$ , whereas  $v_\infty$  is varied between  $v_\infty = 0.2 - 2v_{\text{orb}}$ . All runs behaves similarly to the example in fig. 4.7, showing snapshots of a run with  $v_\infty = 0.5v_{\text{orb}}$  and  $r_{\min} = a_{\text{bin}}/2$ . As stated before the PBHs are first on Keplerian trajectories, then during the first passage, all counter-rotating PBHs gets scattered away, unbound, while some of the co-rotating PBHs loses enough energy to become bound. During subsequent orbits, the bound PBHs undergo multiple passages through the binaries. In each passage there is some probability of the PBH being scattered away on an unbound trajectory. After a few orbital periods of the binary most of the PBHs have once again been put on unbound orbit.

In order to describe the process PBHs being scattered, we look at the energy loss/gain and gained in each passage close to one of the binary companions. We define such a passage as one period of the binary, in which the PBH in question has reached a minimum distance to the companion. The energy lost/gained by the PBH is then simply the difference between the energy before and after the passage  $\Delta E$  (not to be confused with that from dynamical friction). We find the average energy difference, and its dispersion per passage as

$$\langle \Delta E \rangle = 9 \times 10^3 \quad \sigma_{\Delta E} = 6.4 \times 10^5 \text{ km}^2 \text{s}^{-2}, \quad (4.75)$$

which, while high must be compared to the energy before the passage. The distribution of  $\Delta E/E$ , where  $E$  is the energy before the passage, is shown in fig. 4.8 for co-planar ( $i = 0$ ) trajectories. Positive initial energies are separated from negative as these have different implications. For the positive initial energies, we see a spike close to zero. This is simply the PBHs whose trajectory does not change much from their initial trajectory through the binary. For the passages with  $\Delta E/E < -1$ , the PBHs loose more energy than they have, and therefore become bound to the binary.

As the PBHs are bound, they have negative  $E$ s and therefore their subsequent interactions with the binary companions are described by the red distribution in fig. 4.8. This distribution can be separated into three regimes. In the regime of  $\Delta E/E > 0$  the PBH becomes more bound, whereas in the regime of  $-1 < \Delta E/E \leq 0$  the PBH gains energy, but remains bound. The interesting regime is, again, where  $\Delta E/E < -1$ . Here the bound PBHs become unbound, and unless they have one more interaction that re-captures them, they escape from the binary. The probability of a PBH becoming rebound is (based of the  $E > 0$  distribution) low, so in most cases the PBHs escapes. This gives a simple interpretation of the decrease in captured objects: the PBH only become unbound once. The meaning of this is that a captured PBH make multiple passages through the binary, and for each minima loose/gain energy, described by the  $E < 0$  distribution. As it is more probable that the PBHs remain bound, multiple passages are common. However once a PBH has an interaction where  $\Delta E/E < -1$ , this is over; the PBH is scattered away from the binary, escaping to infinity.

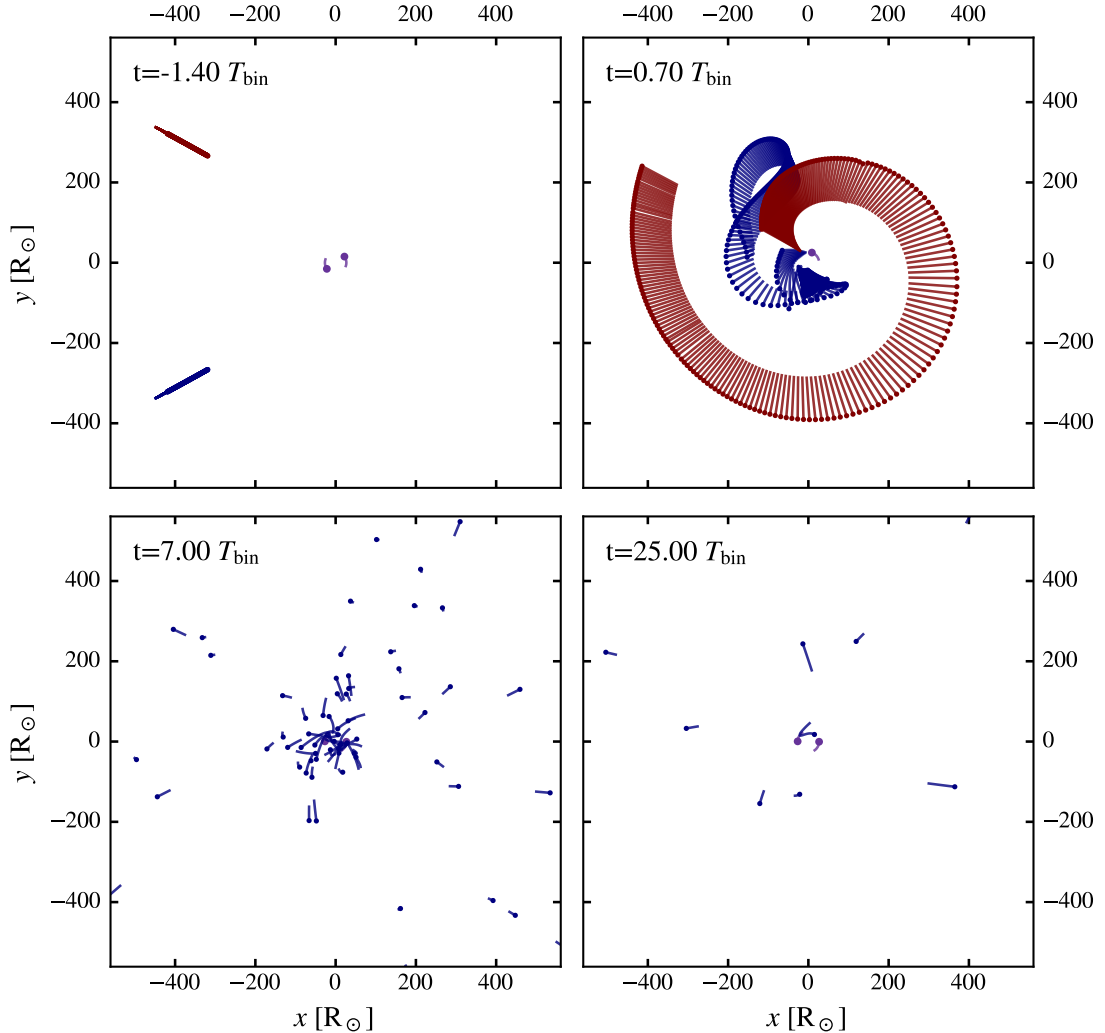


Figure 4.7: Snapshots of a NS-NS binary (purple) scattering PBHs on a co-planar trajectory with the binary. Blue PBHs has an initial trajectory having its angular momentum aligned with the binary, red PBHs anti-aligned. Top left) initial set-up, PBHs spread out on two lines, each line is separated in one period of the binary in phase. Top right) first passage through the binary. Bottom left and right) aftermath of the scattering.

We note that the energy difference in eq. (4.75) is several orders of magnitude larger than that of dynamical friction. While there is a large spread in the  $\Delta E$ , and the energy loss is most likely the highest for co-planar trajectories, it is clear that the energy loss/gain from the three body interaction dominates. Therefore the main capturing mechanism in binaries is gravitational capture rather than that of energy dissipation.

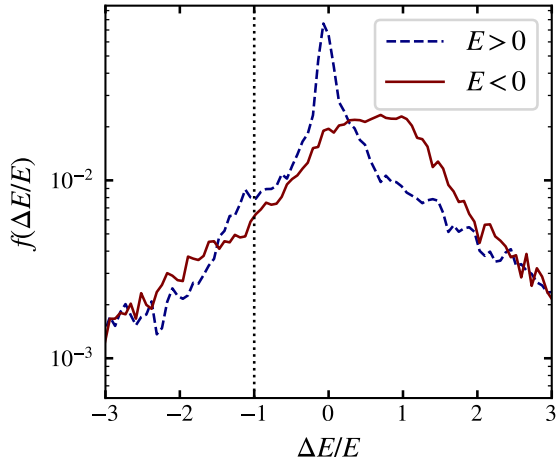


Figure 4.8: The distribution of the difference in energy  $\Delta E$  after one period in which a PBH has reached a minimum distance to one of the binary companions, normalised by the energy  $E$  before the minimum. The blue dashed shows the distribution for minima where the energy before was positive (PBH is initially unbound), and the red shows the same for bound PBHs. The vertical dotted line shows where  $\Delta E/E = -1$ , to the left of which a bound PBH becomes unbound and vice-versa.

### 4.6.2 Random trajectories

We now consider all possible trajectories through the binary. As this parameter space is now much larger than in the co-planar case, we do a monte carlo search, randomly selecting each variable. For the impact parameter  $b$  we distribute across the area of the binary, eg

$$f(b)db = \frac{1}{b_{\max}^2} b db \quad b = [0, b_{\max}]. \quad (4.76)$$

We then take the velocity from the interaction rate distribution of eq. (3.42), eg

$$f(v)dv = \frac{1}{\Gamma} d\Gamma \quad v = [0, \infty], \quad (4.77)$$

where we take the GC velocity dispersion as our fiducial value. The phase  $\varphi$  is given a uniform distribution between  $0, \pi$ ,

$$f(\varphi)d\varphi = \frac{1}{\pi} d\varphi \quad \varphi = [0, \pi], \quad (4.78)$$

such that all the phases are covered equally. As the binary is circular and symmetric (the companions are identical) there is no need to cover the range  $\varphi = [\pi, 2\pi]$ . The inclination

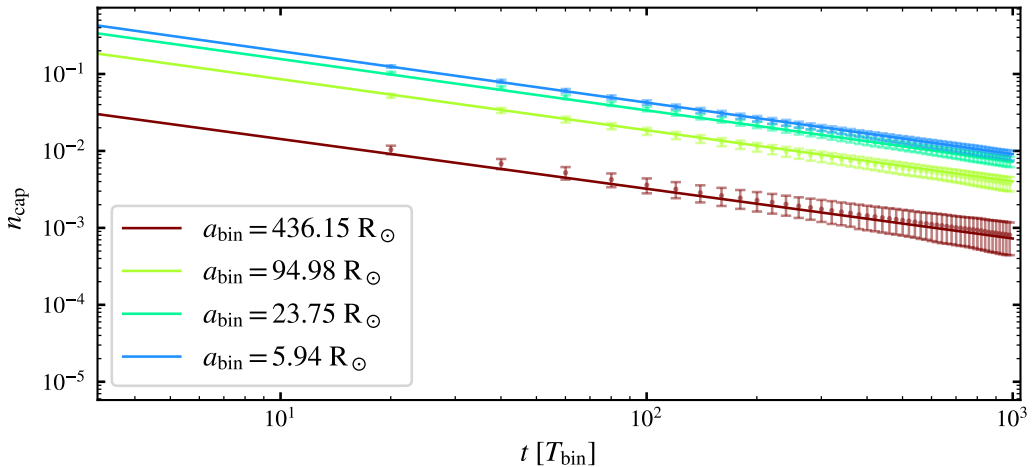


Figure 4.9: The number of captured PBHs as a function of time for different separations of the central binary  $a_{\text{bin}}$ . Dots with error bars are the simulated data points, whereas the lines are the fitted values from eq. (4.81).

$i$  and roll  $\xi$  of the PBH are distributed evenly in steradians of a half circle, again due to the circular/symmetric binary,

$$f(\xi)d\xi = \frac{1}{\pi}d\xi \quad \xi = [0, \pi] \quad (4.79)$$

$$f(i)di = \sin(i)di \quad i = [0, \pi/2]. \quad (4.80)$$

Using these distributions, we do simulations of 5000 PBHs per run.

We vary  $v_{\text{orb}}$ , and do 200 runs for each ( $10^6$  PBHs per  $v_{\text{orb}}$ ). The simulations runs for 1000 orbits of the binary past the point at which the PBHs of zero phase would reach the pericentre of their initial keplerian trajectories. We track over time how many PBHs become and remain gravitationally bound to the binary system due to the gravitational interaction, the result of this for different  $a_{\text{bin}}$  is shown in figure fig. 4.9. As can be seen, the number of PBHs captured increases with  $v_{\text{orb}}$  (decreases with  $a_{\text{bin}}$ ). However, the PBHs gets scattered away by the binary, such that the number of captured PBHs  $n_{\text{cap}}$  appears to follow a power law in time. We fit this power law as

$$n_{\text{cap}}(t) = 1.1e^{-(a_{\text{bin}}/95.2 \text{ R}_\odot)^{0.68}} \left(\frac{t}{T_{\text{bin}}}\right)^{-k(a_{\text{bin}})}, \quad (4.81)$$

where the exponent  $k(a_{\text{bin}})$  has a weak dependence on  $a_{\text{bin}}$

$$k(a_{\text{bin}}) = 0.68 - 4.98 \times 10^{-5}a_{\text{bin}}. \quad (4.82)$$

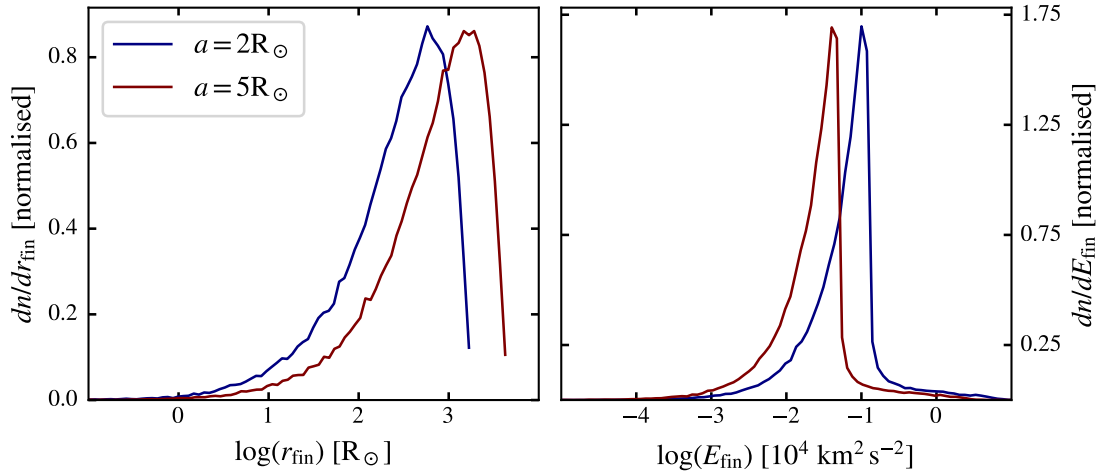


Figure 4.10: Left) The distribution of the distance away from the binary of the PBHs still bound after  $10^3 T_{\text{bin}}$  for a NS-NS binary with semi-major axis of  $2 R_\odot$  and  $5 R_\odot$ . Right) Same but with the distribution in energies.

Tight binaries then capture more PBHs, but due to their violent nature, scatter PBHs faster. We note that the fitted function can be greater than 1. This comes from that we fit the power law for times greater than  $T_{\text{bin}}$ .

Of the PBHs that still remain bound to the binary, the vast majority are found on large radii. Taking a binaries with a semi major axis of  $2 R_\odot$  and  $5 R_\odot$  as example, we can see in fig. 4.10 that most of the PBHs still bound after  $10^3 T_{\text{bin}}$  are on radii  $> 10^2 R_\odot$ . Given that the period of an orbit with semi major axis of  $a$  scales as  $T \propto a^{3/2}$ , distances this large suggests that the remaining PBHs have only passed through the binary once. The energy of these surviving PBHs, shown on the right hand side of fig. 4.10, is sharply peaked. Assuming that at each passage, the PBHs gain or loose some random amount of energy, over multiple passages, the PBHs would gain a wide distribution in energies. Therefore the peak also implies that these PBHs have only passed through the binary once. This is also supported by the fact that for the wider binary, the distribution is further out.

That most of the remaining PBHs are still on their first orbit, suggests that those PBHs that interacts multiple times gets ejected from the binary. While there still are PBHs on smaller distances and lower energies (suggesting more bound orbits), there is a large probability that these get ejected in the future. As shown by fig. 4.7, this problem is highly dependent on the initial conditions, so there it is reasonable to assume that the energy loss at a given passage is random. Therefore the PBHs at small radii can loose or gain small amounts of energy during each passage, but after some amount of passages they get ejected, as discussed previously.

We note that the only stable orbits through the binary (Eg. not an hierarchical triple)

is either a PBH that is in phase with the binary such that it never has a strong interaction, or a PBH that has settled inside one of the NSs. As the former is only possible for wide binaries and do not lead to the PBH settling inside of the target, we do not consider this type of orbit. For the latter the PBHs must have a similar velocity to the NS it has settled in (eg.  $v_{\text{orb}}$ ), and have low enough energy to be bound within a close orbit (as otherwise it would be disrupted by the companion). Taking a simple estimate of the specific energy required to be bound as

$$E_{\text{bound}} = 0.5v_{\text{orb}} - \frac{GM_{\text{NS}}}{R_{\text{NS}}} \quad (4.83)$$

$$\sim 0.1c^2, \quad (4.84)$$

we find no objects that has low enough energy to be considered bound (as for example seen in fig. 4.10).

From the arguments listed above, it is clear to us that the probability of a PBH to settle inside of a NS in a binary to be either be low or non-existent. We do not explicitly derive this probability, as none of the simulated PBHs have, or as we argue above, will settle. There is still a possibility that there exists a configuration of initial conditions that can allow for the capture and settling of PBHs. The total number of PBHs that interacts with the binary over its lifetime can be larger than our simulated sample by orders of magnitudes (see chapter 3), so a more detailed probing of the parameter space may result in the settling of some PBHs with a relevant rate. However, as we cannot determine this rate, for the remainder of this thesis we shall treat the capture and settling of PBHs in binaries as improbable.

## 4.7 Capture in planetary systems

We repeat the simulations described in the previous section, but for a planetary system similar to the Jupiter-Sun system, eg. a solar mass star with a Jupiter mass planet on a circular orbit of 5 au. We retain similar results, eg. that the PBHs do not settle inside the objects, and as the analysis is the same, we do not repeat it here for the sake of brevity.

This does however open up two points of discussion. First of, this may affect the single target capture in MSs and possibly WDs and NSs if they were to have an orbiting planet. If a PBH is captured due to energy dissipation, it has to go through several orbits in order to settle. If there is a planet in orbit around the target, the planet may scatter away the PBH, similar to our discussion in section 4.4.

The second point is that while no PBHs settle inside the star nor planet, they may end up on wide orbits. As the planetary system encounters multiple PBHs per year (see table 3.4) this may imply that there should be a large population of PBHs in orbit around the Sun today. While this would not have an impact on the solar system (the PBHs are too small to affect orbits or consume the planets/Sun), it may cause a local overdensity of PBHs. If that is the case, then it may influence observational constraints such as microlensing, due to higher density of PBHs.

However, we do not expand on these points any further, and leave this chapter by concluding that the capture and settling of PBHs in stars and planets via gravitational capture is, as with stellar binaries, improbable.

# Chapter 5

## The growth of PBH inside of stars & transient rates

So far, we have only discussed how likely it is for a PBH to be captured and settle inside of a star. As we have eluded to earlier, once a PBH has settled, it starts to consume the star, in what we denote as the growth phase. In this chapter we present a discussion on the process in which a PBH grows via accretion inside of a star, ultimately consuming the star. With some order of magnitude estimates, we show that in the final stages of this growth phase, the expected luminosity can be high, on the order of magnitude as gamma-ray bursts. With this in mind, we make a more detailed calculation of the total transient rate in a Milky Way Equivalent Galaxy (MWEG) and dwarf galaxies, estimating a cosmic transient rate on the order of 1 per year within 381 Mpc for the consumption of WDs, and 2100 Mpc for NSs. Comparing this to the expected number of events and observable events for Type Ia supernovae and gamma-ray bursts, we determine that if the transients behave as either of these events, they could be observable in current and future surveys such as the LSST ([LSST Science Collaboration et al. 2009](#)).

### 5.1 Growth of a settled black hole

Most previous studies ([Kouvaris & Tinyakov 2014](#); [Fuller et al. 2017](#); [Takhistov 2018](#)) have suggested that the growth of a small BH inside of a star is described by spherical, Bondi accretion ([Bondi 1952](#)), with a mass accretion rate of

$$\frac{dm_{\text{BH}}}{dt} = \frac{4\pi\lambda\rho_c G^2 m_{\text{BH}}^2}{c_s^3}, \quad (5.1)$$

where  $m_{\text{BH}}$  is the mass of the BH,  $\rho_c$  the central density of the star,  $\lambda$  a parameter depending on the equation of state of the medium, and  $c_s$  the sound speed of the medium. This growth is rapid, with a  $10^{22}$  g black hole consuming a NS on timescales of  $\sim 0.01$  yr ([Fuller et al. 2017](#)), practically negligible compared to the timescale of the settling phase of the PBH.

However, for the BH to grow with this rapid accretion, it must not to be limited by angular momentum or radiation pressure.

As we showed in the previous chapter, NS are the most viable candidate for capturing and settling PBHs inside of them. Therefore throughout this section we focus on the transmutation of NS, with the differences for MS and WD being mentioned at the end.

### 5.1.1 Angular momentum

As stars inevitably have some rotation, the medium accreted onto the BH has a non-zero angular momentum. Assuming that stars rotate as solid body with a angular frequency  $\omega$ , the specific angular momentum  $l$  of a parcel of the medium at a distance  $r$  from the centre is given as

$$l = r^2 \sin^2 \theta \omega, \quad (5.2)$$

where  $\theta$  is the angle to the spin-axis. This angular momentum is conserved during the accretion, barring transfer of angular momentum outwards, so the parcel reaches some radius  $R$  away from the BH where it is supported by its angular momentum. Assuming the parcel is on a circular orbit at this point, the angular momentum at this orbit is given as

$$l_{\text{circ}} = R v_{\text{circ}} \quad (5.3)$$

$$= \sqrt{GM_{\text{enc}}R}, \quad (5.4)$$

where  $M_{\text{enc}}$  is the total mass enclosed inside  $R$ . Demanding that  $l = l_{\text{circ}}$ ,  $R$  can be found as

$$R = \frac{r^4 \sin^4 \theta \omega^2}{GM_{\text{enc}}}. \quad (5.5)$$

If this  $R$  is found outside of the radius of the Innermost Stable Circular Orbit  $r_{\text{ISCO}}$  of the BH, the accreted matter forms an accretion disc, which significantly reduce the mass accretion rate.

Assuming that all matter inside of  $r$  has already been accreted onto the BH,  $M_{\text{enc}} \approx m_{\text{BH}}$ , and we can relate  $r$  to  $m_{\text{BH}}$  as

$$m_{\text{BH}} = \frac{4\pi r^3}{3} \rho + m_{\text{PBH}} \quad (5.6)$$

$$r = \left( \frac{3}{4\pi\rho} (m_{\text{BH}} - m_{\text{PBH}}) \right)^{1/3}, \quad (5.7)$$

where  $\rho$  is the density of the star (again assumed to be constant) and  $m_{\text{PBH}}$  is the initial (P)BH mass. Inserting eq. (5.7) into eq. (5.5), we can estimate  $R$  as a function of the BH mass:

$$R(\theta, m_{\text{BH}}) = \left( \frac{3}{4\pi\rho} \right) \frac{(m_{\text{BH}} - m_{\text{PBH}})^{4/3}}{Gm_{\text{BH}}} \sin^4 \theta \omega^2. \quad (5.8)$$

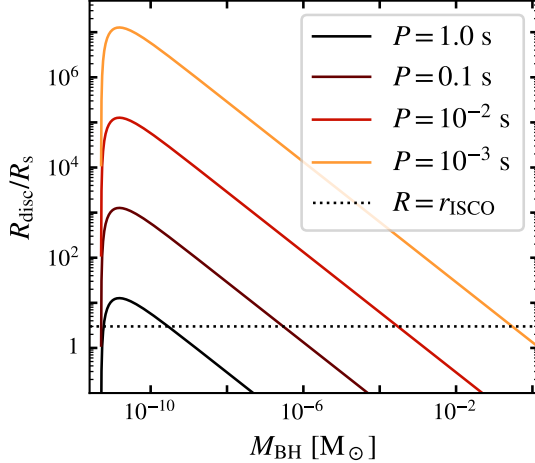


Figure 5.1: The size of the accretion disc that forms around a BH during the transmutation of a NS, normalised by the Schwarzschild radius of the BH. The dashed line indicates the innermost stable orbit for a non-spinning BH, below which a disc is unable to support itself.

Material falling in from the rotation plane of the star ( $\theta = \pi/2$ ) settles on the edge of the disc, so we define the outermost radius of the disc,  $R_{\text{disc}} = R(\pi/2, m_{\text{BH}})$ . To compare how  $R_{\text{disc}}$  behaves with respect to the growth of the BH, in fig. 5.1 we show the ratio between  $R_{\text{disc}}$  and the Schwarzschild radius of the BH with an initial mass  $m_{\text{PBH}} = 10^{22}$  g. The star is taken as a NS, with varying rotational periods  $P = 2\pi/\omega$ . We see that for  $P > 0.1$  s,  $R < r_{\text{ISCO}}$  for most masses, where  $r_{\text{ISCO}} = 3R_s$  for a non-spinning BH, and therefore the accretion is only limited by a disc for the initial accretion stages. For shorter periods, however, the accretion goes through a disc for most  $m_{\text{BH}}$ . Furthermore, as the BH is spun up by the accreted material,  $r_{\text{ISCO}}$  decreases down to  $R_s$  for a maximally spinning BH. Therefore disc accretion becomes even more frequent, however only slightly.

It has been suggested that the viscosity of the medium efficiently transports angular momentum outwards (Markovic 1995). This not only alleviates the problem of limiting the accretion due to material forming a disc, but also keeps the BH from becoming maximally rotating, which would also limit the accretion (Kouvaris & Tinyakov 2014; Fuller et al. 2017). Kouvaris & Tinyakov (2014) suggests that Bondi accretion is never stopped as long as

$$\left(\frac{P}{1 \text{ s}}\right) \left(\frac{T}{10^5 \text{ K}}\right)^{-2/5} \geq 4.1 \times 10^{-3}, \quad (5.9)$$

where  $T$  is the temperature of the NS. For NSs that does not satisfy eq. (5.9), Bondi

accretion would still be limited in the final stages of the consumption, above masses of

$$m_{\text{BH}} \geq 1.7 \times 10^{-3} \left( \frac{P}{1 \text{ s}} \right)^{1/3} \left( \frac{T}{10^5 \text{ K}} \right)^{-4/3} M_{\odot}, \quad (5.10)$$

but as the growth to this point is rapid, the timescale at which NSs are consumed are still short.

It should be noted that the requirement for Bondi accretion depends on the rotational period of the NS. As NSs are formed by collapsing stars, and retains much of the angular momentum of the progenitor they can initially have short periods. Misalignment between the spin axis and the magnetic dipole moment of these NS causes radiation, which we observe as pulses, and have therefore named these objects Pulsars (for review, see [Lorimer 2005](#)). The radiated energy is taken from the rotation, increasing the period of these pulsars. The ratio between the period  $P$  and the its rate  $\dot{P}$  gives a timescale for which a pulsar is spun down.

Observationally we know of two, fairly distinct populations of pulsars, regular pulsars and Millisecond Pulsars (MSPs). Regular pulsars rotate with  $P \sim 0.1 - 10$  s and are spun down on timescales of  $0.1 - 100$  Myr, whereas MSPs both rotate at rapidly  $P \sim 1 - 10$  ms and are spun down slowly, with timescales of  $\sim$  Gyrs. As we saw in the previous chapter, the capture rates of PBHs by NS is at best  $\sim \text{Gyr}^{-1}$ , so we can assume that a regular pulsar that have captured a PBH has already spun down to the point that angular momentum does not inhibit Bondi accretion. MSP pulsars on the other hand are still a concern in this regard. Only a fraction  $\sim 10\%$  of pulsars are found as MSP, and these are typically associated with pulsars in binaries. As we showed in the previous chapter, capturing PBHs in binary systems is highly improbable, and therefore we dont expect the MSP that are in binaries to capture PBHs. However, there are observed isolated MSPs, so we may have to consider NSs with short rotational periods.

### 5.1.2 Radiation pressure

The other issue that we have to address is the fact that the infaling material releases some of the gravitational energy as radiation. This radiation couples to the electrons of the medium resulting in an outward force proportional to the outgoing flux. If this force is larger than the gravitational force of the BH, accretion is halted. Therefore one can derive a maximum luminosity for accretion; the Eddington luminosity, defined as:

$$L_{\text{edd}} = \frac{4\pi G m_{\text{BH}} c}{\kappa}, \quad (5.11)$$

where  $\kappa$  is the opacity of the medium.

By conservation of energy arguments, one can say that a fraction  $\eta$  of the rest energy of the infalling matter is converted into radiation, or

$$L = \eta \frac{dm_{\text{BH}}}{dt} c^2. \quad (5.12)$$

If we assume the BH is accreting via a disc, a particle accreted from infinity has to reduce its potential energy. Half of this energy goes into kinetic energy to keep the particle in a circular orbit, implying that the other half is lost to radiation, eg

$$L = \frac{Gm_{\text{BH}}}{2r_{\text{ISCO}}} \frac{dm_{\text{BH}}}{dt} \quad (5.13)$$

$$= \frac{R_s}{4r_{\text{ISCO}}} \frac{dm_{\text{BH}}}{dt} c^2 \quad (5.14)$$

which for a non-spinning black hole implies an efficiency  $\eta \sim 0.08$ . While this is a simplified model for the emitted luminosity, it is useful for order of magnitude estimates.

Equating the luminosities, the maximal accretion rate is then given by

$$\frac{dm_{\text{Edd}}}{dt} = \frac{4\pi Gm_{\text{BH}}}{\eta\kappa c}. \quad (5.15)$$

For typical values for ionised hydrogen, and an  $\eta = 0.08$ , this gives a timescale for a  $m_{\text{PBH}} = 10^{22}$  g to consume the star on the order of Gyr. Comparing this to the timescale derived from the Bondi accretion implies that the accretion is severely constrained by the Eddington limit.

As the Eddington limit is dependent on the opacity, we need to estimate  $\kappa$  for the nuclear matter of a NS. Ignoring a possible quark-gluon plasma phase in the centre, the matter in NS is dominated by neutrons. However, the competing processes of  $\beta$ -decay and inverse  $\beta$ -decay, along with electron/positron capture implies some equilibrium between the number of protons, neutrons and electrons (and other particles). While the exact ratios for equilibrium depend on the models used for the equation of state, typical values for the fraction of protons and electrons lie in the range of  $f_e = f_p \sim 0.1 - 0.01$  (see, eg. [Rosswog & Davies 2002](#)). As electrons dominate in the absorption of photons, the opacity inside the NS  $k_n$  can be approximated as

$$k_n = \frac{\sigma_T f_e}{(m_p f_e + m_n (1 - 2f_e))}, \quad (5.16)$$

where  $\sigma_T$  is the cross section for Thomson scattering, assumed to be dominant, and  $m_p$  the proton mass. As  $f_e$  can be one or two magnitudes lower inside NSs than that of ionised hydrogen, its easy to see that the opacity is lower for the nuclear matter, and therefore the Eddington accretion rate is higher, due to less efficient absorption.

The decrease in opacity for nuclear matter only increases the possible accretion rate by a few orders of magnitude, which is still not enough in order for accretion with the Bondi rate. [Kouvaris & Tinyakov \(2014\)](#) suggested that the Eddington limit can be ignored entirely. Their arguments are based on the fact that the Bondi accretion is supersonic below radii of

$$r_b = \frac{Gm_{\text{BH}}}{4c_s^2}. \quad (5.17)$$

For  $c_s = 0.17c$ ,  $r_b = 4.3r_s$ , and therefore the matter reaches supersonic speeds before being absorbed into the BH. [Kouvaris & Tinyakov \(2014\)](#) continues by arguing that the mean free path for photons  $l$  is much smaller than  $r_b$ . The mean free path of the photons

$$l = \frac{1}{\kappa\rho} \quad (5.18)$$

which is of the order of femto-metres for  $f_e = 0.1$ ,  $\rho \sim 10^{14} \text{ g cm}^{-3}$ , or roughly the Schwarzschild radius of a  $10^{15} \text{ g}$ , i.e. several orders of magnitude lower than  $r_g$  for the BH masses considered here  $> 10^{19} \text{ g}$ .

Eq. 5.18 changes somewhat due to the electrons being in a degenerate state, however the conclusion is the same;  $l \ll r_b$ . This implies that radiation emitted below  $r_g$  is absorbed into the supersonic flow, which [Kouvaris & Tinyakov \(2014\)](#) argues causes the injected energy to be swept along into the BH. However, we argue that radiation from outside  $r_g$  would still limit accretion. As  $r_g$  is only a few Schwarzschild radii, this can account for a significant amount of the luminosity. Therefore, material outside of  $r_g$  still would reach a maximum accretion rate, limiting the accretion as a whole.

The idea of the radiated energy being trapped into the BH was originally described in [Begelman \(1979\)](#). Instead of  $r_g$ , the radius inside of which radiation is trapped,  $r_{\text{tr}}$  is defined by the distance where the infall speed of the material is equal to the radiation diffusion speed, giving

$$r_{\text{tr}} = \frac{\dot{m}_{\text{BH}}}{\dot{m}_{\text{Edd}}} \frac{R_s}{2}, \quad (5.19)$$

where dots indicate time derivatives. Inserting the Bondi accretion rate of eq. (5.1) and the Eddington mass accretion of eq. (5.15) retrieves

$$r_{\text{tr}} = 2.4 \times 10^7 R_s \left( \frac{\lambda}{0.707} \right) \left( \frac{\kappa}{\kappa_n} \right) \left( \frac{\eta}{0.1} \right) \left( \frac{c_s}{0.17c} \right)^{-3} \left( \frac{\rho}{10^{14} \text{ g cm}^{-3}} \right) \left( \frac{m_{\text{BH}}}{10^{22} \text{ g}} \right), \quad (5.20)$$

which is significantly higher than  $r_g$ , and therefore the accretion could be practically unlimited by radiation pressure. For large BH masses, this expression reaches radii outside of the NS. But as the density decreases rapidly at large radii (the crust and exterior of the NS) this converges to values smaller than  $R_s$ .

There is a question if the photon trapping described above is in a stable state, and is not episodic in nature. Self-consistent numerical simulations ([Ohsuga et al. 2005; Inayoshi et al. 2016](#)) have confirmed that this effect can lead to super-Eddington limit accretion. Specifically [Inayoshi et al. \(2016\)](#) found that the accretion is stable if

$$\frac{dm_{\text{BH}}}{dt} \gtrsim 5 \times 10^3 \frac{dm_{\text{Edd}}}{dt}, \quad (5.21)$$

below this value, the accretion is episodic, with an average accretion rate of  $\sim 10L_{\text{Edd}}/c^2$ . As seen by eq. (5.20) (the ratio between the two accretion rates), for the initial mass of

the BH and up to the point that the outermost region of the NS is accreted, the accretion always satisfies eq. (5.21) and therefore the accretions should proceed with the Bondi rate in the spherical accretion case. It should be noted that these simulations were made using stellar mass BHs or above, accreting gas from densities more similar to the denser regions of the interstellar medium (number densities of  $\sim 10^5 \text{ cm}^{-3}$ ). As such, the application of these results to a low mass BH accreting nuclear density matter might be dubious.

As the accretion would not be spherical due to angular momentum it is unclear if the conditions for photon trapping is met. Any accretion disc forming may or may not flow inwards with velocities smaller than the diffusion speed of the radiation, and could therefore be disrupted due to the high radiation from the accretion of low angular momentum material. This may affect how the NS is consumed overall, as the material of the disc would interact with the infalling, low angular momentum matter. If there is sufficient interaction between the material forming a disc and the infalling material, the flow of the infalling material might be disturbed to the point at which efficient photon trapping becomes unfeasible.

### 5.1.3 Possibility of collapse

It should be noted that all of the above discussion has ignored that the BH is accreting from within a pressure supported star, not a infinite medium that is often assumed in the accretion models. Specifically for NSs, which are supported by degeneracy pressure, this might change the picture of how the BH accretes. Consider the particles close to the centre, and lets say they are in equilibrium before the BH has entered. They all exert degeneracy pressure onto each other, and as they are in equilibrium, the pressure must counteract the gravitational pressure. If suddenly a  $10^{22} \text{ g}$  BH is put in the centre and consumes the neutrons within and immediately around it, the degeneracy pressure surrounding the BH drops. Therefore the previously negative pressure gradient becomes positive, and neutrons are pushed towards the BH via pressure in addition to the gravitational force. This could cause a rarefaction wave propagating outwards, with all matter flowing towards the BH hydrodynamically, possibly triggering a collapse.

The collapse described above would be subject to the same limitations of conservation of angular momentum and radiation pressure, but these limitations would be altered. As the infalling particles are subject travelling downwards a pressure gradient, the velocity required to be on a circular orbit is super-Keplerian. Therefore the radius for which a particle with angular momentum settles on a circular orbit is smaller than described in section 5.1.1. Similarly the pressure gradient (force) implies that more radiation is required in order to counteract both the gravitational and hydrodynamical force that the flow is subject to.

In order for this collapse to actually occur, the initial accretion surrounding the PBH needs to decrease the immediate surrounding density, as otherwise degeneracy pressure is restored. If the accretion follows the Bondi description, this is not the case, as the density of the infalling flow increases for smaller radii ([Bondi 1952](#)). How the initial stages of accretion behaves is therefore key to understanding how a PBH consumes a star (accretion

flow vs. collapse). Similarly during the collapse, the infalling matter is compressed (via the continuity equation) causing the pressure to increase, possibly making the situation quasi-stable, returning to regular bondi accretion.

We do not know of any studies on this (very specific) situation, and we do not pursue this idea further, as it is outside of the scope of this thesis. Studying the structure of NS in general is usually done via general relativistic numerical integration (see, eg. [Belvedere et al. 2012](#); [Cipolletta et al. 2015](#)) or hydrodynamical simulations ([Rosswog & Davies 2002](#)), and it is not apparent that linear simplifications are precise enough in order to estimate the effect of removing degeneracy pressure in small region around the BH. Likely this may require general relativistic, magneto-hydrodynamics, with relevant included physics in order to properly study. Due to lack of knowledge, we leave this idea for possible future research, and assume that the PBH consumes the star via (spherically symmetric or disc) accretion.

Ignoring the effect described above, the assumption that the star is accreted on to the PBH rather than collapse is most likely a good approximation, as the added mass (the BH) is not large enough on its own to cause a collapse. Furthermore, as the star is in equilibrium before this point, its gravitational pressure cancels the hydrodynamical or degeneracy pressure. Therefore, these pressures can mostly be ignored (assuming that they do not change) and the accretion should follow the accretion described earlier.

### 5.1.4 Consumption time and possible transients

As has been discussed in this section, there are uncertainties in how a PBH consumes a NS. Depending on the rotation of the star, an accretion disc may or may not form. If the accretion is spherical, it is probably accreting at super-Eddington rates in a stable state, and not periodically. If the angular momentum of the infalling material is large enough such that a disc is formed, the accretion rate follows the evolution of the disc, and may or may not be Eddington-limited. The disc accretion might even be higher than the Eddington rate due to photon trapping, or other mechanisms (see [Mayer 2018](#), and references therein).

If we assume the accretion rate of a possible disc to be the Eddington limit of eq. (5.15), we can estimate a timescale for the disc to accrete  $\tau_{\text{disc}}$ . Integrating the Eddington rate,  $\tau_{\text{disc}}$  becomes

$$\tau_{\text{disc}} = \frac{\eta \kappa c}{4\pi G} \ln \left( \frac{M_{\text{NS}}}{m_{\text{PBH}}} \right) \quad (5.22)$$

$$\approx 5.2 \times 10^7 \text{ yr.} \quad (5.23)$$

where the numerical value is for  $m_{\text{PBH}} = 10^{22} \text{ g}$ ,  $\kappa = \kappa_n$  for  $f_e = 0.1$ , and  $\eta = 0.08$ . Similarly, the timescale to accrete via Bondi accretion  $\tau_b$  is given by integrating eq. (5.1):

$$\tau_b = \frac{c s_s^3}{4\pi \lambda G^2 \rho} \left( \frac{1}{m_{\text{PBH}}} - \frac{1}{M_{\text{NS}}} \right) \quad (5.24)$$

$$\approx 0.038 \text{ yr,} \quad (5.25)$$

where values has been takes as  $c_s = 0.17c$ ,  $\lambda = 0.707$  and  $\rho$  as average density of a NS.

Note that the timescale of the disc accretion is not the timescale for the star to contract. As a spherical shell of the star is not stable if the mass interior to it has either been accreted or fallen onto a disc, it also should fall inwards. Therefore ignoring viscosity, and other interactions between the infalling material due to asymmetry, the star contracts on a time scale similar to that of Bondi accretion  $\tau_b$ .

As the timescales of Bondi accretion and disc accretion differ by multiple orders of magnitude, not only are these processes are completely disconnected, but during the disruption of the NS, the Bondi accretion is the main mode of consumption. Depending on the rotation of the NS is either completely accreted onto the BH, or only partially accreted, with the non-accreted matter forming an accretion disc around the BH. If we assume that the matter that is being accreted onto the BH is not disturbed by the matter forming a disc, and that the arguments for why the accretion is not Eddington limited still holds, then the BH grows rapidly, swallowing the innermost regions of the disc.

When the outermost regions of the NS are starting to fall inwards, the density of the flow drops sufficiently for the radiation, that previously was trapped, to escape. This results in an increase in luminosity at breakout  $L_{\text{break}}$ . We can estimate this luminosity by assuming that it arises from the infall of the last layer of the dense core (eg. still the average density of the NS). Via eqs. (5.1) and (5.12), assuming that the BH has consumed most of the NS, the break out luminosity then becomes

$$L_{\text{break}} = \eta \frac{4\pi G^2 \rho_{\text{NS}} M_{\text{NS}}^2}{c_s^3} c^2 \quad (5.26)$$

$$\approx 10^{26} \eta L_\odot \quad (5.27)$$

where  $L_\odot = 3.833 \times 10^{33}$  erg  $s^{-1}$  is the Solar luminosity. We note that this luminosity is an upper limit, as the density decreases rapidly outside of the core, implying that luminosities would be lower by multiple orders of magnitude. Furthermore, as the medium is still optically thick, the photons would take some time to actually escape from the infalling crust of the NS which would reduce the luminosity by spreading out the energy release temporally. However taking this as an order of magnitude estimate, we see that these events would be similar, if not brighter in luminosity than gamma-ray bursts (cf. [Tsutsui et al. 2013](#)).

If a disc does form, and is neither disrupted by radiation or swallowed by the growth of the BH, then the disc may still be around after the breakout of radiation. The disc would then be accreted on the long time scale, at a significant fraction of  $\tau_{\text{disc}}$ . The accretion disc would be radiating at luminosities at close to the Eddington luminosity, which assuming a BH mass of  $m_{\text{BH}} = M_{\text{NS}}$ , and  $\kappa = \kappa_n$ , is given as  $L_{\text{Edd}} \sim 10^6 L_\odot$ . This would be an interesting event, as it would have a unique observational signal. The accretion would most likely give a similar signal to low mass x-ray binaries, but without binary orbital motions. However it is uncertain that a disc survives the BH growth and the resulting radiation, and we cannot rely on this situation occurring. Therefore we chose to only consider the breakout luminosity described above as an observational signal.

### 5.1.5 White dwarfs and Main sequence stars

We can translate the previous discussion on the consumption of NSs to WDs and MSs by considering three aspects. The first two are, as with the previous discussion, whether the accretion is limited by angular momentum and radiation pressure.

The discussion on angular momentum still holds here, and the ratio of the radius of a possible accretion disc, and the growing Schwarzschild radius,  $R_{\text{disc}}/R_s$  is monotonically decreasing with the growth of the BH, for BH masses larger than the initial mass (see fig. 5.1). Therefore we need only to consider  $R_{\text{disc}}$  of the final accreted mass to see if there is some major difference to NS:

$$R_{\text{Disc}} = \frac{R_{\text{tar}}^4 \omega^2}{GM_{\text{tar}}} \quad (5.28)$$

The period for a typical WD is on the order of 1 day (see [Kawaler 2003](#), and references therein), and we take the rotational period of MSs as the period of the sun,  $\sim 24$  days, (inaccurately) assuming a solid body rotation ([Snodgrass & Ulrich 1990](#)). Comparing to a 1 s period NSs,  $R_{\text{disc}}$  is retrieved as

$$R_{\text{Disc}} = R_s \times \begin{cases} 1.1 \times 10^{-6} & \text{NS} \\ 1.3 \times 10^{-4} & \text{WD} \\ 5.5 & \text{MS} \end{cases} \quad (5.29)$$

and we can see that the accretion of a WD is similar in angular momentum to that of a NS rotating with a period of  $1 - 0.1$  s, whereas MSs appears to always form a (small) disc.

The second question is then if the accretion is Eddington limited. Once again we look at the trapping radius of eq. (5.20), and the Bondi accretion rate of eq. (5.1). Assuming an adiabatic factor  $\gamma = 5/3$ , the structure constant is  $\lambda = 1/4$ . The adiabatic sound speed can be estimated from

$$c_s^2 = \gamma \frac{P}{\rho} \quad (5.30)$$

For WDs the pressure is dominated by non-relativistic electron degeneracy pressure,

$$P_{\text{WD}} = \frac{8\pi}{15h^3m_e} k_f^5 \quad (5.31)$$

$$k_f = \left( \frac{3n_e}{8\pi} \right) h, \quad (5.32)$$

where the the number density of electrons  $n_e \sim \rho/m_p$ , and  $k_f$  the Fermi momentum. For MSs we approximate the pressure as the central pressure, given numerically for a star with a polytropic structure as ([Privalnik 2009](#))

$$P_{\text{MS}} = 0.206 \times (4\pi)^{1/3} GM_{\text{MS}}^{2/3} (5.991\rho)^{4/3}. \quad (5.33)$$

With these pressures,  $c_s$  is given as

$$c_s \approx \begin{cases} 6400 \text{ km s}^{-1} & \text{WD} \\ 1000 \text{ km s}^{-1} & \text{MS} \end{cases}, \quad (5.34)$$

which then corresponds to a trapping radius of

$$\frac{r_{\text{tr}}}{R_s} = \frac{m_{\text{BH}}}{10^{22} g} \times \begin{cases} 5200 & \text{WD} \\ 2.7 & \text{MS} \end{cases}. \quad (5.35)$$

If we assume the same condition for stable super-Eddington growth via photon trapping as found in Inayoshi et al. (2016) ( $r_{\text{tr}} \geq 2500R_s$ ), we see that for WDs we are close to limit, whereas for MSs  $r_{\text{tr}}$  is well below. This implies that the growth in MSs is most likely limited to the Eddington accretion rate, and therefore the consumption is slow, whereas for WDs it's very much unclear, as the assumptions done here could overestimate  $r_{\text{tr}}$ . For simplicity we assume that accretion in WDs is not Eddington limited.

The third aspect that we should discuss when considering growth inside MSs and WDs, is if nuclear fusion becomes relevant during the consumption. When the BH starts accreting material, both the density and the temperature of the material increases. Along with further heating from the released radiation, there is a possibility for nuclei to fuse. This can significantly increase the radiation release, which not only affects the radiation pressure (and therefore accretion) but also trigger further nuclear reactions, and turn into a runaway nuclear event. If the energy release from the fusion is high enough to counteract the accretion onto the BH, it might disrupt the star, in an event similar (if not identical) to a type Ia supernova in the case of WDs. This has implications on the observational signal, as if the accretion of a WD results in a type Ia supernova, then it is (as far as we can tell) indistinguishable from regular type Ia supernovae.

Assuming that no nuclear reactions occur in the accretion, we can estimate the timescale of consumption and breakout luminosity for the consumption of WDs in the same way as for NSs, granting

$$\tau_{\text{c,WD}} \approx 1.5 \times 10^4 \text{ yr} \quad (5.36)$$

$$L_{\text{break,WD}} \approx 4 \times 10^{18} \text{ L}_\odot. \quad (5.37)$$

The consumption takes longer for WDs than for NSs due to the lower densities. The lower mass accretion rate also gives lower breakout luminosities, which maximum estimate is now lower than for gamma-ray bursts.

For MSs the consumption and transient is much less clear, as not only is a disc likely to form, but the accretion is limited via radiation pressure. As such it is likely that the timescale for the star to be consumed by the BH is closer to that enforced by the Eddington limit, giving on average lower luminosities.

However, the accretion can still be above the Eddington limit in bursts, not allowing for the easy "behind the envelope" calculations that have been used in this section to estimate

the breakout luminosity. However we can still put a lower and upper bound on  $L_{\text{break}}$  by considering the minimum as that of  $L_{\text{Edd}}$  and the maximum of that corresponding to Bondi accretion. The consumption timescale and breakout luminosity can therefore be estimated as

$$\tau_{\text{c},\text{MS}} \approx 0.98 \text{ Gyr} \quad (5.38)$$

$$L_{\text{break},\text{MS}} \sim 10^4 - 10^{15} \text{ L}_\odot, \quad (5.39)$$

where the matter of the MS has been assumed to be ionised hydrogen. The combination of the long timescale for consumption with the long timescale for settling and the corresponding high probability of breakup described in section 4.4 makes MS a poor candidate for capturing, and being consumed by PBHs. The uncertainty in breakout luminosity is also detrimental in attempting to derive constraints from these events. We therefore do not consider main sequence stars beyond this point and focus only on NSs and WDs.

## 5.2 Consumption probability

Having some idea of what happens when a target is consumed by a PBH, in this section we estimate the probability of a given (singular) object to have been consumed by the current age of the universe  $p_{\text{cons}}$ . Following from Capela et al. (2013) the probability of a target having captured a PBH follows an exponential decay

$$p_{\text{cap}} = 1 - \exp(-T_{\text{tar}}\Gamma_{\text{cap}}), \quad (5.40)$$

where  $T_{\text{tar}}$  is the age of the target. Now as shown in section 4.4, it takes some time for the PBH to settle inside, which limits the available time for PBHs to be captured, resulting in the consumption probability given in Capela et al. (2013):

$$p_{\text{cons}} = 1 - \exp(-[T_{\text{tar}} - t_{\text{set}}]\Gamma_{\text{cap}}), \quad (5.41)$$

where  $t_{\text{set}}$  is given by eq. (4.59), and  $T_{\text{tar}} - t_{\text{set}} > 0$  is implicitly assumed.

However as we showed in section 4.4, the PBH-target binary can be vulnerable to disruption from intruding stars.  $p_{\text{cons}}$  is therefore modified to include the settling rate of PBHs:

$$p_{\text{cons}} = 1 - \exp(-[T_{\text{tar}} - t_{\text{set}}]\Gamma_{\text{set}}) \quad (5.42)$$

$$= 1 - \exp(-[T_{\text{tar}} - t_{\text{set}}]p_{\text{set}}\Gamma_{\text{cap}}), \quad (5.43)$$

where  $p_{\text{set}}$  is given by eq. (4.64). Further including that it takes some time for the targets to consume the target, the final consumption probability is given by

$$p_{\text{cons}} = 1 - \exp(-[T_{\text{tar}} - t_{\text{set}} - \tau_{\text{c}}]p_{\text{set}}\Gamma_{\text{cap}}). \quad (5.44)$$

This differs from the probability given in Capela et al. (2013) in two ways. The first, being quite minor assuming old targets, is the inclusion of  $\tau_{\text{c}}$ . As  $\tau_{\text{c}}$  is short for both

WDs and NSs we don't expect this to affect the probability significantly. The second, and more important difference, is the inclusion of the scatter probability. As mentioned before this has either been neglected, or completely missed in previous studies, and as showed in section 4.4, becomes significant for the relevant PBH masses  $m_{\text{PBH}} = 10^{20} - 10^{23} \text{ g}$ .

As we know that targets such as NSs and WDs exists, we know that eq. (5.44) cannot be close to 1 (as otherwise there would be no NSs or WDs). This is equivalent of saying that the absolute value of the argument in the exponent must not be larger than order unity, eg.

$$[T_{\text{tar}} - t_{\text{set}} - \tau_c] p_{\text{set}} \Gamma_{\text{cap}} \leq 1. \quad (5.45)$$

Remember that so far in  $\Gamma_{\text{cap}}$ , we have ignored the fraction of DM that consists of PBHs,  $f_{\text{DM}}$ . Denoting  $\Gamma_{\text{cap},1} = \Gamma_{\text{cap}}(f_{\text{DM}} = 1)$ , we are then able constrain the abundance of PBHs as

$$f_{\text{DM}} \leq \frac{1}{[T_{\text{tar}} - t_{\text{set}} - \tau_c] p_{\text{set}} \Gamma_{\text{cap},1}}. \quad (5.46)$$

We see that as this constraint scales with the inverse of  $\Gamma_{\text{cap},1}$ , this constraint is only strong for large values of  $\Gamma_{\text{cap},1}$ . As was shown in section 4.3, this is practically only true for targets inside of the galactic centre (given that  $T_{\text{tar}} < 10 \text{ Gyr}$ ). Therefore we can only constrain PBH masses based of the survival in the galactic centre, which is the focus of the remainder of this section.

### 5.2.1 Neutron star survival in the Galactic centre

Remembering that the capture rate in the GC is high based of the high density of matter, of which some fraction  $\alpha$  is DM, where  $\alpha$  was chosen as 0.5, its clear that the stellar density is also high ( $\sim 10^4 \text{ M}_\odot \text{ pc}^{-3}$ ). This implies that the number density of stars is high, and therefore the probability of the PBH being ejected during settling can be significant. On examination of eq. (4.65), a stellar number density on the order of  $n_* \sim 10^4 - 10^5 \text{ pc}^{-3}$  increases the mass for which PBHs survive the settling phase in WDs to values beyond what we are interested in  $m_{\text{PBH}} \leq 10^{23} \text{ g}$ . Therefore we only consider NS in deriving this constraint.

Using the density and velocity profiles for the GC shown in section 3.2.2, we construct a mass weighted average of the settling rate within a radius  $r$  of the GC:

$$\langle \Gamma_{\text{set}} \rangle = \frac{4\pi}{M(<r)} \int_0^r \rho(r) p_{\text{set}} \Gamma_{\text{cap}} r^2 dr. \quad (5.47)$$

For the ratio between stars and and DM we once again use  $\alpha = 1/2$  where  $\rho_{\text{DM}} = \alpha \rho$ . For  $p_{\text{set}}$  we again assume that the stars have the same velocity dispersion as the DM, and that the stellar number density can be estimated as  $n_* = \rho_*/\langle m_* \rangle$ , where  $\langle m_* \rangle \approx 0.25 \text{ M}_\odot$  is the average stellar mass based of a salpeter IMF (Salpeter 1955).

We estimate the fraction of dark matter that can be occupied by DM via eq. (5.46) for a given PBH mass, assuming an average NS age of 5 Gyr. The resulting constraint is shown for multiple radii in fig. 5.2. We see that any significant constraints on PBH masses are based of the survival of NS inside of  $r < 10$  pc. This poses the first problem with this constraint, that there might be a lack of pulsars in the central parsecs of the galactic centre (Dexter & O’Leary 2014). While the lack of observed pulsar could be an indication that PBHs have depleted the NS population, other, less exotic explanation exists (Dexter & O’Leary 2014; Rajwade et al. 2017). Instead, the missing pulsars has the consequence that the constraint derived here can only be relevant if the missing pulsar problem is resolved.

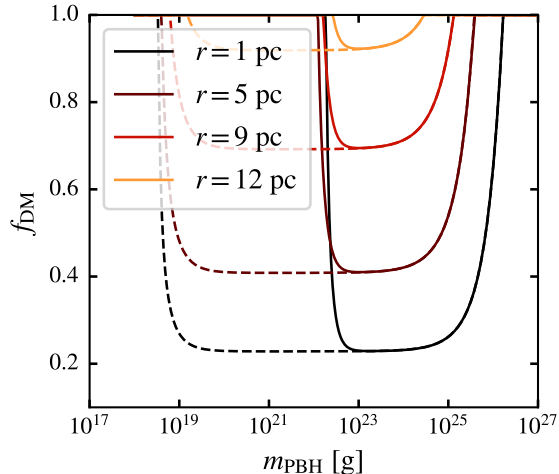


Figure 5.2: The limits on PBH that can be derived based on NS survival within a radius  $r$  of the GC, assuming that DM makes up half of the total matter. The solid lines take into account that the PBH can be scattered away by intruding stars during settling, whereas the dashed lines ignore this possibility.

In fig. 5.2 we also see that due to the large density of stars,  $p_{\text{set}}$  becomes significant. As  $p_{\text{set}}$  sets the lower limit on the mass range that can be constrained, this limits the constraint to PBH masses. To illustrate the significance  $p_{\text{set}}$  has, the constraints that would be derived ignoring  $p_{\text{set}}$  is also shown in fig. 5.2. We see that ignoring  $p_{\text{set}}$  the constraints reaches down to PBH masses of  $10^{19}$  g, where  $t_{\text{set}} = T_{\text{tar}}$ , whereas including  $p_{\text{set}}$  stops the constraint at  $10^{23}$  g. This becomes relevant when considering that microlensing constraints are currently effective down to  $10^{22} - 10^{23}$  g (Niikura et al. 2019a), meaning that the constraint derived here is redundant.

Finally we have to consider that we may have been to generous with the dark matter mass fraction in the GC  $\alpha$ . While the actual value is unknown,  $\alpha = 1/2$  is most likely to high. It is easy to show from equation 5.46 that the PBH DM fraction is inversely proportional to  $\alpha$  ( $f_{\text{DM}} \propto \alpha^{-1}$ ), and therefore even lowering the DM mass fraction to

$\alpha \sim 0.01$  would completely remove the constraints of fig. 5.2.

## 5.3 Transient rates

As shown in the previous section, constraints based of the galactic centre are either too weak or irrelevant due to previous constraints from microlensing. As this was the only region where capture rates are high enough in our model to reliably capture PBHs in any target, this excludes any further constraints based of the survival of these targets. However, in dwarf galaxies, and even in the Galaxy, the capture rates are high enough, that when taking into account the large amount of targets, several consumption events could be happen within the life time of the galaxies. This section explores this idea by further by estimating the transit rate, assumed to be equal to the settling rate, for the Milky Way Equivalent galaxy (MWEG) and dwarf galaxies.

### 5.3.1 Milky way equivalent galaxy

To make a better estimate on the total capture/settling rate of PBHs in a given target, we adopt a galactic model of a bulge, disc and halo. For the bulge we assume a Hernquist stellar profile

$$\rho_b(r) = \frac{M_b}{4\pi a^3} \frac{1}{r/a(1+r/a)^3}, \quad (5.48)$$

where  $r$  is the distance from the galactic centre,  $M_b = 1.6 \times 10^{10} M_\odot$  is the mass of the bulge and  $a = 600$  pc, with the numerical values taken from ([Sartore, N. et al. 2010](#)). For the disc we adopt a Miyamoto-Nagai disc ([Miyamoto & Nagai 1975](#))

$$\rho_d(R, z) = \frac{b^2 M_h}{4\pi} \frac{aR^2 + [a + 3(z^2 + b^2)^{1/2}] [a + (z^2 + b^2)^{1/2}]^2}{\left( R^2 + [a + (z^2 + b^2)^{1/2}]^2 \right)^{5/2} (z^2 + b^2)^{3/2}}, \quad (5.49)$$

where  $R$  and  $z$  are the cylindrical coordinates of the galaxy, and  $a = 3.7$  kpc is the scale length of the disc,  $b = 200$  pc is the scale height, and the  $M_h = 8 \times 10^{10} M_\odot$  is the total mass of the disc. The specific values for the parameters are taken from ([Paczynski 1990](#)). We describe the halo in two parts: the DM halo and the stellar halo. We choose the DM halo to be described by an NFW profile

$$\rho_{h,DM}(r) = \frac{\rho_0}{r/r_0(1+r/r_0)^2}, \quad (5.50)$$

where  $\rho_0 = 7.9 \times 10^{-3} M_\odot \text{ pc}^{-3}$  and  $r_0 = 20 \text{ kpc}$ . For the stellar halo we chose the observationally fitted profile from (Kafle et al. 2014)

$$\rho_{\text{h},*}(r) \propto \begin{cases} (r/r_1)^{-2.4} & r < r_1 \\ (r/r_1)^{-4.5} & r_1 < r < r_2, \\ (r_2/r_1)^{-4.5} (r/r_2)^\epsilon \exp\left(-\frac{r-r_2}{\Delta}\right) & r > r_2 \end{cases} \quad (5.51)$$

where  $r_1 = 17.2 \text{ kpc}$ ,  $r_2 = 97.7 \text{ kpc}$ ,  $\Delta = 7.1 \text{ kpc}$  and  $\epsilon = r_2/\Delta - 4.5$ . For the normalisation to this profile, we chose the mass of the stellar halo to be  $M_{\text{H},*} = 5 \times 10^8 M_\odot$  (see Bland-Hawthorn & Gerhard 2016, and references therein).

Using the above density profiles, we derive the velocity profiles as described in section 3.2. For simplicity we choose to define the circular velocity as its value at in the disc plane

$$v_c(R, z) = v_c(R, 0, 0). \quad (5.52)$$

As the disc is most likely the important region (due to the larger number of stars) this simplification should not influence our results significantly. We make a further approximation by setting the velocity dispersion as  $\sigma_v = v_c/\sqrt{2}$ , rather than fully calculating it. In these estimates we ignore the stellar halo, as it is insignificant compared to the other components.

In order to estimate the galactic settling rate, we need the spatial distributions of our targets, NSs and WDs. For WDs we assume that they follow the stellar density profile (disc+bulge+stellar halo). We can then describe the number density of WDs as

$$n_{\text{WD}} = \frac{N_{\text{WD}}}{M_{\text{tot},*}} \rho_{\text{tot},*}(R, z), \quad (5.53)$$

$$= N_{\text{WD}} f_*(R, z), \quad (5.54)$$

where  $M_{\text{tot},*}$  and  $\rho_{\text{tot},*}$  is the total stellar mass and density, and  $f_*$  is what we define as the fractional number density of stars (units  $\text{pc}^{-3}$ ). For NSs we need to take into account that they receive a kick in their birth. For this reason we make a neutron star population synthesis, described in appendix B, to estimate the distribution of NS in the galaxy.

As the distribution of NSs cannot be simply functionally estimated, we instead choose to divide the galaxy into bins of  $R$  and  $|z|$  (axis symmetry), between  $0 - 40 \text{ kpc}$  in each. As the regions most dense in stars are the most interesting, we construct a refinement tree to increase the resolution where the most NS are formed. Refinement is chosen such that each bin has at least 100 and at most 1000 NS, with a maximal refinement of  $\sim 150 \text{ pc}$  in both  $R$  and  $z$  (equivalent to 8 levels of refinement).

In each bin, we estimate  $\rho_{\text{DM}}$ ,  $\rho_{\text{tot},*}$ ,  $\sigma_{\text{rel}}$ ,  $\langle v_{\text{tar}} \rangle$  and the fractional number density of NS  $f_{\text{NS},i}$ . The latter is calculated as

$$f_{\text{NS},i} = \frac{N_{\text{NS},i}}{V_i N_{\text{NS,tot}}}, \quad (5.55)$$

where  $N_{\text{NS},i}$  is the number of star in bin  $i$ ,  $N_{\text{NS}}$  the total number of NS in the population synthesis ( $5 \times 10^6$ ), and  $V_i$  the volume of the bin with edges  $z_1 < z_2$ ,  $R_1 < R_2$

$$V_i = 2\pi(z_2 - z_1)(R_2^2 - R_1^2). \quad (5.56)$$

With these quantities, we can estimate the fractional settling rate density  $\gamma_{\text{set}}$  (settling rate per unit volume per target) in each bin for a given target as

$$\gamma_{\text{set,tar}} = \Gamma_{\text{cap}}(\rho_{\text{DM}}, \sigma_{\text{rel}}, \langle v_{\text{tar}} \rangle, m_{\text{PBH}}) p_{\text{set}} f_{\text{tar}}, \quad (5.57)$$

where  $f_{\text{tar}}$  is the fractional number density of the given target.

For WDs we take into account that we have two populations of stars: stars in the disc, and stars in the halo/bulge. For WDs in the halo we assume a spherical distribution of stars with the same dispersion as the DM, whereas for the WDs in the disc, we take  $\langle v_{\text{tar}} \rangle = v_c$  with a velocity dispersion of  $\sigma_u = 30 \text{ km s}^{-1}$ . The fractional number density of the halo/bulge WDs is given by  $f_b = (\rho_b + \rho_{h,*})/M_{\text{tot},*}$ , and for the disc  $f_d = \rho_d/M_{\text{tot},*}$ . We then calculate the fractional settling rate for the bulge/halo WDs and disc WDs separately, summing them together. Similarly, for both the settling in NSs and WDs, in  $p_{\text{set}}$  we take into account that the different stellar populations and therefore change eq. (4.64) to

$$\ln p_{\text{set}} = -\pi ([n_{*,b} + n_{*,h}] \sigma_v + 30 \text{ km s}^{-1} \times n_{*,d}) \frac{r_{\text{max},0}^2}{4} t_{\text{set}}, \quad (5.58)$$

where  $n_*$  is the number densities of stars of the given population, again assuming an average stellar mass of  $0.25 M_\odot$ .

In fig. 5.3 we show  $\gamma$  in each bin for a PBH mass of  $m_{\text{PBH}} = 10^{23} \text{ g}$ . We can see that the refinement is sufficient to distinguish the different regions, as  $\gamma_{\text{set}}$  for WDs is significantly reduced in the galactic centre, where stellar densities are high. The kick velocity for NS makes an obvious impact, as we see that the settling rate for NS is large multiple kpc above the disc, whereas for WD it is mostly confined in the disc and bulge.

We need to estimate the total number of NSs and WDs in the Galaxy. To do this we make some (significant) simplifying assumptions. The first assumption is that the star formation rate of the Galaxy is constant across cosmic time, and follows the density distribution of stars. The second assumption is that the initial mass function of stars is constant in time and space. With this we can estimate the fraction of stars within a given main sequence mass range via a Salpeter IMF (Salpeter 1955), defined as

$$\phi(m) dm = km^{-1.35}, \quad (5.59)$$

where  $k$  is a normalisation factor. Assuming that WD progenitors have MS masses below  $\leq 8 M_\odot$ , and that NS progenitors range between  $8 M_\odot - 20 M_\odot$ , we can estimate the total number of NS and WD by integrating eq. (5.59) over the respective mass ranges and time, assuming a star formation rate of  $3 M_\odot \text{ yr}^{-1}$ . Taking into account main sequence lifetimes (as the stars need to become stellar remnants), we estimate the total number of WDs and

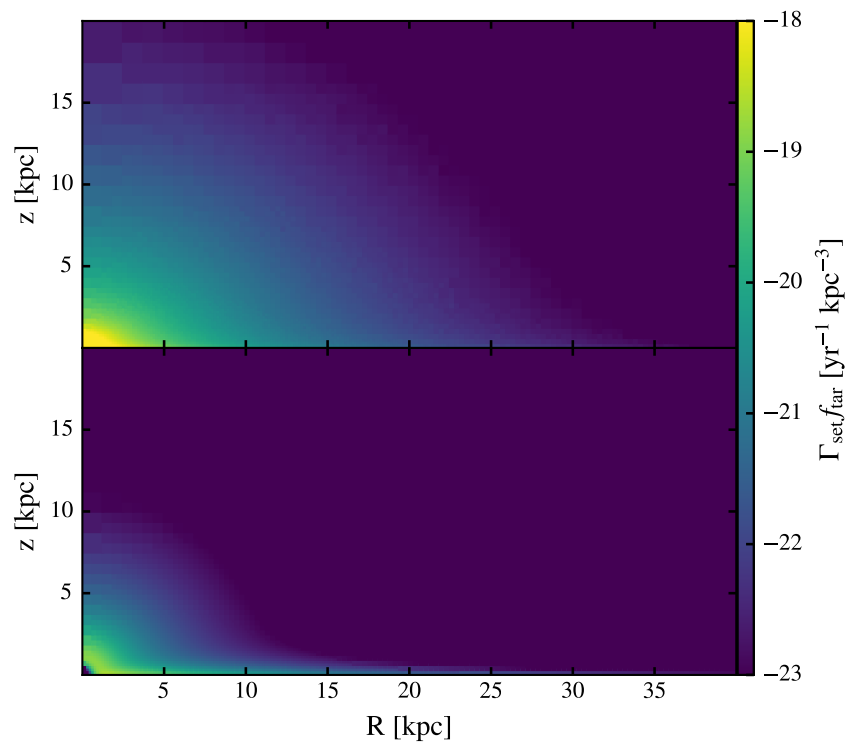


Figure 5.3: The fractional settling rate for the MWEG for NS (top) and WD (bottom), assuming a PBH mass of  $m_{\text{PBH}} = 10^{23} \text{ g}$ .

NSs currently in the Galaxy as

$$N_{\text{WD}} \sim 10^9 \quad (5.60)$$

$$N_{\text{NS}} \sim 10^8. \quad (5.61)$$

Of course this is a very rough estimate, as there are more realistic initial mass functions (eg. [Kroupa 2001](#); [Chabrier 2003](#)), and our approximation of mass ranges, star formation rate (and history) etc. is not detailed. However, as most of our models are either uncertain (eg. capture/settling), or approximate (eg. Galactic models), this order of magnitude estimate should be sufficient.

The total settling rate can now be estimated as the sum over all  $N$  bins:

$$\Gamma_{\text{set,tot,tar}} = N_{\text{tar}} \sum_{i=1}^N \gamma_{\text{set,tar},i} V_i. \quad (5.62)$$

For NSs we then find for  $m_{\text{PBH}} = 10^{23} \text{ g}$

$$\Gamma_{\text{set,tot,NS}} = 2.6 \times 10^{-10} \text{ yr}^{-1}, \quad (5.63)$$

and for WDs

$$\Gamma_{\text{set,tot,WD}} = 2.3 \times 10^{-13} \text{ yr}^{-1}. \quad (5.64)$$

These values are still not high enough for us to expect to observe a consumption event in the Milky Way. However, as we described in section [5.1](#), the luminosity of these events could be similar to gamma ray burst, and would therefore be seen as cosmological events.

### 5.3.2 Dwarf galaxies

For the dwarf galaxies, we use the same DM density and velocity dispersion as in section [3.2.3](#). However, to estimate the rate of transients, we need the number and distribution of stars. Unfortunately [Adams et al. \(2014\)](#) does not give an estimate of the total stellar mass of the dSpi, however estimates of the total stellar mass and its half-light radius is given for dSph and dIrr in [Read et al. \(2018\)](#). So for these estimate we chose only to look at dSph and dIrr. The average total stellar mass for the two types is taken as

$$M_{\text{tot,*}} = \begin{cases} 10^6 M_{\odot} & \text{dSph} \\ 10^7 M_{\odot} & \text{dIrr} \end{cases}, \quad (5.65)$$

and the half light radius  $R_{1/2}$  as

$$R_{1/2} = \begin{cases} 0.2 \text{ kpc} & \text{dSph} \\ 1 \text{ kpc} & \text{dIrr} \end{cases}. \quad (5.66)$$

We assume that the stars follows a spherical distribution, chosen as a Hernquist profile of eq. (5.48), with the parameter  $M_{\text{tot},*}$ , taken from eq. (5.65) and scale length  $a$ . Assuming a constant mass to light ratio, we can estimate  $a$  as

$$a = \frac{1.33}{1 + \sqrt{2}} R_{1/2}. \quad (5.67)$$

Furthermore, we assume that the initial mass function of stars is constant throughout the profile, again giving the fractional number density of a given target as

$$f_{\text{tar}} = \frac{\rho_*}{M_{\text{tot},*}}, \quad (5.68)$$

with each target having a number density of  $n_{\text{tar}} = N_{\text{tar}} f_{\text{tar}}$ , where  $N_t$  is again the total number of stars of that type.

As we have assumed a constant (temporally and spatially) initial mass function, the fraction of stars that are WD  $f_{\text{WD}}$  is also constant over  $r$ . However, as with the Galaxy, for NS we need to take into account that NSs receive a kick at birth. Instead of making a population synthesis, here we make a simplification by saying that all NS that receive a kick velocity  $v_{\text{kick}}$  such that their total velocity is larger than the escape velocity of the dwarf galaxy are ejected. The NSs that are not ejected are assumed to have the same distribution, which introduces errors within an order of magnitude, as shown in appendix B. Assuming that the NS progenitors are on circular orbits, the maximum kick velocity is taken as

$$v_{\text{kick,max}} = \sqrt{v_{\text{esc}}^2 - v_{\text{circ}}^2}, \quad (5.69)$$

where  $v_{\text{esc}}$  is the escape velocity, and  $v_{\text{circ}}$  the circular velocity. Taking the same Maxwellian kick distribution as in appendix B, the fraction of NS that remain bound is given as

$$f_{\text{bound}} = \left( \frac{1}{6\pi\sigma_{\text{kick}}^2} \right)^{1/2} \left[ \sqrt{6\pi} \sigma_{\text{kick}} \text{erf} \left( \sqrt{\frac{3}{2}} \frac{v_{\text{kick,max}}}{\sigma_{\text{kick}}} \right) - 6v_{\text{kick,max}} \exp \left( -\frac{3v_{\text{kick,max}}^2}{2\sigma_{\text{kick}}^2} \right) \right], \quad (5.70)$$

where  $\sigma_{\text{kick}} = 265 \text{ km s}^{-1}$  is the dispersion of the kicks, and erf the Error function. The fractional number density for NS is then given as

$$f_{\text{NS}} = \frac{\rho_*}{M_{\text{tot},*}} f_{\text{bound}} \quad (5.71)$$

We can now estimate the total settling rate as

$$\Gamma_{\text{set,tot,tar}} = 2\pi N_{\text{tar}} \int_0^r \Gamma_{\text{cap}}(1 - p_{\text{set}}) f_{\text{tar}} r^2 dr \quad (5.72)$$

which for a PBH mass of  $10^{23} \text{ g}$  gives for NSs

$$\Gamma_{\text{set,tot,NS}} = \begin{cases} 3.1 \times 10^{-10} \text{ yr}^{-1} & \text{dSph} \\ 4.3 \times 10^{-11} \text{ yr}^{-1} & \text{dIrr} \end{cases}, \quad (5.73)$$

and for WDs,

$$\Gamma_{\text{set,tot,WD}} = \begin{cases} 4.3 \times 10^{-8} \text{ yr}^{-1} & \text{dSph} \\ 4.8 \times 10^{-9} \text{ yr}^{-1} & \text{dIrr} \end{cases}. \quad (5.74)$$

Again, we see that the settling rates can be relevant in a cosmological framework. Assuming that our models for dSph and dIrr are somewhat representative of the settling rate in dwarf galaxies in general (eg. galaxy mass to settling rate holds), we can see that as the lower mass dSph dominate in settling rate, and as the mass function of galaxies follow a negative powerlaw for low stellar masses (see, eg. [Naab & Ostriker 2017](#); [Read et al. 2017](#)), the rates per dwarf galaxy should be closer to dSph. However, as a conservative estimate, we decide to use the average of the two rates when describing the total settling rate for dwarf galaxies

### 5.3.3 Cosmological transit rate

With the estimates the total settling rates for a MWEG and dwarf galaxies, we can estimate the transient rate per MWEG. For this we need the number of dwarf galaxies per MWEG. For Andromeda and the Milky Way, there are a few tens (eg. [McConnachie 2012](#)) of satellite dwarf galaxies. The number of dwarfs per MWEG can be even higher when considering different environments ([Read et al. 2017](#)), but as a conservative estimate we say that for each MWEG there are 10 dwarf galaxies. Comparing eqs. (5.63)-(5.64) and eqs. (5.63)-(5.64), we see that the settling rate for WDs is predominantly in dwarf galaxies, whereas for NSs the rates in the MWEG is dominant. Therefore the total settling rate per MWEG for WDs is (linearly) dependent on the number of dwarf galaxies per MWEG, whereas for NSs its approximately fixed for reasonable numbers of dwarf galaxies.

We can calculate the settling rate density by multiplying the settling rate per MWEG by the number density of MWEG. This density is typically estimated by taking the observed B-band luminosity density in the universe (tracer of active star formation), and, assuming that this luminosity is dominated by MWEGs, dividing it by the Milky Way B-band luminosity ([Phinney 1991](#); [Kalogera et al. 2001](#)). The density of MWEG from these estimates is roughly  $n_{\text{MWEG}} = 0.01 \text{ Mpc}^{-3}$ . We then get the total settling rate within a certain distance  $d$

$$\Gamma_{\text{set,tar}}(< d) = \frac{4\pi d^3}{3} \Gamma_{\text{set,tot,tar}} n_{\text{MWEG}}, \quad (5.75)$$

and we find that the distance required for a settling rate of  $1 \text{ yr}^{-1}$ ,  $d_1$ , is

$$d_1(m_{\text{PBH}} = 10^{23} \text{ g}) = \begin{cases} 382 \text{ Mpc} & \text{WD} \\ 2274 \text{ Mpc} & \text{NS} \end{cases}. \quad (5.76)$$

We need to be careful that these distances are not too large, such that the look-back time become significant. As the settling rate is linearly dependent on the number of WDs/NSs in each respective galaxy, there rates change during cosmic time. Not only do younger galaxies have less stars (due to less time forming stars), but since we are interested in stellar remnants, the ratio of WDs/NSs and main sequence stars is lower by the virtue of stars not having time to evolve through the main sequence and subsequent stellar phases.

With the cosmological rate derived above, we should be able to estimate the total number of events within a given year. However, as discussed in section 5.1, the specifics of these transient events are uncertain. While we have an upper limit on the final breakout luminosity, a significant fraction of this does not need to be in electromagnetic radiation. Furthermore, we do not know for how long these events would be luminous, and how the luminosity changes with time. Finally the direction of the luminosity is uncertain, as in the case of a high angular momentum star, only the poles would be accreted onto the BH, generating high luminosities.

In order to estimate how many of these transient events are observable, we need to know which conditions are required. To do this, we take two cases. In the first case, we assume that the transient events are similar to type 1a Supernovae (SNe), and in the other case that they have the same observational conditions as Gamma-Ray Bursts (GRB). By this we mean that the ratio of transient to observed transient is the same for PBHs consuming a given target as for either type 1a SNe, or GRB. We can then estimate the observational rate as

$$\Gamma_{\text{trans,obs}} = \Gamma_{\text{1aSNe/GRB,obs}} \frac{\Gamma_{\text{trans}}}{\Gamma_{\text{1aSNe/GRB}}}, \quad (5.77)$$

where  $\Gamma_{\text{trans/1aSNe/GRB}}$  is the rate of PBH consumption, type 1a SNe or GRBs, and the obs subscript denotes the observed rate. We approximate the rate per MWEG of type 1a SNe as  $\sim 10^{-2} \text{ yr}^{-1}$ , and take the GRB rate per MWEG as  $10^{-5} \text{ yr}^{-1}$  (Podsiadlowski et al. 2004) (giving a conservative estimate of eq. (5.77)). The observed rates for GRB with the Swift mission (Barthelmy et al. 2005) is on the order of  $100 \text{ yr}^{-1}$  (Gehrels & Mészáros 2012). For type 1a SNe the future LSST mission (LSST Science Collaboration et al. 2009) is expected to observe on the order of  $10^6 \text{ yr}^{-1}$ .

With the above estimates, we can determine the dark matter fraction that is made up by PBHs  $f_{\text{DM}}$  in order for the detection of 1 transient event in a given time frame  $\Delta t$ . This is given by

$$f_{\text{DM}} = \frac{1}{\Gamma_{\text{trans,obs}} \Delta t}. \quad (5.78)$$

This is shown in fig. 5.4 for the observation of WD consumption transient events, both assuming the same observational conditions as for type 1a SNe with the LSST, and for GRBs with Swift. The corresponding plots for NSs are not shown as they are either larger than 1 or minuscule as compared to that of the WDs. As we can see, once the probability of the PBH being scattered during settling limits us to mass ranges already constrained

by microlensing ([Niikura et al. 2019a](#)). If we would weaken that condition, the cut-off that is seen would be moved to lower masses, and therefore out of the constraints of the microlensing.

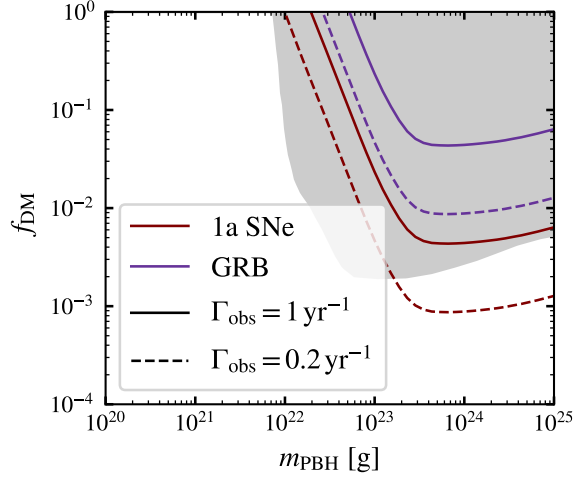


Figure 5.4: The fraction of DM  $f_{\text{DM}}$  required for an observational rate of a PBH consumption of a WD transit event of  $1 \text{ yr}^{-1}$  (full lines) and  $0.2 \text{ yr}^{-1}$  (dashed line), assuming that the transit event has similar observational conditions as type 1a SNe (red) observed with LSST ([LSST Science Collaboration et al. 2009](#)) or GRB (Purple) observed with Swift ([Barthelmy et al. 2005](#)). Current constraints from HSC microlensing of the Milky way halo and M31 ([Niikura et al. 2019a](#)) are indicated by the shaded region.

We note that the lines shown in fig. 5.4 are not constraints on PBH masses. Swift has been active for almost 5 years now, and one could derive the probability of not observing a WD consumption event in this time frame, and therefore constrain the PBH DM fraction. However, there are multiple aspects in this problem which are too uncertain, which is discussed in detail in section 6.3. So we leave these results as a possibility for further use in other studies.

# Chapter 6

## Discussion

In this chapter, we put our models for the capture/settling rates of PBHs into context. We start by comparing the derived capture rates in a MWEG, and in the GC, to that of similar research. We show that with differences/improvements in our models for the capture rate, our results are lower by a factor  $\sim 100$  than that of these previous works. We then describe how our improved modelling of the settling phase significantly changes the results of previous works by limiting the PBH mass range that can settle inside of targets. We expand on this with our treatment of binary targets, suggesting that previous results ignoring the binary-single interactions are inaccurate.

We then compare the model used for the energy dissipation in the single target capture to that of other works. Using their values, along with their arguments, we argue that adopting a different energy dissipation model would not change the energy loss significantly. We then demonstrate that the inclusion of density profiles should not significantly change our results, by comparing to other works including this aspect. Furthermore, we argue that including rotation of the target is most likely not relevant, as the target would have to rotate at close to break-up in order for the velocities to be comparable to that of the passing PBH. We then demonstrate that there could be another channel for PBHs to captured in targets by considering binary PBHs and the tidal force that they experience while passing close to a target.

Finally we show that the uncertainties in our derived observable transient rate can be significant. We discuss how our estimates based on comparing to Type 1a SNe and GRBs is faulty due to the major differences in the transient event of a PBH consuming a target. We note that as GRBs are observed at high redshifts, that our rates can be significantly reduced due to the increased lookback time. Also, we argue that as WDs can be disrupted during the initial passage of the PBH ([Graham et al. 2015](#)), our rates for high mass PBHs can be significantly reduced.

## 6.1 Comparison to previous work

In this section we start by comparing to other, related studies on how PBHs can be captured, settled and finally consume specifically NS. We start with a discussion specifically comparing the derived capture rates, and then move on to the major differences and between the rates derived in this work and other, eg. the treatment of the settling phase and binary systems.

### 6.1.1 Capture rates

As far as we know, no previous studies have attempted to demonstrate a cosmological transit rate. Therefore direct comparisons of those results is not possible. However as multiple of these studies have calculated Galactic capture/settling rates (eg. [Fuller et al. 2017](#); [Bramante et al. 2018](#)). These two studies find remarkably different results, with ([Bramante et al. 2018](#)) finding a maximum specific capture rate (capture rate for single NSs) of  $10^{-16} \text{ yr}^{-1}$  (given their total capture rate and assumed number of NSs), and [Fuller et al. \(2017\)](#) finding a specific galactic capture rate of  $10^{-11} \text{ yr}^{-1}$  for PBH masses of  $10^{19} \text{ g}$ . In our full galactic model, we obtain a specific capture rate of  $\sim 10^{-18} \text{ yr}^{-1}$  (see section 5.3.1), which is two orders of magnitude lower than that of ([Bramante et al. 2018](#))

[Bramante et al. \(2018\)](#) suggests that their more realistic treatment of the MWEG is the root cause of the massive difference between their results and that of [Fuller et al. \(2017\)](#), who represents the Galaxy using single values of the DM density and velocity dispersion closer to that of the GC ( $\rho_{\text{DM}} \sim 10^2 M_{\odot} \text{ pc}^{-3}$ ,  $\sigma_v \sim 100 \text{ km s}^{-1}$ ). We can also compare our estimate of the capture rate in the GC and the corresponding value used in [Fuller et al. \(2017\)](#), and see that given that our fiducial DM density is larger by  $\sim 10^2$ , that our specific capture rates agree with that of [Fuller et al. \(2017\)](#) in the GC. As our galactic rates are much lower than in the GC (see section 5.3.1) we then agree with [Bramante et al. \(2018\)](#) that a more accurate model of the Galaxy is required.

As to the difference between our results and that of [Bramante et al. \(2018\)](#), we find two differences in methodology. First, we note that the galactic model used by [Bramante et al. \(2018\)](#) places all of the NSs in the galactic midplane. This accounts for some of the difference between the capture rates derived here and that of [Bramante et al. \(2018\)](#), as rerunning the calculations with all of the NSs located in the midplane increases our capture rates somewhat, but they are still a order of magnitude lower than in [Bramante et al. \(2018\)](#). The second difference is that we take into account the velocities of the NS population, whereas [Bramante et al. \(2018\)](#) takes the NSs as stationary. As we show in chapter 3, taking into account the velocities of the target always push the relative velocity distribution to higher values. Therefore the number of PBHs that become captured is significantly lower, due to the higher initial energies. Redoing the calculations for stationary NSs (no velocity dispersion and mean velocity), retains capture rates slightly lower than that of [Bramante et al. \(2018\)](#), with the remaining difference being accounted for by the spatial distribution of NSs.

### 6.1.2 Disruption during settling & binaries

As discussed previously, the possibility for the PBH to be disturbed while its in the process of settling has not been considered or neglected in most similar studies. As shown in fig. 5.2 and eq. (4.65), the scattering probability can significantly limit the mass range that studies of this type can constrain. The constraint from Capela et al. (2013) is already in contention, due to uncertain DM densities in globular clusters (their target environment). Due to them not taking into account that the PBH can be scattered during settling, their constraint is further weakened. As globular clusters are the densest stellar environments, with the possible exception of galactic nuclei, the probability of being ejected is high. By eq. (4.65) the minimum mass that can settle in NSs becomes  $10^{22}$  g for number densities of star of  $\sim 10^5$  pc $^{-3}$ . As globular cluster densities can be close to this value, we therefore expect that the minimum mass that Capela et al. (2013) can constrain is at most slightly lower than that already constrained by microlensing.

The same conclusion hold for the other studies of capture in NSs. This is specifically noticeable in figure 2 of Fuller et al. (2017) and figure 1 in Takhistov (2018). These studies do not specifically put constraints on PBH masses, but rather determines the rates, and resulting consequences of the consumption of NS by PBHs. Fuller et al. (2017) demonstrates that the formation of r-process elements in the ejecta of the consumption events in millisecond pulsars, and shows in that this can account for the entire Galactic abundance of these elements for PBH DM fractions on the order of  $\sim 1\%$ . Takhistov (2018) that estimates that  $f_{\text{DM}} 10^{-3}$  is enough for there to be one merger event of a transmuted binary per year in aLIGO/VIRGO. As can be seen in their aforementioned figures, both of these studies show that their respective results holds for PBH masses  $\leq 10^{20}$  g, which, based of eq. (4.65) is not possible due to the scattering of the PBH during settling.

The estimate from Takhistov (2018) also relies on the PBH being captured inside of a tight binary. However, Takhistov (2018), and similar studies on capturing in binaries (Bramante et al. 2018; Abramowicz et al. 2018), neglected the dynamics of the binary, and only included the energy dissipation model. As we showed in section 4.6, the three body interaction between a PBH and a tight NS-NS binary leads to changes in energy orders of magnitude larger than the energy dissipation. This means that their capture rates are not accurate for binary systems. We have shown that capturing in binaries is rare, and not described by energy dissipation as in the single target case. We therefore argue that their results are invalid.

## 6.2 Energy dissipation and capture processes

In this section we discuss the models used for capturing PBHs inside of targets. As described in section 4.1.1, for single targets we adopt a model based on dynamical friction from scattering particles inside of the target, which are assumed to be free. We are going to discuss and compare other models for the energy loss, some of which are also based on dynamical friction (Abramowicz et al. 2009, 2018), whereas some use more advanced

models [Pani & Loeb \(2014\)](#); [Defillon et al. \(2014\)](#). We then move on to describe other possible capturing mechanism, specifically involving PBH binaries.

### 6.2.1 Energy dissipation models

Before describing different dissipation models, and see how they compare to the one adopted here, we should start by noting how the capture/settling rates change when the dissipated energy increases/decreases. If the energy loss is larger than modelled here then two aspects are changed. First, as the energy loss is higher, more energetic PBHs get captured, and therefore a larger fraction PBHs that collide with the target become bound. Secondly, with the higher energy loss, the orbits during the settling phase are shorter, and the settling time become shorter, making it less probable that an intruding star can scatter away the PBH. For lower energy losses the reverse situation applies, with less PBHs becoming bound, and higher mass PBHs becoming susceptible to scattering during the settling phase.

With that in mind, lets start by considering the other energy model based on dynamical friction used in [Abramowicz et al. \(2009, 2018\)](#). Unlike the model used in this thesis and other works ([Capela et al. 2013](#); [Fuller et al. 2017](#); [Takhistov 2018](#)), that considers conservation of momentum in the scattering of individual particles, this model considers the gravitational force by the wake caused by the PBH travelling through the medium. In [Abramowicz et al. \(2009\)](#) the energy losses cited are similar to the ones derived in this work. However in [Abramowicz et al. \(2018\)](#) the energy loss for a PBH passing through a NS is higher than the one adopted here by a factor of  $\sim 10$ , which would then increase the results shown here. However it is important to note that the energy loss in these works do not take into account relativistic effects, nor do they take into account that the medium of NS is in a degenerate state. It is also unclear why the results between [Abramowicz et al. \(2009\)](#) and [Abramowicz et al. \(2018\)](#) differ.

Energy losses for NSs derived in the work of [Pani & Loeb \(2014\)](#) were higher than that derived here by roughly  $\sqrt{R_{\text{NS}}/R_s}$ , where  $R_s$  is the Schwarzschild radius of the PBH. This is multiple orders of magnitude and would significantly change the results given here. The energy dissipation in this model is not based on dynamical friction, but is rather based on tidal heating and the excitation of non-radial acoustic modes in the NS. The total energy loss then becomes a sum over all modes. However, it has been argued that due to the PBH travelling at supersonic velocity, the higher order modes are not excited, and the energy loss is reduced to a value similar to that from dynamical friction ([Capela et al. 2014](#); [Defillon et al. 2014](#)). [Pani & Loeb \(2014\)](#) argue that this is not the case, as it would imply that high order modes are never excited during close parabolic orbits of any object (specific citing another NS). However, the analytical calculations in [Defillon et al. \(2014\)](#) supports the case for causality limiting the excitation of high order modes.

It is interesting to consider that if higher modes are not limited, then the energy loss is high enough that it could be relevant in the case a PBH travelling through a NS-NS binary. If the energy loss is high enough for a PBH travelling through one of the NS becomes high enough, then the PBH may never go far enough away from the NS in order to be scattered away by its companion. In that case, there might still exist a non-negible rate of NS merger

with a NS mass BH, giving distinct gravitational wave signals. However, as stated above, the energy dissipation is most likely not high enough for this to be the case.

In light of the arguments from [Defillon et al. \(2014\)](#), we can say that the energy dissipation derived here is consistent within an order of magnitude between all models. This is not to say that there are no flaws to this model, and the inclusion of further physics may change the energy dissipation (discussed in the next part of this section). However, based on the convergence between different models, at the time of writing, we cannot find a reason why a more realistic energy dissipation would significantly change our results.

### 6.2.2 Properties of the target

There are multiple aspects to the energy dissipation model which we have ignored in this work. Specifically, we have not included the possibility of the target to rotate, nor have we considered different (more realistic) density profiles. Now we address what could change if these aspects were included in our model.

#### Density profiles

Our models did not include realistic density profiles, instead making simplifications by assuming that the targets had a uniform density. This could impact the energy dissipation, as the density goes linearly into [4.22](#), and most PBHs have their trajectory off-centre, and therefore encounter lower densities, affecting the average energy loss. For NSs we can compare to [Capela et al. \(2013\)](#), who included a density profile from ([Belvedere et al. 2012](#)). As mentioned, our average energy loss is larger than that of [Capela et al. \(2013\)](#) by roughly 8%. However, we do not know if this is due them including a density profile, as we take into account the trajectories of the PBHs in a relativistic framework, which could account for the increase.

A steep density profile would not only affect the encountered density of the PBHs, but would also affect the velocities, as further acceleration is possible. The density profile then have a non-linear influence on the energy loss. Based on that the energy loss scales as  $v^{-2}\rho$  (see section [4.1.1](#)), we see that as the lower velocities corresponds to the exterior region of the target, the energy loss is reduced with the inclusion of a density profile, however the details of this reduction depends on the steepness of the density profile. The volume of NSs are dominated by the core which only varies by an order of magnitude ([Belvedere et al. 2012](#)). For WDs and specifically MSs the variation in the density can be higher. MSs contain cores and are therefore centrally concentrated, and therefore the energy loss could be significantly reduced from what is given in this thesis.

However, as the energy loss for MSs was already low, we only considered NSs and WDs. As both of these mainly consists of the core, we do not expect them to have a steep density profile. Therefore, the energy loss cited in this thesis should not change significantly with the introduction of a density profile, and our results should stay the same within an order of magnitude.

## Rotation

Another property of the target which was ignored is the rotation of the target. If the target is rotating then that would affect at which velocities the PBH encounters the medium, depending on the orientation of the PBH. While on average the encountered velocity is the same, we can see from fig. 4.2 that the energy loss is non-linear with the velocity. However, the PBH always travel close to the escape velocity of the target, and therefore the relative velocity between the PBH and the medium is dominated by the velocity of the PBH, unless the target is rotating close to breakup. The rotation of the target is then only relevant for millisecond pulsars.

In practice millisecond pulsars have periods of  $\sim 10 - 100$  ms, which, assuming solid body rotation grants maximum rotational velocities of  $\sim 10^{-2} - 10^{-3}c$ , which is small compared to the escape velocity  $\sim 0.5c$ . However there are some recorded pulsars with periods of  $\sim 1.4$  ms (eg. [Hessels et al. 2006](#)), which corresponds to a rotational velocity of  $\sim 0.1c$ . As the energy dissipation for NSs is in the plateau of fig. 4.2, an increase in relative velocity could result in an overall increase in energy dissipation. However as this is only relevant for the outskirts of the NS (fastest rotational velocity), and single NSs this rapidly rotating are observationally rare, we do not expect rotation to affect our results.

### 6.2.3 A third capture channel: PBH binaries

In the formation of PBHs and their subsequent dynamical evolution through time, some fraction of them may end up in PBH-PBH binaries ([Nakamura et al. 1997](#); [Ali-Haïmoud et al. 2017](#); [Sasaki et al. 2018](#)). This probably does not change the current capture rates via the two capture channels considered in this work. However, the possibility of two small PBHs being in a binary interacting with a (much more massive) target, such as NSs/WDs or MSs introduces another capture channel.

We note that the mass ratio between a PBH and a star is on the order of  $10^{-10} - 10^{-16}$ . This is similar or smaller than the mass ratio between SMBHs and stars. This means that we can relate the situation of a PBH binary encountering a NS to that of a stellar binary encountering a SMBH. It is well understood that the tidal force that a SMBH exerts on a stellar binary can disrupt the binary, with one of the binary stars giving energy to the other. The result is that one of the stars can be ejected, which is a possible explanation for hyper velocity stars (eg. [Hills 1988](#); for review, see [Brown 2015](#)). However, for our purposes, the interesting aspect of this situation is the companion that loses energy, as this one becomes bound to SMBH, and can possibly fall into it. Translating to a PBH-PBH binary encountering a NS, we see that there is a possibility for one of the PBHs to become bound to the NS. If the disruption of the PBH binary occurs within the radius of the NS, the bound PBH have its trajectory through the NS, and settles via energy dissipation as described in section 4.4. If the disruption occurs outside of the NS, this is still a possibility, given that the energy loss is high enough.

As this is outside of the scope of this project, we do not go into detail, but we can determine the viability of this capture channel. Consider a binary of total mass  $m_b =$

$2m_{\text{PBH}}$  and semi-major axis  $a$  on a trajectory with a pericentre passage  $r_{\text{peri}}$  around a NS. The probability of this binary to disrupt is [Hills \(1988\)](#)

$$p = 1 - D/175 \quad (6.1)$$

$$D = \frac{r_{\text{peri}}}{a} \left( \frac{10^6 m_b}{2M_{\text{NS}}} \right), \quad (6.2)$$

where  $p = 0$  for  $D > 175$ . The distribution of the semi-major axis of a PBH-PBH binary is dependent on the conditions in which PBHs are formed, the PBH masses, and their ability to not be disrupted over the lifetime of the universe ([Ali-Haïmoud et al. 2017](#)). However, as the probability of eq. (6.1) is lower for small  $a$ , we can estimate  $a$  by the minimum semi-major axis that do not merge within a Hubble time ( $\sim 10$  Gyr),  $a_{\text{min}}$ . Via Peters equations ([Peters 1964](#)), assuming a circular binary, this can be estimated as

$$a_{\text{min}} = (4\beta \times 10 \text{ Gyr})^{1/4}, \quad (6.3)$$

$$\beta = \frac{128G^3 m_{\text{PBH}}^3}{5c^5}. \quad (6.4)$$

Inserting  $a_{\text{min}}$  into eq. (6.1), with  $r_{\text{pero}} = R_{\text{NS}}$ , we see that the probability is greater than 0 for PBH masses larger than  $10^{20}$  g.

The above estimate shows that binary PBHs interacting with a target could be a viable capture channel. However, to estimate rates (capture/settling/tranients) we would need more detailed calculations on the binary fraction of PBHs along with their distribution in  $a$ . While this is a feasible calculation (again, see [Ali-Haïmoud et al. 2017](#)), it remains outside the scope of this thesis, and is left as a possibility for future work. We do however note that the resulting capture rate would not depend on  $m_{\text{PBH}}$  in the same way as the one based on energy dissipation, and could therefore lead to interesting results.

## 6.3 Viability of the observational transient rates

As mentioned previously, the observational rate of PBH consumption events derived in section 5.3.3 contain multiple uncertainties, making further use unviable. These extend beyond the inherent (unquantified) uncertainty of the models for the capture processes. In this section we discuss these uncertainties.

### 6.3.1 Transients of PBH consumption events

As we discussed in section 5.1, the final stages in the consumption of a NS or WD by a PBH is not well determined. We worked around this uncertainty by assuming that the resulting transients were either similar to GRBs or Type 1a SNe. There is obviously a possibility that consumption events could behave differently from these events, however let's first assume that this is not the case. Then one would have to consider if the consumption events would be distinguishable from Type I SNe (and/or GRBs). In the case of the

consumption of WDs, from which the highest observational rates are obtained, this is very much an open question.

We already mentioned in section 5.1 that during the growth phase of a BH inside of a WD, the conditions might be met such that a runaway nuclear reaction occurs. If this happens, the consumption event would behave almost, if not exactly identical to a Type 1a SNe. In that case, it is likely that there would be no distinguishing observational signal between these events. Furthermore, the rates per MWEG for consumption events ( $\sim 10^{-7} \text{ yr}^{-1}$ ) and Type 1a SNe ( $\sim 10^{-2} \text{ yr}^{-1}$ ) differ by orders of magnitude. Therefore, the slightly increased rate due to the extra progenitor channel of Type 1a SNe would in most cases not be measurable within a reasonable degree of uncertainty.

If the consumption events differ from Type 1a SNe, but are similar to SNe in general, then there is a possibility that one could distinguish them based of light curves and luminosity. The maximum breakout luminosity ( $\sim 10^{18} L_\odot$  for the consumption of a WD) is orders of magnitude higher than that of typical SNe. The actual breakout luminosity could be orders of magnitude lower (due to lower densities) and may not be completely in electromagnetic radiation, as some energy may be emitted in neutrinos or gravitational radiation. Therefore the luminosities could be comparable. However, as we do not know how much, if any, material is ejected, and for how long the ejected material is luminous, it might not be reasonable to suggest that these events would have the same observational conditions.

The assumption that WD consumption events are similar to GRBs is not fully viable, as the maximal breakout luminosity for WDs containing a BH estimated in this work is on the low end of the expected luminosities for GRBs (Tsutsui et al. 2013). Given that the estimated breakout luminosity is a maximum, the consumption event of a WD and a GRB might differ in luminosity by orders of magnitudes. Furthermore, the assumption that these events are similar relies on that the matter of the WD has high enough angular momentum in order to form a disc, limiting the angle at which the radiation is emitted. As it is uncertain if an accretion disc is formed, once again the observational conditions may differ between consumption events and GRBs.

The arguments listed above shows that in order for the observational rates derived in this work to actually constrain the DM abundance of PBHs, we need a detailed model of the growth phase and consumption event of WDs/NSs. Not only is a more accurate luminosity estimate required for a proper analysis, but this could possibly also give insight into what wavelengths the radiation is emitted (something we have neglected entirely) and how much mass is ejected and if this can stay luminous. With some simple arguments, Fuller et al. (2017) indicated that with outward transport of angular momentum, upwards of  $\sim 0.5 M_\odot$  could be ejected in the consumption of a millisecond pulsar. However, for regular pulsars (and NSs in general), along with WDs, this may not be the case.

A more detailed model on how a consumption event could be observed is needed for a detailed analysis of the cosmological/observational rates derived in this work. However, as this is outside of the scope of this project, we leave this for future studies. We note that the two comparisons chosen (Type 1a SNe and GRBs) do cover two ends of the possibility space of the observational signatures of consumption events. Type 1a SNe comes into the

low luminosity range, but with roughly spherical emission, with a long timescale for the luminosity, whereas GRBs covers the high luminosity range, but the luminosity is directed. As these two estimates recovers similar observational rates, within two orders of magnitude, the actual observational rate could be within, or close to, this range.

### 6.3.2 Lookback time

As both the observations of Type 1a SNe, and specifically GRBs considered here are cosmological, there is a possibility that the region of space needed to be probed in order for one observation of a WD/NS consumption event in a given timeframe reaches to large redshifts. As mentioned, this could change the transient event rate, due to the longer lookback time. This is specifically important for WDs, as the more numerous low mass main sequence progenitors have longer lifetimes. Therefore the number of WDs that can be consumed (and by extention transient rates) would drop rapidly with lookback time, as the low mass progenitors have not left their main sequence.

For the comparison with Type 1a SNe, this should not have a massive influence on the results. The average redshift of Type 1a SNe observed within the main field of the LSST will be  $\sim 0.5$  ([LSST Science Collaboration et al. 2009](#)), which while it is considered a fairly large redshift, the lookback time on the order of  $\sim$  Gyr, meaning that the age of the galaxies are still  $\sim 10$  Gyr. Also, the progenitors of Type 1a SNe are thought to be WDs, which could imply that the two rates scales similarly with redshift. However, as the Type 1a progenitors are most likely binaries, the main sequence is affected by binary evolution, which would make this comparison unfair (considering that capturing and settling in binaries is difficult).

In the comparison with GRBs on the other hand, lookback time should be taken into account. The average redshift observed for GRBs with Swift is  $\sim 2.8$  ([Jakobsson et al. 2006](#)), at which the universe is young ( $\sim$  Gyr). Therefore the number of WDs can be significantly lower, reducing the settling, and therefore transient rate.

### 6.3.3 Viable mass range of PBH

We showed that only the consumption events of WDs had transient rates high enough to reliably observe the events within a reasonable time frame. However, this was only true for PBH masses of  $\gtrsim 10^{22}$  g. As mentioned, this mass range is already constrained by microlensing, but judging by fig. 5.4, if observed for long enough, one could derive stronger constraints on the mass range above  $10^{23}$  g than current microlensing constraints. This mass range does, however, suffer from another problem.

As discussed in section 2.2.6, energy dissipation that a PBH experiences while it is passing through a WD increases the temperature of the medium. [Graham et al. \(2015\)](#) showed that the increase in temperature can be high enough, in order for runaway nuclear fusion to occur, resulting in the disruption of the WD in a Type 1a SNe. If this is the case, then the capture and settling of the PBH never occurs, and the resulting transient cannot be distinguished from a Type 1a. Furthermore this could significantly limit the

capture/settling rates derived in this work, as the WD is disrupted and therefore the settling phases do not occur.

The energy dissipation scales as  $m_{\text{PBH}}^2$  (see section 4.1.1), and therefore higher PBH masses increases the probability of the WD disrupting. Figure 1. in [Graham et al. \(2015\)](#) shows that the minimum  $m_{\text{PBH}}$  required to disrupt a WD of a given mass scales log-linearly, such that higher PBH masses, less massive WDs can be disrupted. For a PBH mass of  $10^{23}$  g, WDs with masses larger than  $\sim 0.6 M_{\odot}$  get disrupted. Considering that the observed mass distribution peaks at  $0.6 M_{\odot}$  and drops off rapidly at either side of the peak ([Liebert et al. 2005](#)), this implies that for PBH masses of  $10^{24}$  g or higher, a significant fraction of WDs are disrupted before the PBH can settle. This would reduce the number of WDs that are candidates for being consumed by a PBH, and therefore lower the settling/transient rates for high PBH masses.

For  $10^{23}$  g BHs, including the possibility of the WDs being disrupted during the passage would reduce the settling/transient rates by a factor of  $\sim 0.5$ . Considering the log-scale of fig. 5.4, this does not change our results significantly. However, for more massive PBHs, the fraction would go towards zero, and the decrease seen at the high mass range in fig. 5.4 would be steeper.

# Chapter 7

## Summary & conclusions

In this chapter we summarise the work done in this thesis. We start by briefly explaining the key models used and our key results. After this we list our main conclusions, the caveats attached to them, and how they relate to previous, similar works.

### 7.1 Summary

#### Collisions, Capture and Settling

In this thesis we have considered the collisions, capture and settling of low mass primordial black holes inside of various targets such as neutron stars, white dwarfs and main-sequence stars. We specifically concern ourselves with asteroid mass ( $10^{16} - 10^{17}$  g) and sub-lunar ( $10^{20} - 10^{22}$  g) primordial black holes, the abundance of which is still relatively unconstrained, and could make up a significant amount of the dark matter content of the universe. The settling of one of these black holes would lead to the disruption of the target star, and we have used this fact in order to attempt to derive theoretical observational rates of the resulting transients, and possible constraints on the two mass ranges.

Assuming that all dark matter consists of primordial black holes of a given mass, in chapter 3 we have used simple models of various environments such as the galactic centre, solar neighbourhood and the entire Galaxy, along with dwarf galaxies, to estimate the collision rate between primordial black holes and a given target. The collision rate depends on the number density of the primordial black holes (see eq. 3.12), and therefore the collision rate is inversely proportional to the mass of the black holes. Due to the low masses in consideration, we find that the collision rates can be high, depending on target and environment. However, as the black holes are small, in most cases, a collision simply implies that the PBH passes through the target. Therefore a collision does not imply the capture of a primordial black hole.

In chapter 4, we have considered two possible channels for a primordial black hole to be captured by a target during a collision or interaction, the first involving the capture of a black hole by a single target, discussed in sections 4.1 and 4.2. By considering the drag force the primordial black hole experiences from its interaction with the medium of the target,

we have determined the energy loss of a black hole as it passes through a target. We did this by re-deriving the dynamical friction force from [Capela et al. \(2013\)](#), taking into account general relativistic effects. We then integrated this force over the trajectory through the target, which was numerically solved in a general relativistic framework. We found that the average energy loss is low, which implies that the initial relative velocity between the black hole and the target has to be small in order for capture to occur. Furthermore as the energy loss is proportional to the square of the black hole mass, low mass black holes are less likely to capture.

As the energy loss is small, a captured black hole ends up on a long elliptical orbit, going through the target. Subsequent passages through the target results in further energy loss, causing the primordial black hole to spiral inwards in what we denote as the settling phase. Again, following [Capela et al. \(2013\)](#), in section 4.4 we investigated this phase using simple arguments on the orbit, determining how long time it takes for the primordial black hole to settle. Furthermore, unlike previous works, we take into account that as the orbit of the black hole is large, there is a non-zero probability of the primordial black hole to be scattered by an intruding star. As the energy loss is lower for low mass black holes, below a certain mass (dependent on the environment) the probability of being scattered is practically 100%, and therefore low mass primordial black holes do not settle inside of targets.

The second capture channel that we consider involves the three body interaction between a primordial black hole and a stellar binary. Considering the primordial black holes as test particles, we developed a code to numerically integrating their trajectories through the binary, investigating the exchange of energy between the binary and the black hole. We found that in most cases the black hole gains energy and is therefore ejected from the binary. The black holes that become bound end up on long orbits, and once they return to the binary, they are in many cases ejected. While we did find that some PBHs were still bound to the binary at the end of our simulations, these were not captured inside of one of the stars, and we argue they would be disrupted at a later stage. We found that the energy exchanged is much greater than that for the dynamical friction described above, and therefore argue that capturing black holes in binaries is difficult.

The relation between the number of primordial black holes that collide, become captured and settle inside of targets is summarised in fig. 7.1. The number of primordial black holes that undergo a collision is high, specifically for low mass black holes. However, due to the energy loss being low, and capturing in binaries being improbable, the number of black holes that captures is lower, specifically for low mass black hole where the energy loss is smaller. Furthermore, as the black holes that get captured end up on long orbits, black holes below a given mass have a large probability of being scattered away by an intruding star and never settles inside the target. This becomes relevant for constraining sub-lunar mass PBHs, as depending on the target and environment in consideration, the minimum mass that can settle inside of stars can be large, and outside of the sub-lunar mass range.

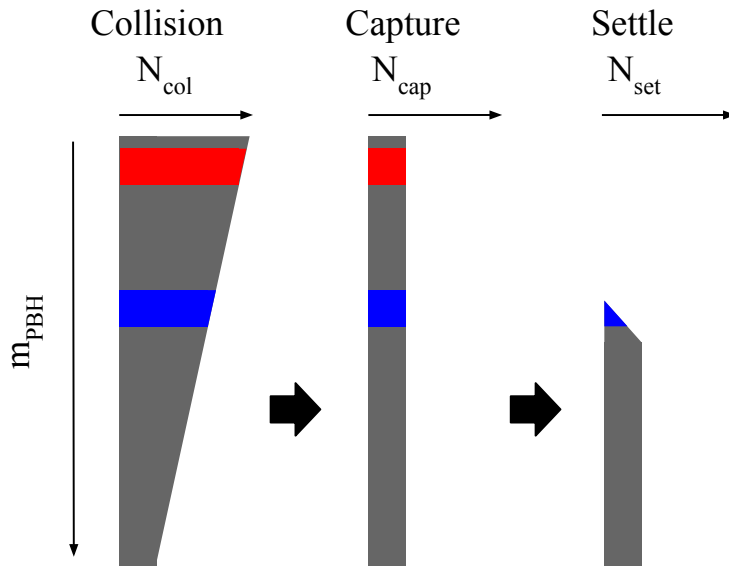


Figure 7.1: Schematic on how many primordial black holes collides, then captures and finally settles inside of a given target, depending in the mass of the primordial black hole  $m_{\text{PBH}}$ . The red regions indicate the asteroid mass PBH range, and the blue regions roughly correspond to the sub-lunar mass range (dependent on environment and target).

### Observational rate

In chapter 5, we discuss what the possible outcomes are if a primordial black hole settles inside of a given target, and what the possible transient event would be. After this, in section 5.3 we estimate the total settling rate in both a milky way equivalent galaxy, and in dwarf galaxies. Assuming that the transient events are similar to either gamma-ray bursts or type 1a supernovae, we estimate the relative rate between these events and the transient events originating from primordial black holes. With this we are able to estimate the observational rate of the black hole induced transient event, which are shown in fig. 5.4. We show that due to the probability of the primordial black hole being scattered during the settling phase, the observation rate is insignificant for black hole masses not already constrained via microlensing ([Niikura et al. 2019a](#)).

## 7.2 Conclusions

Following the discussion above, the main conclusions of this thesis are:

- The collision rate between primordial black holes and targets such as stars and stellar remnants is high, but due to inefficient energy loss, the capture rate is low.
- Capturing in binaries is improbable, as the primordial black holes on average extracts energy from the binary, becoming more unbound. This invalidates previous results

## *CHAPTER 7. SUMMARY & CONCLUSIONS*

---

that treats binaries as two individual targets, with the primordial black holes being captured via energy dissipation in the same way as for single targets (eg. [Fuller et al. 2017](#); [Bramante et al. 2018](#); [Takhistov 2018](#)).

- Primordial black holes that are in the process of settling inside of a target are on large enough orbits, that for low mass primordial black holes the probability of being ejected is significant. This makes the settling of low mass black holes practically impossible, significantly limiting the results in this thesis and other works that have not accounted for this effect.
- Due to the high luminosity in the consumption of a star by a black hole, there is a possibility that the consumption events of white dwarfs could be observable with relevant rates. However due to the probability of the PBHs being scattered during settling, the observational rates are too small for primordial black hole masses not already constrained by microlensing.

Our results do not give rise to new constraints on the possible dark matter fraction of primordial black holes. They do however show that the proper treatment of both capturing in binaries, and the settling of a primordial black hole inside of a single target is required in the development of future constraints based on the same process.

# Appendix A

## General relativistic calculations

### A.1 Schwarzschild metric

Many parts of this thesis considers the motion of massive particles in the Schwarzschild metric ([Schwarzschild 1916](#)), defined by eq. (4.2) or

$$g_{\alpha\beta} = \begin{pmatrix} -(1 - R_s/r) & 0 & 0 & 0 \\ 0 & (1 - R_s/r)^{-1} & 0 & 0 \\ 0 & 0 & r^2 \sin^2 \theta & 0 \\ 0 & 0 & 0 & r^2 \end{pmatrix}, \quad (\text{A.1})$$

where  $g_{\alpha\beta}$  is the metric tensor and  $R_s = 2GM/c^2$  is the Schwarzschild radius of the central object with mass  $M$ . This section covers many of the calculations essential for the work done in this thesis. The rest of this appendix adopts geometric units ( $G = c = 1$ ).

The most important relation for our purposes is how the  $r$  of an orbiting particle changes with the proper time  $\tau$ . This can be derived by using the fact that the metric is both time independent and spherically symmetric, meaning that angular momentum and energy is conserved. This then gives the 4-momentum  $p^\mu$  as

$$\frac{1}{m} p^t = \frac{dt}{d\tau} = (1 - R_s/r)^{-1} \tilde{E} \quad (\text{A.2})$$

$$\frac{1}{m} p^\phi = \frac{d\phi}{d\tau} = \frac{1}{r^2} \tilde{L} \quad (\text{A.3})$$

$$\frac{1}{m} p^r = \frac{dr}{d\tau}, \quad (\text{A.4})$$

where  $\tilde{E} = p_t$  and  $\tilde{L} = p_\phi$  is the specific energy and angular momentum of the particle of mass  $m$ , and we have chosen the orbital plane such that  $\theta = \pi/2$ . Using that  $p^\mu p_\mu = m^2$  one can then derive that ([Schutz 2009](#))

$$\left( \frac{dr}{d\tau} \right)^2 = \tilde{E}^2 - \left( 1 + \frac{R_s}{r} \right) \left( 1 + \frac{\tilde{L}^2}{r^2} \right). \quad (\text{A.5})$$

This equation is used in the remainder of this section in order to derive both the cross section of a body, and the trajectories of particles around a body.

### A.1.1 Cross section

If one takes an object (such as a star) as spherically symmetric and static (eg. no rotation), then the metric outside of the object is given by the Schwarzschild. As such, the cross section of a target for a given  $\tilde{E}$  is set by the  $\tilde{L}$  which satisfies that the minimum of  $r$  is at the radius of the target  $R_{\text{tar}}$ . From eq. (A.5) we then get

$$\left(\frac{dr}{d\tau}\right)^2 \Big|_{r=R_{\text{tar}}} = E^2 - \left(1 - \frac{R_s}{R_{\text{tar}}}\right) \left(1 + \frac{L^2}{R_{\text{tar}}^2}\right) = 0, \quad (\text{A.6})$$

which solved for  $\tilde{L}$  gives

$$L^2 = \left(\frac{E^2 - 1 + R_s/R_{\text{tar}}}{1 - R_s/R_{\text{tar}}}\right) R_{\text{tar}}^2. \quad (\text{A.7})$$

For an unbound particle, conservation of angular momentum and energy means that  $\tilde{E}$  and  $\tilde{L}$  can be described by their values at infinity (eg. in Minkowski space)

$$\tilde{E} = \gamma \quad (\text{A.8})$$

$$\tilde{L} = bv\gamma, \quad (\text{A.9})$$

where  $b$  is the impact parameter,  $v$  the velocity at infinity and  $\gamma = (1 - v^2)^{-1}$ . This then gives

$$\gamma^2 v^2 b^2 = \left(\frac{\gamma^2 v^2 + R_s/R_{\text{tar}}}{1 - R_s/R_{\text{tar}}}\right) R_{\text{tar}}^2, \quad (\text{A.10})$$

or the corresponding cross section  $\sigma = \pi b^2$

$$\sigma = \pi \left(\frac{1 + \frac{R_s}{\gamma^2 v^2 R_{\text{tar}}}}{1 + R_s/R_{\text{tar}}}\right) R_{\text{tar}}^2. \quad (\text{A.11})$$

Furthermore, as a check, we can see that in the non-relativistic limit ( $R_s/R_{\text{tar}} \rightarrow 0, \gamma \rightarrow 1$ ), eq. (A.11) goes to its Newtonian solution

$$\sigma = \pi \left(1 + \frac{2GM_{\text{tar}}}{R_{\text{tar}}v^2}\right) R_{\text{tar}}^2. \quad (\text{A.12})$$

### A.1.2 Trajectories

In this subsection, we describe how one calculates trajectories in the Schwarzschild metric. The derivation of this can be seen in detail in [Chandrasekhar \(1983\)](#), but is summarised here for use in sections [4.1.1](#) and [4.2](#). Starting by dividing eq. [\(A.5\)](#) by the square of eq. [\(A.3\)](#):

$$\left(\frac{dr}{d\phi}\right)^2 = R_s r - r^2 + \frac{R_s}{\tilde{L}^2} r^3 + \frac{\tilde{E} - 1}{\tilde{L}^2} r^4. \quad (\text{A.13})$$

Making the substitution  $u = 1/r$ , one then gets

$$\left(\frac{du}{d\phi}\right) = R_s u^3 - u^2 + \frac{R_s}{\tilde{L}^2} u + \frac{\tilde{E}^2 - 1}{\tilde{L}^2} \quad (\text{A.14})$$

which we can identify as a third degree polynomial in  $u$

$$\left(\frac{du}{d\phi}\right)^2 = R_s(u - u_1)(u - u_2)(u - u_3). \quad (\text{A.15})$$

where  $u_1$ ,  $u_2$  and  $u_3$  are the extrema of the trajectory.

For the purposes of this thesis, we only need to consider unbound trajectories, eg.  $\tilde{E} > 1$ . As stated in section [4.1.1](#), this implies through eq. [\(A.14\)](#) and eq. [\(A.15\)](#) that

$$u_1 u_2 u_3 = -\frac{\tilde{E} - 1}{\tilde{L}^2 R_s} < 0, \quad (\text{A.16})$$

which means that either all extrema are negative ( $u_i < 0$  for all  $i$ ), or one is negative with the other two either being real and positive or complex conjugates ( $u_1 < 0$ ,  $u_2 \times u_3 > 0$ ). The physical interpretation of these cases is discussed in detail in section [4.1.1](#), and here we only describe how one calculates the trajectory of particles in these different cases. We only need to mention that in the case of all roots being real, a particle comming in from infinity reaches some perihelion distance, whereas for two roots being complex conjugate, the particle spirals inwards towards the centre.

#### All roots real

We start by taking  $u_1$ ,  $u_2$  and  $u_3$  as

$$u_1 = \frac{1}{l}(1 - e) \quad (\text{A.17})$$

$$u_2 = \frac{1}{l}(1 + e) \quad (\text{A.18})$$

$$u_3 = \frac{1}{R_s} - \frac{2}{l} \quad (\text{A.19})$$

where  $l$ , the latus rectum is some constant, and  $e$  the eccentricity. If we then make the substitution

$$u = \frac{1}{l}(1 + e \cos \chi) \quad (\text{A.20})$$

where  $\chi$  some relativistic anomaly the square root of eq. (A.15) becomes

$$\left( \frac{d\chi}{d\phi} \right)^2 = \left[ \left( 1 - \frac{3R_s}{l} + \frac{R_s r}{l} \right) - \frac{2R_s e}{l} \cos^2 \chi / 2 \right]. \quad (\text{A.21})$$

If we not invert this expression, take the square root and extract some factors, we arrive at

$$d\phi = \pm \frac{d\chi}{\Delta (1 - k^2 \cos^2 \chi / 2)}, \quad (\text{A.22})$$

where  $\Delta$  and  $k$  are defined as

$$\Delta = 1 - \frac{3R_s}{l} + \frac{R_s r}{l} \quad (\text{A.23})$$

$$k^2 = \frac{2R_s e}{l \Delta} \quad (\text{A.24})$$

Returning to eq. (A.20), we can see that the perihelion occurs at  $\chi = 0$ . If we set the perihelion as the origin for  $\phi$ , our limits become

$$\phi = \frac{1}{\Delta} \int_0^\chi \frac{d\chi'}{\sqrt{1 - k^2 \cos^2 \chi' / 2}}, \quad (\text{A.25})$$

where the  $\pm$  is implicit, but has been dropped due to symmetry around  $\chi = 0$ . Making one final substitution  $t = (\pi - \chi)/2$ , the resulting integral becomes

$$\phi = -\frac{2}{\Delta} \int_{\pi/2}^{\pi/2 - \chi/2} \frac{dt}{\sqrt{1 - k^2 \sin^2 t}}. \quad (\text{A.26})$$

which can be written as

$$\phi = \frac{2}{\Delta} [K(k) - F(\pi/2 - \chi/2, k)] \quad (\text{A.27})$$

where  $K$  and  $F$  are the complete and incomplete elliptic integrals of the first kind, defined as

$$K(k) = \int_0^{\pi/2} \frac{dt}{\sqrt{1 - k^2 \sin^2(t)}} \quad (\text{A.28})$$

$$F(\psi, k) = \int_0^\psi \frac{dt}{\sqrt{1 - k^2 \sin^2(t)}}, \quad (\text{A.29})$$

both of which can be approximated numerically (Press et al. 2007).

For section 4.1.1, we saw that we needed the total scattering angle  $\Theta$ . By referring back to eq. (A.20), we see that the angle at infinity corresponds to  $\chi_\infty = \arccos(-e^{-1})$ , which means that the limit if the incomplete integral goes to  $(\chi_\infty - \pi)/2 = \arccos(e^{-1})$ , or

$$\phi_\infty = \frac{2}{\Delta} [K(k) - F(\arccos(e^{-1})/2, k)]. \quad (\text{A.30})$$

As the particle is both comming in from infinity and leaving to infinity, and we have chosen such that  $\phi$  is symmetric about  $\chi = 0$ , the total scattering angle is equal to  $\Theta = 2\phi_\infty$  or

$$\Theta = \frac{4}{\Delta} [K(k) - F(\arccos(e^{-1})/2, k)] - \pi. \quad (\text{A.31})$$

### Complex roots

For  $\tilde{L}$  corresponding to complex roots, we take  $u_1$ ,  $u_2$  and  $u_3$  similar as with the real roots, but with imaginary eccentricities:

$$u_1 = \frac{1}{l}(1 - ie) \quad (\text{A.32})$$

$$u_2 = \frac{1}{l}(1 + ie) \quad (\text{A.33})$$

$$u_3 = \frac{1}{R_s} - \frac{2}{l}. \quad (\text{A.34})$$

Making a similar substitution as with A.20:

$$u = \frac{1}{l}(1 + e \tan(\xi/2)), \quad (\text{A.35})$$

eq. (A.15) can be expressed as

$$\left( \frac{d\xi}{d\phi} \right)^2 = 2 \left[ \left( \frac{3R_s}{l} - 1 \right) + \frac{R_s e}{l} \sin \xi + \left( \frac{3R_s}{l} - 1 \right) \cos \xi \right]. \quad (\text{A.36})$$

As previously, taking the square root and inverting this expression gived  $\phi$  as an integral. Further making the change of variable

$$\sin^2 \psi = \frac{1}{\Delta + 3R_s/l - 1} \left[ \Delta - \frac{R_s e}{l} \sin \xi - \left( \frac{3R_s}{l} - 1 \right) \cos \xi \right], \quad (\text{A.37})$$

where

$$\Delta = \left[ \left( \frac{3R_s}{l} - 1 \right)^2 + \frac{R_s^2 e^2}{l^2} \right], \quad (\text{A.38})$$

one can once again retrieve  $\phi$  from solving a complete and a incomplete elliptic integral

$$\phi = \frac{2}{\Delta^{1/2}} [K(k) - F(\psi, k)]. \quad (\text{A.39})$$

## A.2 General static, spherically symmetric metric

In this section, we show how one can, in a relatively simple way, numerically integrate trajectories of test particles in a general time independent, spherically symmetric metric. Due to the metric being time independent and spherically symmetric, it is diagonal and only dependent on the radius from the centre  $r$  (Schutz 2009), eg.

$$g_{\alpha\beta} = \begin{pmatrix} g_{tt}(r) & 0 & 0 & 0 \\ 0 & g_{rr}(r) & 0 & 0 \\ 0 & 0 & r^2 & 0 \\ 0 & 0 & 0 & 0 \end{pmatrix}, \quad (\text{A.40})$$

where we have chosen the plane such that the second angle  $\theta = \pi/2$ . For the same reason, as with the Schwarzschild metric, angular momentum and energy is conserved, giving the 4-momentum

$$\frac{1}{m} p^t = \frac{dt}{d\tau} = g^{tt} \tilde{E} \quad (\text{A.41})$$

$$\frac{1}{m} p^\phi = \frac{d\phi}{d\tau} = \frac{1}{r^2} \tilde{L} \quad (\text{A.42})$$

$$\frac{1}{m} p^r = \frac{dr}{d\tau}, \quad (\text{A.43})$$

where  $\tilde{E} = p_t$  is the specific energy, and  $\tilde{L} = p_\phi$  the specific momentum. We can then again use the fact that  $p^\mu p_\mu = -m^2$  and get,

$$-m^2 = -p^t p_t + p^r p_r + p^\phi p_\phi \quad (\text{A.44})$$

$$\implies -1 = -g^{tt} \tilde{E}^2 + g_{rr} \left( \frac{dr}{d\tau} \right)^2 + \frac{\tilde{L}^2}{r^2} \quad (\text{A.45})$$

$$\implies \left( \frac{dr}{d\tau} \right)^2 = \frac{1}{g_{rr}} \left( g^{tt} \tilde{E}^2 - \left[ 1 + \frac{\tilde{L}^2}{r^2} \right] \right). \quad (\text{A.46})$$

From here, one can take the root of equation eq. (A.46) to get

$$\frac{dr}{d\tau} = \pm \sqrt{\frac{1}{g_{rr}} \left( g^{tt} \tilde{E}^2 - \left[ 1 + \frac{\tilde{L}^2}{r^2} \right] \right)}. \quad (\text{A.47})$$

which, along with with eqs. (A.41) and (A.42) can be integrated to obtain the corresponding coordinates.

The solution of eq. (A.47) convenient when the problem is (semi-)analytic as with the Schwarzschild metric (see sec. A.1). However, when the metric is complicated enough for an analytic solution to be unobtainable and one has to rely on numerical integration, the sign of eq. (A.47) becomes an issue. As this sign determines if a particle is moving outwards or

inwards, this needs to be manually switched once a particle reaches a minimum distance. This then come down to (arbitrary) numerical precision for changing the sign. In order to integrate the full trajectory then, it can be more convenient to take the derivative of eq. (A.46)

$$2 \frac{dr}{d\tau} \frac{d^2r}{d\tau^2} = \frac{d}{d\tau} \left[ \frac{1}{g_{rr}} \left( g^{tt} \tilde{E}^2 - \left[ 1 + \frac{\tilde{L}^2}{r^2} \right] \right) \right]. \quad (\text{A.48})$$

To solve the right hand side of eq. (A.48), we can use the fact that the metric is diagonal, meaning that  $g^{tt} = -g_{tt}^{-1}$  and  $g^{rr} = g_{rr}^{-1}$ , and that

$$\frac{d}{d\tau} = \frac{dr}{d\tau} \frac{d}{dr}. \quad (\text{A.49})$$

This then gives eq. (A.48) as

$$2 \frac{dr}{d\tau} \frac{d^2r}{d\tau^2} = \frac{dr}{d\tau} \left[ g^{rr} \left( g_{tt}^{-2} g_{tt,r} \tilde{E}^2 + 2 \frac{\tilde{L}^2}{r^3} \right) - g_{rr}^{-2} g_{rr,r} \left( g^{tt} \tilde{E}^2 - \left[ 1 + \frac{\tilde{L}^2}{r^2} \right] \right) \right], \quad (\text{A.50})$$

where  $g_{tt,r}$  indicates the partial derivative

$$g_{tt,r} = \frac{\partial g_{tt}}{\partial r}, \quad (\text{A.51})$$

with the same notation for  $g_{rr,r}$ . The equations to be integrated is then

$$\frac{dt}{d\tau} = g^{tt} \tilde{E} \quad (\text{A.52})$$

$$\frac{d\phi}{d\tau} = \frac{1}{r^2} \tilde{L} \quad (\text{A.53})$$

$$\frac{d^2r}{d\tau^2} = \frac{g^{rr}}{2} \left[ g_{tt}^{-2} g_{tt,r} \tilde{E}^2 + 2 \frac{\tilde{L}^2}{r^3} - g^{rr} g_{rr,r} \left( g^{tt} \tilde{E}^2 - \left[ 1 + \frac{\tilde{L}^2}{r^2} \right] \right) \right]. \quad (\text{A.54})$$

# Appendix B

## Galactic neutron star distribution

It is known that NSs receive a natal kick in the supernovae that produces them, probably due to spatial asymmetry in the explosion (eg. [Lyne & Lorimer 1994](#); [Hansen & Phinney 1997](#)). The details of this kick is uncertain, but most estimates and models puts the average magnitude of the change in velocity as  $\sim 300 - 400 \text{ km s}^{-1}$  ([Arzoumanian et al. 2002](#); [Hobbs et al. 2005](#)). By chance, this means that the kick velocity that NS gains is roughly equivalent in magnitude to that of the orbital velocity around the Galaxy. Therefore the orbits of NS can be greatly affected by the natal kick, which then means that their distribution in the galaxy can be substantially different from that of main sequence stars. As we have shown in the main text, the capture rate of PBHs is strongly dependent on the dark matter density and velocity dispersion, both of which varies in the Galaxy. So in order to estimate the capture rate of PBHs by NS, we need to take into account the natal kicks of NS, and their resulting distribution in the galaxy. To do this, we construct a population synthesis of NS, where we sample properties of the NS and their progenitors, and the integrate the NS in a galactic potential. This appendix describes this population synthesis.

### B.1 Population synthesis

To emulate the Galactic population of NS, we need to know the galactic distribution of their progenitors, natal-kick velocity and age of the NS. In this section we describe the distribution chosen for these initial conditions.

#### B.1.1 Galactic distribution

Starting with the galactic distribution of the progenitors, we take a similar approach to [Faucher-Giguère & Kaspi \(2006\)](#) (see also [Sartore, N. et al. 2010](#)). We adopt an exponential profile for the radial distribution, based of the surface density of supernovae remnants in the galaxy ([Case & Bhattacharya 1998](#)) :

$$f(R) = \left(\frac{R}{R_0}\right)^2 \exp\left(-\frac{\beta(R - R_0)}{R_0}\right), \quad (\text{B.1})$$

Table B.1: Parameters for the spiral arms form [Wainscoat et al. \(1992\)](#)

	Spiral 1	Spiral 2	Spiral 3	Spiral 4
$k$	4.25	4.25	4.89	4.89
$R_k$ [kpc]	3.48	3.48	4.9	4.9
$\varphi_0$	1.57	4.71	4.09	0.95

where  $R_0 = 8.5$  kpc, and  $\beta = 3.53$ , and  $R = \sqrt{x^2 + y^2}$ .

SNe originate from massive stars, which have short lifetimes, and as such the progenitors explodes close to their birth sites, eg. in the spiral arms of the Galaxy. Therefore, we distribute the progenitors on four spiral arms by the equation

$$\varphi = k \log(R/R_k) + \varphi_0, \quad (\text{B.2})$$

where  $\varphi$  is the angle between  $x$  and  $R$ , and the parameters  $k$ ,  $R_k$  and  $\varphi_0$  are taken from [Wainscoat et al. \(1992\)](#), with each parameter being different for each spiral arm, as shown in tab. B.1. The NS are then given a spread in both  $\varphi \rightarrow \varphi + \varphi_{\text{spread}}$  and  $R \rightarrow R + R_{\text{spread}}$  by

$$f(R_{\text{spread}}) = \left( \frac{1}{2\pi\sigma_R^2} \right)^{1/2} \exp \left( -\frac{R_{\text{spread}}^2}{2\sigma_R^2} \right) \quad (\text{B.3})$$

$$f(\varphi_{\text{spread}}) = \frac{1}{2\pi} \exp \left( -\frac{0.35R}{\text{kpc}} \right), \quad (\text{B.4})$$

where  $\sigma_R = 0.07R$ . Finally we spread the progenitors vertically with an exponential profile with a mean absolute value of  $\langle |z| \rangle = 50$  pc:

$$f(z) = \frac{1}{\langle |z| \rangle} \exp \left( -\frac{|z|}{\langle |z| \rangle} \right). \quad (\text{B.5})$$

### B.1.2 Kick velocity and NS age

As mentioned before, the velocity imparted on NS by the natal kick is still uncertain, but most estimates suggest either a single Maxwellian distribution ([Lyne & Lorimer 1994](#); [Hobbs et al. 2005](#)), or a double peaked distribution [Arzoumanian et al. \(2002\)](#). For simplicity we adopt a single Maxwellian distribution

$$f(v) = \left( \frac{1}{2\pi\sigma_v^2} \right)^{3/2} 2\pi v^2 \exp \left( -\frac{v^2}{2\sigma_v^2} \right), \quad (\text{B.6})$$

with a velocity dispersion of  $\sigma_v = 265$  km s<sup>-1</sup> from [Hobbs et al. \(2005\)](#). We orient the velocity in the Galactic coordinate system randomly via two angles, drawn from  $\sin \theta d\phi d\theta$ .

We chose to neglect the effects of binaries in our kick velocity, an approximation which we discuss later in this appendix.

Similar to [Sartore, N. et al. \(2010\)](#), we chose to assign an age to the NS. The reason for this is to average over the orbital period of the NSs. As the orbits that NS are kicked into are generally not circular, their position in the Galaxy depends on time. Therefore we need to average over time, which can be done by giving each NS an age. We assume an uniform distribution in age from zero to 10 Gyr, eg. a constant starformation rate.

### B.1.3 Numerical integration

The model of our galaxy is described by three components, a bulge, disc and a DM halo. For the bulge we adopt a Hernquist distribution ([Hernquist 1990](#)), eg. a potential of

$$\Phi_{\text{bulge}}(r) = -\frac{GM_b}{r + r_b}, \quad (\text{B.7})$$

where the parameters are chosen as  $M_b = 1.6 \times 10^{10} M_\odot$  and  $r_b = 0.6$  kpc as in ([Sartore, N. et al. 2010](#)). We describe the Disc as a Miyamoto-Nagai potential ([Miyamoto & Nagai 1975](#))

$$\Phi_{\text{disc}}(R, z) = -\frac{GM_d}{\left(R^2 + \left(a_d + \sqrt{z^2 + b_d^2}\right)^2\right)^{1/2}}, \quad (\text{B.8})$$

where the values are chosen as in [Paczynski \(1990\)](#), with  $M_d = 8.07 M_\odot$ ,  $a_d = 3.7$  kpc and  $b_d = 0.2$  kpc. And finally we describe the DM halo with an NFW profile ([Navarro et al. 1995](#)).

$$\Phi_{\text{halo}}(r) = -4\pi G \rho_0 r_0^2 \frac{\ln(1 + r/r_0)}{r/r_0}, \quad (\text{B.9})$$

with  $r_0 = 20$  kpc and  $\rho_0 = 0.0079 M_\odot \text{ pc}^{-3}$ . The DM density and circular velocity at 8.5 kpc is found as  $\rho_{\text{DM}}(8.5 \text{ kpc}) = 0.0092 M_\odot \text{ pc}^{-3}$ ,  $v_c = 240 \text{ km s}^{-1}$ , in rough agreement to what we expect in the Milky Way (cf. section [3.2.1](#)).

We initialise  $5 \times 10^6$  NS-particles out to  $R = 25$  kpc according to the distributions in sec. [B.1.1](#), with all of the NS initialy on a circular orbit (before the kick). The resulting initial distribution in the  $xy$ - and  $Rz$ -planes are shown in fig. [B.1](#). We then integrate the orbits according to

$$\mathbf{a} = -\nabla(\Phi_{\text{bulge}} + \Phi_{\text{disc}} + \Phi_{\text{halo}}), \quad (\text{B.10})$$

using the [Dormand & Prince \(1980\)](#) fourth order runge-kutta integrator. Each NS is integrated for the time corresponding its age (eg. a NS of age 4 Gyr is integrated for 4 Gyr).

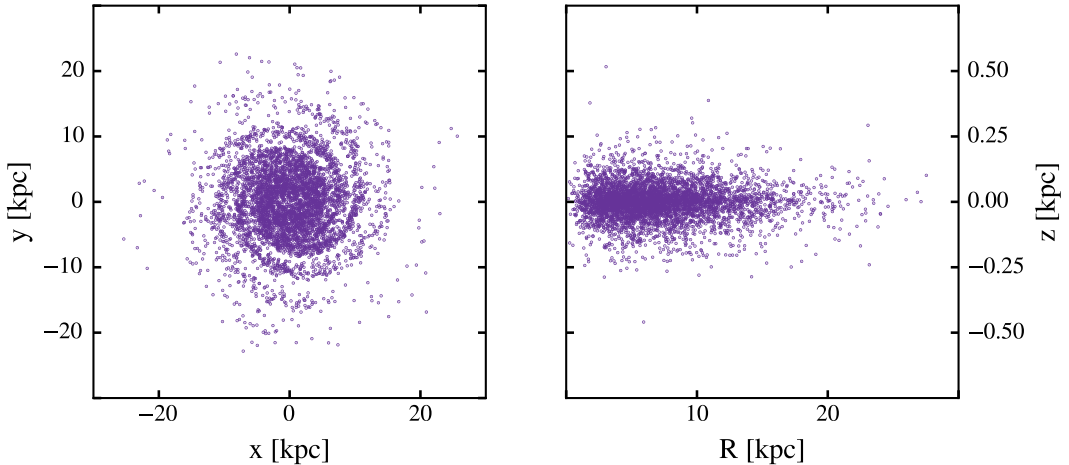


Figure B.1: The initial positions of the NS population (only 5000 shown). In the  $xy$ -plane on the left and  $Rz$ -plane on the right. The  $z$  axis is scaled for clarity.

## B.2 Resulting distribution

The initial and resulting distribution in  $R$  is shown in the right hand side of fig. B.2. The NS have (predictably) become much more spread out, and reach much further distances. Similarly for  $z$ , we can see in the left hand side of fig. B.2 a much larger spread (compared to fig. B.1, where we keep in mind different scaling). We find that the average vertical height has increased drastically up to  $\langle z \rangle = 35$  kpc. For a better estimate of the spread in  $z$  we adopt the average half-density thickness  $z_{1/2}$  from (Sartore, N. et al. 2010), eg. the height where the number density has decreased by half from its midplane value.  $z_{1/2}$  has increased from 35 pc in the initial conditions to  $z_{1/2} = 216$  pc, which consistent with that found in Sartore, N. et al. (2010), who also agree on the fraction of NS still bound ( $\sim 80\%$ ).

The distribution found does not agree with that of low mass x-ray binaries (see references in Repetto et al. 2012). This points to that ignored the possible impact of binaries in this population synthesis model. While we are interested in single NSs, as the binary fraction of stars is significant (especially for high mass), a large fraction of the NSs may come from binaries disrupted by the SN kick. The velocity the NS then gains at birth is the vector addition of the kick velocity and the orbital velocity of the binary. For wide binaries the kick velocity greatly exceeds the orbital velocity of the binary, and the effect becomes negligible. However for binaries with smaller semi-major axes, two velocities become comparable (semi-major axis of  $\sim 10 R_\odot$  for two  $10 M_\odot$  stars). The distribution of NSs computed here may therefore be biased. We do however note that the kick velocity distribution used here is based on observations of pulsars (Hobbs et al. 2005), and therefore should give a reasonable approximation of the real distribution (assuming decent models

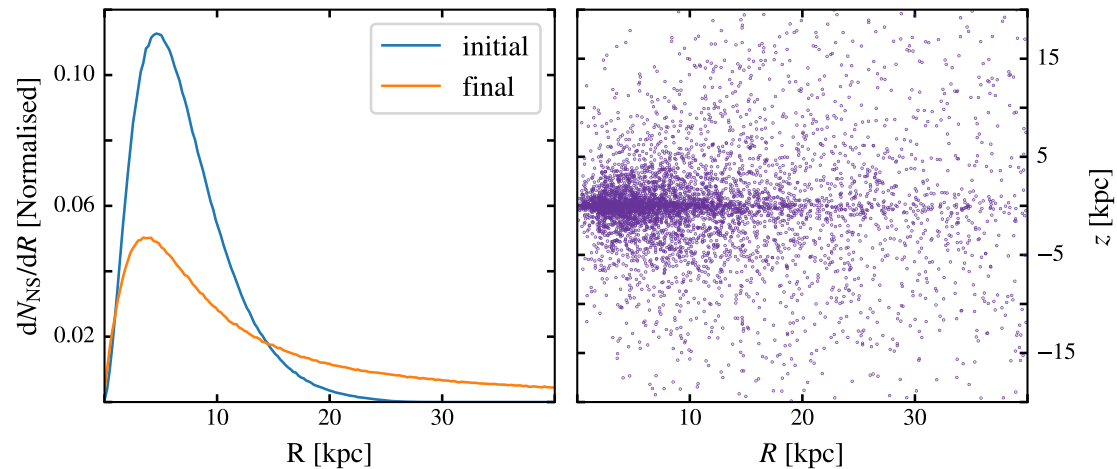


Figure B.2: Circular velocity, initial distribution of NS and final distribution of NS

for the birth location and galactic potential has been used).

# Bibliography

- Abramowicz, M. A., Becker, J. K., Biermann, P. L., et al. 2009, ApJ, 705, 659
- Abramowicz, M. A., Bejger, M., & Wielgus, M. 2018, ApJ, 868, 17
- Adams, J. J., Simon, J. D., Fabricius, M. H., et al. 2014, ApJ, 789, 63
- Afshordi, N., McDonald, P., & Spergel, D. N. 2003, ApJL, 594, L71
- Alcock, C., Allsman, R. A., Alves, D., et al. 1998, The Astrophysical Journal Letters, 499, L9
- Ali-Haïmoud, Y. & Kamionkowski, M. 2017, Phys. Rev. D, 95, 043534
- Ali-Haïmoud, Y., Kovetz, E. D., & Kamionkowski, M. 2017, Phys. Rev. D, 96, 123523
- Arzoumanian, Z., Chernoff, D. F., & Cordes, J. M. 2002, ApJ, 568, 289
- Ballesteros, G. & Taoso, M. 2018, Phys. Rev. D, 97, 023501
- Barnabè, M., Dutton, A. A., Marshall, P. J., et al. 2012, MNRAS, 423, 1073
- Barnacka, A., Glicenstein, J.-F., & Moderski, R. 2012, Phys. Rev. D, 86, 043001
- Bartelmann, M. 2010, Classical and Quantum Gravity, 27, 233001
- Barthelmy, S. D., Barbier, L. M., Cummings, J. R., et al. 2005, Space Sci. Rev., 120, 143
- Begelman, M. C. 1979, MNRAS, 187, 237
- Belvedere, R., Pugliese, D., Rueda, J. A., Ruffini, R., & Xue, S.-S. 2012, Nucl. Phys. A, 883, 1
- Bertone, G., Hooper, D., & Silk, J. 2005, Physics Reports, 405, 279
- Binney, J. & Tremaine, S. 2008, Galactic Dynamics: Second Edition (Princeton University Press)
- Bland-Hawthorn, J. & Gerhard, O. 2016, Annual Review of Astronomy and Astrophysics, 54, 529

## *BIBLIOGRAPHY*

---

- Bondi, H. 1952, MNRAS, 112, 195
- Bowman, J. D., Rogers, A. E. E., Monsalve, R. A., Mozdzen, T. J., & Mahesh, N. 2018, Nature, 555, 67
- Bramante, J., Linden, T., & Tsai, Y.-D. 2018, Phys. Rev. D, 97, 055016
- Brandt, T. D. 2016, ApJL, 824, L31
- Brown, W. R. 2015, Annu. Rev. Astron. Astrophys, 53, 15
- Capela, F., Pshirkov, M., & Tinyakov, P. 2013, Phys. Rev. D, 87, 123524
- Capela, F., Pshirkov, M., & Tinyakov, P. 2014, ArXiv e-prints, arXiv:1402.4671
- Carr, B., Kühnel, F., & Sandstad, M. 2016, Phys. Rev. D, 94, 083504
- Carr, B. J. & Hawking, S. W. 1974, MNRAS, 168, 399
- Carr, B. J., Kohri, K., Sendouda, Y., & Yokoyama, J. 2010, Phys. Rev. D, 81, 104019
- Carr, B. J., Kohri, K., Sendouda, Y., & Yokoyama, J. 2010, Phys. Rev. D, 81, 104019
- Carr, B. J. & Sakellariadou, M. 1999, ApJ, 516, 195
- Case, G. L. & Bhattacharya, D. 1998, ApJ, 504, 761
- Chabrier, G. 2003, Publications of the Astronomical Society of the Pacific, 115, 763
- Chandrasekhar, S. 1983, The Mathematical Theory of Black Holes (Clarendon Press/Oxford University Press)
- Cipolletta, F., Cherubini, C., Filippi, S., Rueda, J. A., & Ruffini, R. 2015, Phys. Rev. D, 92, 023007
- Clark, S., Dutta, B., Gao, Y., Ma, Y.-Z., & Strigari, L. E. 2018, ArXiv e-prints
- Defillon, G., Granet, E., Tinyakov, P., & Tytgat, M. H. G. 2014, Phys. Rev. D, 90, 103522
- Dexter, J. & O’Leary, R. M. 2014, ApJ, 783, L7
- Dormand, J. & Prince, P. 1980, J. Comput. Appl. Math., 6, 19
- Dutton, A. A. & Macciò, A. V. 2014, MNRAS, 441, 3359
- Faucher-Giguère, C.-A. & Kaspi, V. M. 2006, ApJ, 643, 332
- Flores, R. A. & Primack, J. R. 1994, ApJL, 427, L1
- Fritz, T. K., Chatzopoulos, S., Gerhard, O., et al. 2016, ApJ, 821, 44

- Fuller, G. M., Kusenko, A., & Takhistov, V. 2017, Phys. Rev. Lett., 119, 061101
- Garbari, S., Liu, C., Read, J. I., & Lake, G. 2012, MNRAS, 425, 1445
- García-Bellido, J., Clesse, S., & Fleury, P. 2018, Physics of the Dark Universe, 20, 95
- Gehrels, N. & Mészáros, P. 2012, Science, 337, 932
- Gould, A. 1992, ApJL, 386, L5
- Graham, P. W., Rajendran, S., & Varela, J. 2015, Phys. Rev. D, 92, 063007
- Griest, K., Cieplak, A. M., & Lehner, M. J. 2013, Phys. Rev. Lett., 111, 181302
- Griest, K., Cieplak, A. M., & Lehner, M. J. 2014, ApJ, 786, 158
- Hansen, B. M. S. & Phinney, E. S. 1997, MNRAS, 291, 569
- Hawking, S. 1971, MNRAS, 152, 75
- Hawking, S. W. 1975, Communications in Mathematical Physics, 43, 199
- Hektor, A., Hütsi, G., Marzola, L., et al. 2018, ArXiv e-prints
- Hernquist, L. 1990, ApJ, 356, 359
- Hessels, J. W. T., Ransom, S. M., Stairs, I. H., et al. 2006, Science, 311, 1901
- Hills, J. G. 1988, Nature, 331, 687
- Hobbs, G., Lorimer, D. R., Lyne, A. G., & Kramer, M. 2005, MNRAS, 360, 974
- Inayoshi, K., Haiman, Z., & Ostriker, J. P. 2016, MNRAS, 459, 3738
- Inomata, K., Kawasaki, M., Mukaida, K., & Yanagida, T. T. 2018, Phys. Rev. D, 97, 043514
- Jakobsson, P., Levan, A., Fynbo, J. P. U., et al. 2006, A&A, 447, 897
- Kafle, P. R., Sharma, S., Lewis, G. F., & Bland-Hawthorn, J. 2014, ApJ, 794, 59
- Kalogera, V., Narayan, R., Spergel, D. N., & Taylor, J. H. 2001, ApJ, 556, 340
- Kawaler, S. D. 2003, arXiv e-prints, astro
- Khlopov, M. Y. 2010, Research in Astronomy and Astrophysics, 10, 495
- Kouvaris, C. & Tinyakov, P. 2014, Phys. Rev. D, 90, 043512
- Kroupa, P. 2001, MNRAS, 322, 231

## *BIBLIOGRAPHY*

---

- Lake, G. 1989, AJ, 98, 1554
- Leach, S. M., Grivell, I. J., & Liddle, A. R. 2000, Phys. Rev. D, 62, 043516
- Liebert, J., Bergeron, P., & Holberg, J. B. 2005, ApJS, 156, 47
- Lorimer, D. R. 2005, Living Reviews in Relativity, 8, 7
- LSST Science Collaboration, Abell, P. A., Allison, J., et al. 2009, arXiv e-prints, arXiv:0912.0201
- Luo, Y., Hanasoge, S., Tromp, J., & Pretorius, F. 2012, ApJ, 751, 16
- Lyne, A. G. & Lorimer, D. R. 1994, Nature, 369, 127
- Markovic, D. 1995, MNRAS, 277, 25
- Mayer, L. 2018, arXiv e-prints, arXiv:1807.06243
- McConnachie, A. W. 2012, AJ, 144, 4
- Meszaros, P. 1975, A&A, 38, 5
- Miyamoto, M. & Nagai, R. 1975, Publications of the Astronomical Society of Japan, 27, 533
- Moore, B. 1994, Nature, 370, 629
- Naab, T. & Ostriker, J. P. 2017, Annual Review of Astronomy and Astrophysics, 55, 59
- Naderi, T., Mehrabi, A., & Rahvar, S. 2018, Phys. Rev. D, 97, 103507
- Nakamura, T., Sasaki, M., Tanaka, T., & Thorne, K. S. 1997, ApJ, 487, L139
- Navarro, J. F., Frenk, C. S., & White, S. D. M. 1995, MNRAS, 275, 720
- Nesti, F. & Salucci, P. 2013, JCAP, 2013, 016
- Niikura, H., Takada, M., Yasuda, N., et al. 2017, ArXiv e-prints
- Niikura, H., Takada, M., Yasuda, N., et al. 2019a, Nature Astronomy, 238
- Niikura, H., Takada, M., Yokoyama, S., Sumi, T., & Masaki, S. 2019b, Phys. Rev. D, 99, 083503
- Ohsuga, K., Mori, M., Nakamoto, T., & Mineshige, S. 2005, ApJ, 628, 368
- Paczynski, B. 1986, ApJ, 304, 1
- Paczynski, B. 1990, ApJ, 363, 218

- Pani, P. & Loeb, A. 2014, JCAP, 2014, 026
- Peters, P. C. 1964, Phys. Rev., 136, B1224
- Phinney, E. S. 1991, ApJ, 380, L17
- Planck Collaboration, Ade, P. A. R., Aghanim, N., et al. 2016, A&A, 594, A13
- Podsiadlowski, P., Mazzali, P. A., Nomoto, K., Lazzati, D., & Cappellaro, E. 2004, ApJ, 607, L17
- Polnarev, A. G. & Khlopov, M. Y. 1982, Soviet Astronomy, 26, 391
- Press, W. H., Teukolsky, S. A., Vetterling, W. T., & Flannery, B. P. 2007, Numerical Recipes 3rd Edition: The Art of Scientific Computing, 3rd edn. (New York, NY, USA: Cambridge University Press)
- Prialnik, D. 2009, An Introduction to the Theory of Stellar Structure and Evolution
- Quinn, D. P., Wilkinson, M. I., Irwin, M. J., et al. 2009, MNRAS Letters, 396, L11
- Rajwade, K. M., Lorimer, D. R., & Anderson, L. D. 2017, MNRAS, 471, 730
- Read, J. I. 2014, Journal of Physics G: Nuclear and Particle Physics, 41, 063101
- Read, J. I., Agertz, O., & Collins, M. L. M. 2016, MNRAS, 459, 2573
- Read, J. I. & Gilmore, G. 2005, MNRAS, 356, 107
- Read, J. I., Iorio, G., Agertz, O., & Fraternali, F. 2017, MNRAS, 467, 2019
- Read, J. I., Walker, M. G., & Steger, P. 2018, ArXiv e-prints
- Repetto, S., Davies, M. B., & Sigurdsson, S. 2012, MNRAS, 425, 2799
- Ricotti, M., Ostriker, J. P., & Mack, K. J. 2008, ApJ, 680, 829
- Rosswog, S. & Davies, M. B. 2002, MNRAS, 334, 481
- Roulet, E. & Mollerach, S. 1997, Physics Reports, 279, 67
- Salpeter, E. E. 1955, ApJ, 121, 161
- Sartore, N., Ripamonti, E., Treves, A., & Turolla, R. 2010, A&A, 510, A23
- Sasaki, M., Suyama, T., Tanaka, T., & Yokoyama, S. 2018, Classical and Quantum Gravity, 35, 063001
- Schutz, B. 2009, A First Course in General Relativity (Cambridge University Press)

## *BIBLIOGRAPHY*

---

- Schwarzschild, K. 1916, Sitzungsber. K. Preuss. Akad. Wiss., Phys.-Math. Kl., 189
- Sivertsson, S., Silverwood, H., Read, J. I., Bertone, G., & Steger, P. 2018, MNRAS, 478, 1677
- Snodgrass, H. B. & Ulrich, R. K. 1990, ApJ, 351, 309
- Sreekumar, P., Bertsch, D. L., Dingus, B. L., et al. 1998, ApJ, 494, 523
- Strong, A. W., Moskalenko, I. V., & Reimer, O. 2004, ApJ, 613, 962
- Takhistov, V. 2018, Physics Letters B, 782, 77
- Tisserand, P., Le Guillou, L., Afonso, C., et al. 2007, A&A, 469, 387
- Tsutsui, R., Yonetoku, D., Nakamura, T., Takahashi, K., & Morihara, Y. 2013, MNRAS, 431, 1398
- Wainscoat, R. J., Cohen, M., Volk, K., Walker, H. J., & Schwartz, D. E. 1992, The Astrophysical Journal Supplement Series, 83, 111
- Wyrzykowski, L., Kozłowski, S., Skowron, J., et al. 2010, MNRAS, 407, 189
- Wyrzykowski, L., Kozłowski, S., Skowron, J., et al. 2009, MNRAS, 397, 1228
- Wyrzykowski, L., Kozłowski, S., Skowron, J., et al. 2011a, MNRAS, 413, 493
- Wyrzykowski, L., Skowron, J., Kozłowski, S., et al. 2011b, MNRAS, 416, 2949
- Zhang, L., Rix, H.-W., van de Ven, G., et al. 2013, ApJ, 772, 108
- Zumalacárregui, M. & Seljak, U. c. v. 2018, Phys. Rev. Lett., 121, 141101
- Zwicky, F. 1933, Helvetica Physica Acta, 6, 110
- Özel, F. & Freire, P. 2016, Annu. Rev. Astron. Astrophys, 54, 401